

Application Of Artificial Neural Network Models For Predicting Total Dissolved Solids In Marsh Water

Dr. Mohammed D. Salman

College of Eng. / Mech. Eng. Dept. / University of Thi Qar

E-mail: Mohammed_selman2000@yahoo.com

ABSTRACT

In this paper an Artificial Neural Networks (ANNS) model is designed to predict the Total Dissolved Solids (TDS) concentration in marsh water. A previous data set are selected from previous studies which done on analysis of marsh water quality, these data are arranged in a format of five input parameters to feed forward back-propagation including the acidity (pH), calcium concentration (C), Magnesium Concentration (M), Chloride Concentration (Cl) and Sulphate Concentration (S), and one output parameter as Total Dissolved Solids concentration. Artificial Neural Network used to study the effect of each parameter on TDS concentration in marsh water. Several structures of ANNs model is examined with different transfer functions, activation functions, number of neurons in each hidden layer and number of hidden layers. Results show that the two hidden layer network with transfer function (tansig) with (12 & 10) neurons in the first and second hidden layer respectively and (tansig-tansig-purelin) gives the best performance (Mean Square Error: 3.05×10^{-5}) network for this prediction.

Keyword: Total Dissolved Solids, Neural Networks, Prediction, Marsh Water.

الخلاصة

في هذه الورقة صمم نموذج شبكات عصبية صناعية لتخمين تركيز المواد الصلبة الذائبة الكلية في مياه الاهوار. اختيرت مجموعة معلومات سابقة مختارة من الدراسات السابقة التي عملت على تحليل نوعية ماء الاهوار، رتب هذه البيانات في صيغة خمسة عوامل داخلية للشبكة متضمنة ذلك الحموضة (pH)، تركيز الكالسيوم، تركيز المغنيسيوم، تركيز الكلوريد، وتركيز الكبريتات، وعامل ناتج واحد متمثلاً بتركيز المواد الصلبة الذائبة في مياه الاهوار. استعملت الشبكة العصبية الصناعية لدراسة تأثير كل من العوامل الداخلة على تركيز المواد الصلبة الذائبة في مياه الاهوار. اختبرت عدة تراكيب لنموذج الشبكة العصبية في مختلف: دوال النقل، دوال التنشيط، عدد العقد في كل طبقة مخفية وعدد الطبقات المخفية. اوضحت النتائج بأن الشبكة العصبية ذو الطبقتين المخفيتين بوظيفة النقل (tansig) مع (12 و 10) عقد عصبية في الطبقة المخفية الاولى والثانية على التوالي و دالة تنشيط متمثلة بـ (tansig tansig purelin) تعطي أفضل أداء (متوسط مربع نسبة الخطأ: 3.05×10^{-5}) للشبكة لهذا التنبؤ في هذه الدراسة.

Introduction:-

Iraqi marshes are one of the most ancient marshes in the world and pride themselves on its beautiful scenery and its rich natural ecological system. Closely involved in the lives of people over many years, marshes have been an important water resource and helped create and preserve distinctive culture. Lack of water resources and optimum management have been two recent challenges of water resources engineering [1]. Population growth, decrease of useable water resources, improvements in lifestyle, growing rate of consumption, climate change and several other parameters have caused useable water to be a significant problem for future. Economic and efficient use of water resources and its management have an increasingly significant role. Prediction of Total Dissolved solids(TDS) in water is one of the methods which have been recently considered for management of water resources. The predictions can be used for water resources planning and management in case they are of acceptable accuracy. There are two methodologies for prediction of TDS, like other water quality parameters,; first, precise study of different processes which can affect water salinity and developing statistical or deterministic models according to the obtained information. Second, developing Data Driven Models using information and collected data; In the latter technique, relationship between input and output data can be found using input data, but still physical understanding of phenomena is significant for having suitable input data for model [2,3].

The artificial neural network (ANN) technique is an artificial intelligence technique that attempts to mimic the human brain's problem solving capabilities. Artificial neural networks are capable of self-organization and learning; patterns and concepts can be extracted directly from historical data. In general, artificial neural networks can be applied to the following types of problems: pattern classification, clustering and categorization, function approximation, prediction and forecasting, optimization, associative memory, and process control. When presented with data patterns, sets of historical input and output data that describe the problem to be modeled, ANNs map the cause-and-effect relationships between the model input data and output data. This mapping of input and output relationships in the ANN model architecture allows developed models to be used to predict the value of the model output parameter, given any reasonable combination of model input data, with satisfactory accuracy[4].

This paper, artificial neural network model is used to represent the theoretical work, this model is coded using *MATLAB* (R2008a). Then '*MATLAB Function* program' is developed to call the model results (the correct weights and bases); this function is saved with the M-File basic functions of *MATLAB*. In order to simplifying this model for general use, graphical user interface is developed using *MATLAB* code, the result of this program is based on the '*MATLAB Function* program' which, in turn, uses neural network model result.

Neural network model is used to predict the Total Dissolved Solids in water which depends upon the results of the experimental work as training and testing data. The aim of the theoretical work is to obtain the best neural network model used to predict the overall mass transfer coefficient.

1. Artificial Neural Networks Model:

Theoretical work which is represented by ANN modelling. This program implements several different neural network algorithms, including back-propagation algorithm. The configuration and training of neural networks is a trial-and-error process due to such undetermined parameters as the number of hidden layers, the number of nodes in the hidden layers, the learning parameter, and the number of training patterns. An artificial neural network is developed to predict TDS. This section describes the data selection for training and testing patterns, the topology of the constructed network, the training process and the verification of the neural network results. The successful application of neural network to a problem depends on the problem representation and learning. Problem representation means the selection of a proper topology of the network.

The back propagation networks are most useful for problems involving forecasting and pattern recognition. Two subsets of data are used to build a neural network model: a training set and a testing set. The training phase needs to produce a neural network that is both stable and convergent. Therefore, selecting what data to use for training a network is one of the most important steps in building a neural network model. The training set is used for computing the gradient and updating the network weights and biases to diminish the training error, and find the relationship between the input and output parameters. Hence, the learning process is a crucial phase in NN modeling. The testing set is used to evaluate the generalization ability of the learning process. In this study the testing set contains approximately (20) % of total database. The parameters used in this study are shown in Table (1) [5,6,7,8]. The experimental values used to train the neural network as training data. The total number of

(140) test cases were utilized. The training set contains (112) cases and the testing set comprises of (28) cases.

1.1 Structure of Back propagation Neural Network:-

The nodes in the input layer and output layer are usually determined by the nature of the problem. The main difficulty in the structural identification of a complex nonlinear system arises from the huge amount of possible relationships among variables. The selection of outputs is straightforward and depends on the modeling goal. However, informed input-variable selection is critical to achieving efficient model performance [9].

In this study the (140) sample data are chosen for parameters which may be introduced as the components of the input vector consist of the pH, Calcium concentration (C), Magnesium Concentration (M), Chloride Concentration (Cl) and Sulfate Concentration. The output data is the Total Dissolved Solids Concentration (TDS) in marsh water Therefore, the nodes in the input layer and output layer are (5) and (1), respectively as shown in figure (1).

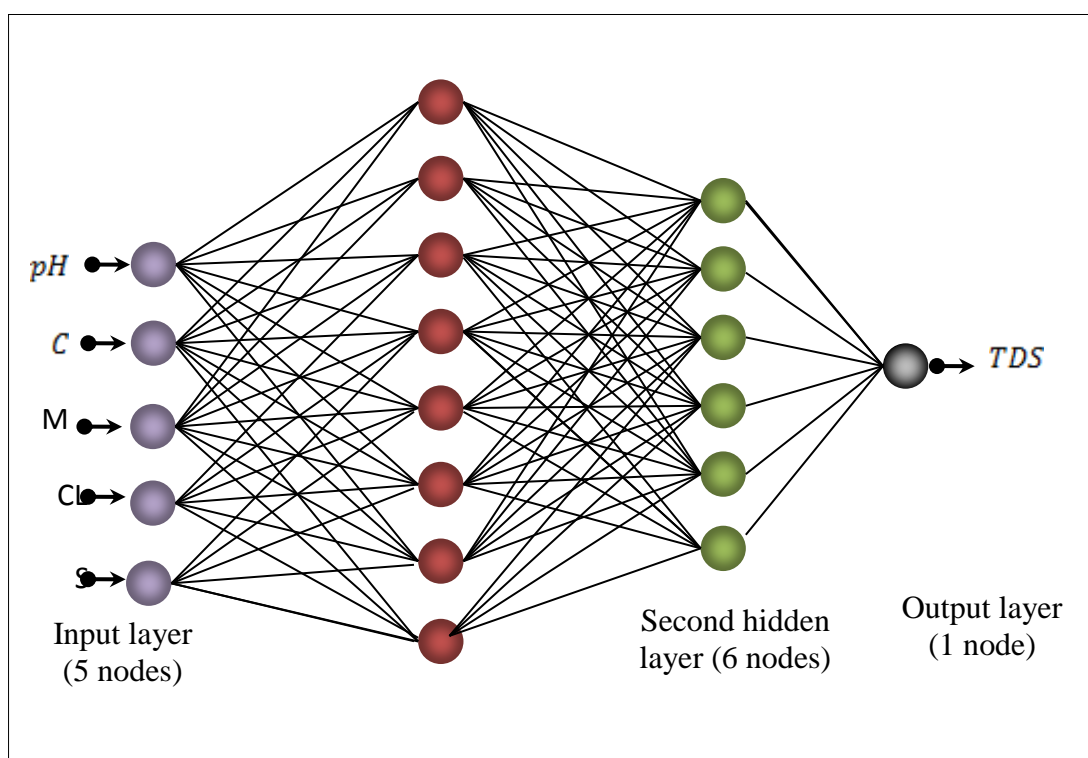


Figure 1 Configuration of Neural Network (3-7-5-2)

2.2 Normalizing Input and Output Data Set

The input and output data sets should be normalized before they are applied to the neural network so as to limit the input and output values within a specified range. This is due to the large difference in the values of the data provided to the neural network. Besides, the activation function used in the back propagation neural network is a hyperbolic tangent function, the lower and upper limits of this function are -1 and +1 respectively.

In this work, the used function for normalization is [10]:

$$pn_i = 2[p_i - p_{\min}/p_{\max} - p_{\min}] - 1 \quad (1)$$

Where: p_i is the value of i -th variable, p_{\min} is the minimum value of p_i and p_{\max} is the maximum value of p_i .

2.2 Optimization Technique and Error Estimates

Neural network functions depend non-linearly on their weights and so the minimization of the corresponding error function requires the use of iterative non-linear optimization algorithms. These algorithms make use of the derivatives of the error function with respect to the weights of the network. After completing the training process, the model is tested using another batch of data which has not been used in the training set.

The following statistical parameters of significance are calculated, for the present work, at the end of the training and testing calculations :

1. *Mean square error (MSE)*: is a statistical measure of the differences between the values of the outputs in the training set and the output values the network is predicting. The goal is to minimize the value of MSE.
2. *Correlation coefficient (R)*: is a measure of how the actual and predicted values correlate to each other. The goal is to maximize the value of R . The correlation coefficient function can be described as following [11]:

$$R = an(tn'/Q - 1)/sta * stt \quad (1)$$

Where: an and tn' are the normalized outputs and transpose matrix of normalized target data respectively, sta and stt are the standard deviation of the output and target data respectively.

Q is the number of the data in target vector.

2.3 Number of Hidden Layers and Number of Nodes in Hidden Layer

The choice of the number of hidden layers, number of nodes in the hidden layer and the activation function depends on the network application.

It is usually to start with a relatively small number of hidden units and increase it until we are satisfied with the approximation quality of the network. Unfortunately, the network needs to be fully retrained after each modification of its structure. The number of nodes in a hidden layer(s) drastically affects the outcome of the network training [12].

Therefore, trial-and-error approach is carried out to choose an adequate number of hidden layers and number of nodes in each hidden layer. The number of nodes in the hidden layer is selected according to the following rules:

1. The maximum error of the output network parameters should be as small as possible for both training patterns and testing patterns.
2. The correlation coefficient should be as high as possible especially. It is a measure of how well the variation in the output is explained by the targets. If this number is equal to (1), then there is perfect correlation between targets and outputs.

In this study the network is tested with one and two hidden layer configurations with an increasing number of nodes in each hidden layer(s). Different training function types and activation functions are investigated.

In this work, all training algorithms available in *MATLAB* (R2008a) are examined in this investigation. These algorithms are:

1. Conjugate gradient (traincgf, traincgp, traincgb, trainscg).
2. Quasi-Newton (trainbfg, trainoss).
3. Levenberg-Marquardt (trainlm, trainbr).
4. Gradient Descent (traingd, traingdm).
5. Variable Learning Rate (traingdx).
6. Resilient Back propagation (trainrp).

These functions were used for one hidden layer investigation and two hidden layers investigation [13].

The program of this work can be computerized in a three steps as following:

1. The first step is the “*Neural Network*” program that is coded in *MATLAB* (R2008a) language realizes the training and generalization processes of the back propagation network. The structure of this program is shown in Fig. 2. The main variables are stored using the cell arrays. The cell arrays in *MATLAB* are multidimensional arrays whose elements are copies of other arrays, and then the neural network description is extracted and saved in a separate file. The results of this step are suitable values of the weight and the biases.

2. The second step is the “*MATLAB Function*” program that is coded in *MATLAB* (R2008a) also. This function uses the network parameters extracted in step 1 to put the selected model in its operating mode.
3. The third step is the “*Graphical User Interface*” program that is coded using *MATLAB* (R2008a). This program uses the function extracted in step 2 to put this function in its operating mode as shown in Fig(2).

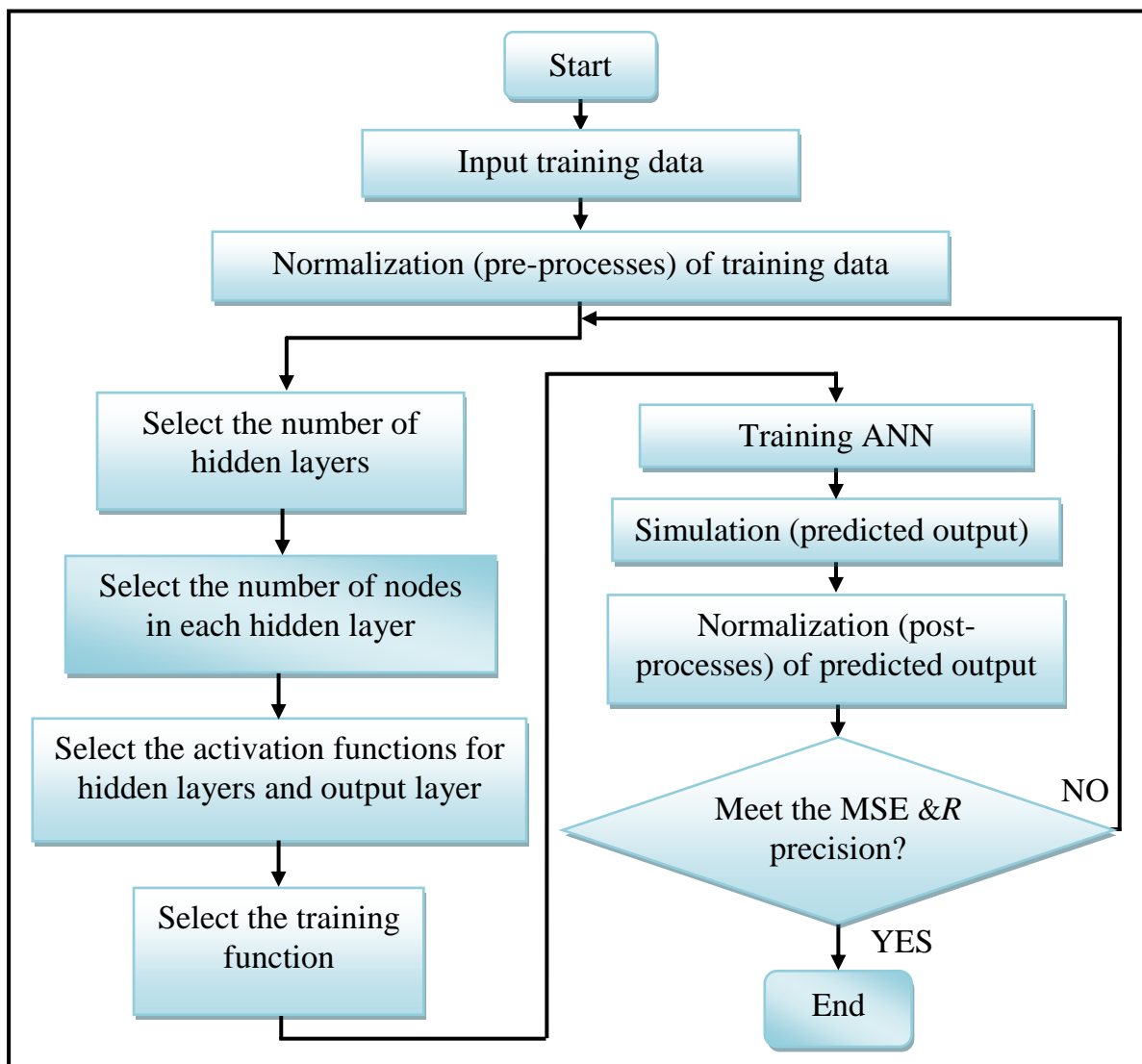


Fig. 2: The Structure of the Neural Network Program

Table (1): Input and Output Parameters

<i>Item</i>	<i>Parameters</i>	<i>Range of Parameters</i>		<i>Units</i>
		<i>From</i>	<i>To</i>	
Input Parameters	pH	6.9	8.48	-
	Calcium Concentration (ppm)	41.88	700	ppm
	Magnesium Concentration (ppm)	21.7	661	ppm
	Chloride Concentration (ppm)	30	1940	ppm
	Sulfate Concentration (ppm)	74	2500	ppm
Output Parameter	Total Dissolved Concentration (TDS) (ppm)	500	6189	ppm

3. Results and Discussions:-

3.1 One Hidden Layer Network:

One hidden layer networks are investigated with different training and activation functions for the hidden and output layer. Different numbers of nodes in each hidden layer from (6 to 12) nodes are used. The performance and regression of these topologies of network for both training and testing are shown in Tables (2,3,4,5,6 and 7).

Table (2): MSE and R for Conjugate Gradient training functions

	Training Function	Node No.	Training data (80%)		Testing data (20%)	
			MSE	R1	MSE	R1
Activation Function : {tansig, purelin}	traincgf	6	0.0155	0.925	0.015	0.9036
		8	0.0153	0.926	0.0159	0.8961
		10	0.0078	0.963	0.01	0.935
		12	0.0078	0.963	0.01	0.935
	traincgp	6	0.015	0.9274	0.0147	0.9033
		8	0.0103	0.9507	0.0113	0.9267
		10	0.006	0.9717	0.0049	0.9672
		12	0.0069	0.9674	0.0091	0.943
	traincgb	6	0.0131	0.9371	0.0174	0.8874
		8	0.0119	0.9431	0.0106	0.9345
		10	0.088	0.9581	0.0086	0.9456
		12	0.0054	0.9745	0.0053	0.9665
	trainscg	6	0.0112	0.9461	0.0167	0.8865
		8	0.01	0.9523	0.012	0.9213
		10	0.0083	0.9605	0.0049	0.9688
		12	0.0059	0.9727	0.0082	0.9546

Table (3): MSE and R for Quasi-Newton training functions

	Training Function	Node No.	Training data (80%)		Testing data (20%)	
			MSE	R	MSE	R
Activation Function : {tansig, purelin}	trainbfg	6	0.0132	0.9366	0.0139	0.9113
		8	0.009	0.9569	0.0111	0.9261
		10	0.0058	0.9724	0.0058	0.9534
		12	0.0072	0.9657	0.0075	0.9511
	trainoss	6	0.0142	0.9314	0.0152	0.9027
		8	0.011	0.9471	0.0152	0.8954
		10	0.0099	0.9534	0.0148	0.9105
		12	0.0069	0.968	0.0098	0.9447

Table (4): MSE and R for Gradient Descent training function

Activation Function : {tansig, purelin}	Training Function	Node No.	Training data (80%)		Testing data (20%)	
			MSE	R	MSE	R
	traingd	6	0.04833	0.74	0.035	0.7376
		8	0.0388	0.7983	0.0277	0.8317
		10	0.0377	0.8042	0.0219	0.8502
		12	0.0377	0.8042	0.0219	0.8502
	traingdm	6	0.0369	0.8095	0.0228	0.8471
		8	0.0438	0.7682	0.0291	0.8004
		10	0.03398	0.8261	0.0197	0.8631
		12	0.0358	0.815	0.0202	0.865

Table (5): MSE and R for Levenberg-Marquardt training function

Activation Function : {tansig, purelin}	Training Function	Node No.	Training data (80%)		Testing data (20%)	
			MSE	R	MSE	R
	Trainlm	6	0.0171	0.9164	0.0148	0.9017
		8	0.0086	0.9591	0.0128	0.9175
		10	0.006	0.9721	0.0064	0.9652
		12	0.0055	0.9741	0.0043	0.9731

Table (6): MSE and R for Variable Learning Rate training function

Activation Function : {tansig, purelin}	Training Function	Node No.	Training data (80%)		Testing data (20%)	
			MSE	R	MSE	R
	Traingdx	6	0.0176	0.9144	0.0179	0.8826
		8	0.0172	0.9161	0.017	0.8888
		10	0.0186	0.9091	0.014	0.9066
		12	0.0149	0.9282	0.0177	0.8844

Table (7): MSE and R for Resilient Backpropagation training function

Activation Function : {tansig, purelin}	Training Function	Node No.	Training data (80%)		Testing data (20%)	
			MSE	R	MSE	R
	Trainrp	6	0.0186	0.909	0.0207	0.8568
		8	0.0118	0.9433	0.0147	0.9054
		10	0.0102	0.9515	0.011	0.9296
		12	0.0081	0.9613	0.009	0.9413

It can be seen that From Tables (2,3,4,5,6 and 7), the networks with (12) nodes in the hidden layer and activation function as hyperbolic tangent (*tansig*) and (*purelin*) function for hidden and output layers respectively gives best performance and correlation coefficient for networks with training function (traincgf, traincgb, trainscg, trainoss, traingd, trainlm and trainrp)while networks with (10) nodes in the hidden layer and training function (traincgp, trainbfg, traingdm and traingdx) gives best results than other. The best performance network for predicting TDS concentration in water is the one with (12) nodes in hidden layer with training function (trainlm).

3.2 Two Hidden Layers Investigation

Artificial Neural Networks(ANNs) with Two hidden layers and different training and activation functions for each layer are investigated. Different nodes numbers in each hidden layer from (6 to 12) nodes in the first hidden layer and (5-10) in the second one are choosing. The performance and regression of these topologies for both training and testing are shown in Tables (8, 9, 10, 11, 12 and 13).

Table (8): MSE and R for Conjugate Gradient training functions

	Training Function	Node No.	Training data (80%)		Testing data (20%)	
			MSE	R	MSE	R
Activation Function : {tansig, tansig, purelin}	traincgf	6-5	0.0052	0.9758	0.0111	0.9291
		8-6	0.0023	0.9896	0.0081	0.9516
		10-8	8.831e-4	0.9959	0.0026	0.9828
		12-10	4.422e-4	0.9979	6.477e-4	0.9963
	traincgp	6-5	0.0088	0.9587	0.0119	0.9295
		8-6	0.0128	0.9389	0.0148	0.9119
		10-8	0.0021	0.9903	0.0041	0.9734
		12-10	0.0019	0.9911	0.0024	0.9848
	traincgb	6-5	0.0064	0.97	0.0111	0.931
		8-6	0.0015	0.9927	0.0034	0.9927
		10-8	5.4205e-4	0.9975	0.0014	0.9912
		12-10	2.3210e-4	0.9986	2.3210e-4	0.9986
	traincsg	6-5	0.0027	0.987	0.0071	0.9528
		8-6	0.0019	0.9911	0.0043	0.9717
		10-8	3.923e-4	0.9982	8.54e-4	0.9944
		12-10	3.052e-5	0.9999	1.485e-5	0.9999

Table (9): MSE and R for Quasi-Newton training functions

	Training Function	Node No.	Training data (80%)		Testing data (20%)	
			MSE	R	MSE	R
Activation Function : {tansig, tansig, purelin}	trainbfg	6-5	0.0022	0.9896	0.0064	0.9599
		8-6	0.001	0.9952	0.002	0.9872
		10-8	2.013e-4	0.9991	3.255e-4	0.9979
		12-10	1.588e-4	0.9993	1.939e-4	0.9987
	trainoss	6-5	0.0039	0.9817	0.0071	0.9561
		8-6	0.0047	0.9777	0.0052	0.9667
		10-8	8.796e-4	0.9959	0.0021	0.9863
		12-10	8.018e-4	0.9962	9.428e-4	0.9939

Table (10): MSE and R for Levenberg-Marquardt training function

Activation Function : {tansig, tansig, purelin}	Training Function	Node No.	Training data (80%)		Testing data (20%)	
			MSE	R	MSE	R
	trainlm	6-5	0.003	0.9859	0.0027	0.9839
		8-6	3.132e-4	0.99895	5.042e-4	0.9967
		10-8	2.49e-22	1	3.807e-22	1
		12-10	3.044e-24	1	4.245e-24	1

Table (11): MSE and R for Gradient Descent training function

Activation Function : {tansig, tansig, purelin}	Training Function	Node No.	Training data (80%)		Testing data (20%)	
			MSE	R	MSE	R
	Traingd	6-5	0.0463	0.7529	0.028	0.8062
		8-6	0.0385	0.8002	0.0279	0.8031
		10-8	0.0384	0.8214	0.0175	0.8837
		12-10	0.0287	0.8555	0.025	0.8185
	Traingdm	6-5	0.038	0.798	0.026	0.8126
		8-6	0.0186	0.9096	0.0197	0.8653
		10-8	0.0348	0.8214	0.0175	0.8837
		12-10	0.0379	0.8032	0.025	0.8213

Table (12): MSE and R for Variable Learning Rate training function

Activation Function : {tansig, tansig, purelin}	Training Function	Node No.	Training data (80%)		Testing data (20%)	
			MSE	R	MSE	R
	traingdx	6-5	0.0138	0.9338	0.019	0.877
		8-6	0.0147	0.9289	0.0127	0.9157
		10-8	0.0132	0.9396	0.016	0.8991
		12-10	0.0089	0.9577	0.0103	0.9366

Table (13): MSE and R for Resilient Backpropagation training function

Activation Function : {tansig, tansig, purelin}	Training Function	Node No.	Training data (80%)		Testing data (20%)	
			MSE	R	MSE	R
	trainrp	6-5	0.0065	0.9692	0.0107	0.9327
		8-6	0.0061	0.9714	0.0091	0.9458
		10-8	0.0047	0.9776	0.0057	0.9633
		12-10	0.0012	0.9944	0.0027	0.9853

It can be seen that tables from (8) to (13) show that the response of network with different training functions changed with variation of nodes in the first and the second hidden layers. The training function selected here is conjugate gradient back propagation type (*TRAINSCG*) which indicated high regression and best performance with lowest mean square error. Other functions are investigated and compared in the present work. The transfer function (*trainlm*) with node (14-10) and (15-12) have high MSE values but its performance suffer from overfitting data, therefore it is not good function compared with other functions.

The selected training function (*TRAINSCG*) in this study must be examined with another different activation function to complete this investigation as showing in Table (14) and Fig. (14), which are shown that (*tansig, tansig, purelin*) activation function arrangement gives the best performance and regressions for both training and testing phases.

**Table (14): MSE & Regression with Different Arrangements of Activation Functions
Each of Two hidden layer (12-10) Network with *TRAINSCG* Training Function.**

<i>TRAINSCG</i> Training Function	<i>Arrangements of Activation Functions</i>				
	(<i>tansig</i> , <i>purelin</i> , <i>purelin</i>)	(<i>tansig</i> , <i>tansig</i> , <i>purelin</i>)	(<i>tansig</i> , <i>tansig</i> , <i>tansig</i>)	(<i>purelin</i> , <i>tansig</i> , <i>tansig</i>)	(<i>tansig</i> , <i>purelin</i> , <i>tansig</i>)
MSE (train)	0.0066	3.052e-5	1.7649e-4	0.0045	0.0052
MSE (test)	0.0074	1.485e-5	1.5775e-4	0.0132	0.0081
R (train)	0.9688	0.9999	0.9992	0.9788	0.9751
R (test)	0.9540	0.9999	0.9990	0.9172	0.9546

The analysis of these results lead to the fact that the training function (*trainscg*) with activation functions (*tansig*) and (*purelin*) for the two hidden layers and output layer respectively between all other different arrangements of neural networks gives the best MSE and correlation coefficients for both training and testing than other. Therefore, this network can be selected as a suggested network for this study.

Figures (3, 4 and 5) show the regression analysis between the output of neural network and the corresponding target for training, testing and overall data respectively for Total Dissolved Solids Concentration in water. Outputs are plotted versus the targets as open circles. The solid line indicates the best linear fit and the broken line indicates the perfect fit (output equals target). The high regression analysis ($R=0.999$) is obtained in these figures which obtained in network with (12 and 10) nodes in the first and second hidden layer respectively using (*trainscg*) as transfer function with activation function (*tansig*, *tansig* and *purelin*).

Figures (6) and (7) show the behavior of ANN to predict Total Dissolved Solids Concentration (TDS) for training and testing data set respectively. It can be seen that the actual and predicted values are close to each other, can concluded that ANN model has high accuracy levels of prediction.

Figure (8) shows training and testing performance of the best two hidden layer network. The performance of a trained network can be measured to some extent by the errors on the training and testing sets, but it is often useful to investigate the network response in more detail. One option is to perform a regression analysis between the network response and the corresponding targets. Figure (9) represents a comparison between the best one and two hidden layers performance which gives good error for the network with two hidden layer using training function as *trainscg*.

Figure (10) studied the variation of Mean Square Errors (MSE) with different activation functions each of (5-12-10-1) network with *trainscg* training function, it can be seen that the function (*tansig* - *tansig* - *purelin*) indicated high performance than other with MSE of ($3.052e-5$) to the best network.

Figure (11) represent Graphical User Interface (GUI) of the Neural Network Program which act as an artificial neural network model to predict Total Dissolved Solids Concentration (TDS) in (ppm) at formation behavior of another data to another input water quality values inside and outside training data range respectively.

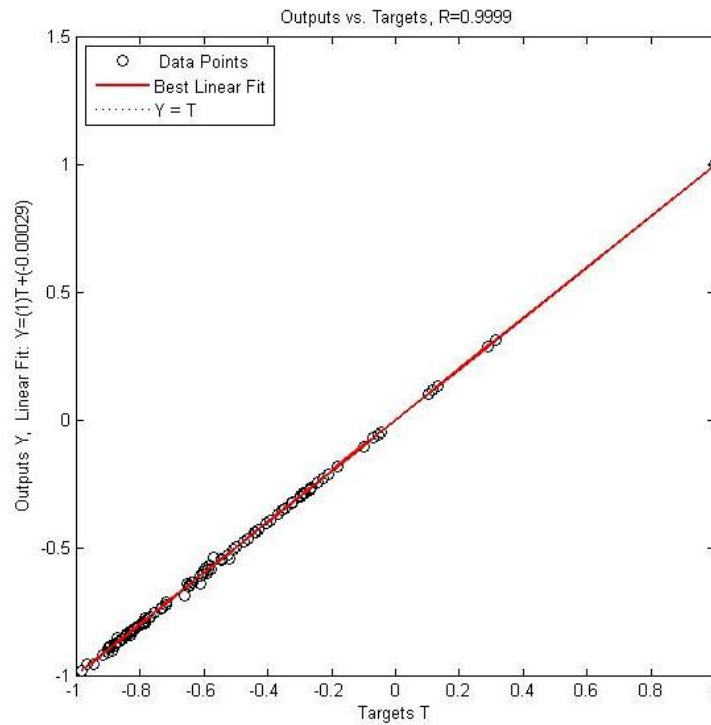


Fig.(3) : Training TDS Regression of the Two Hidden Layer (trainscg) Network

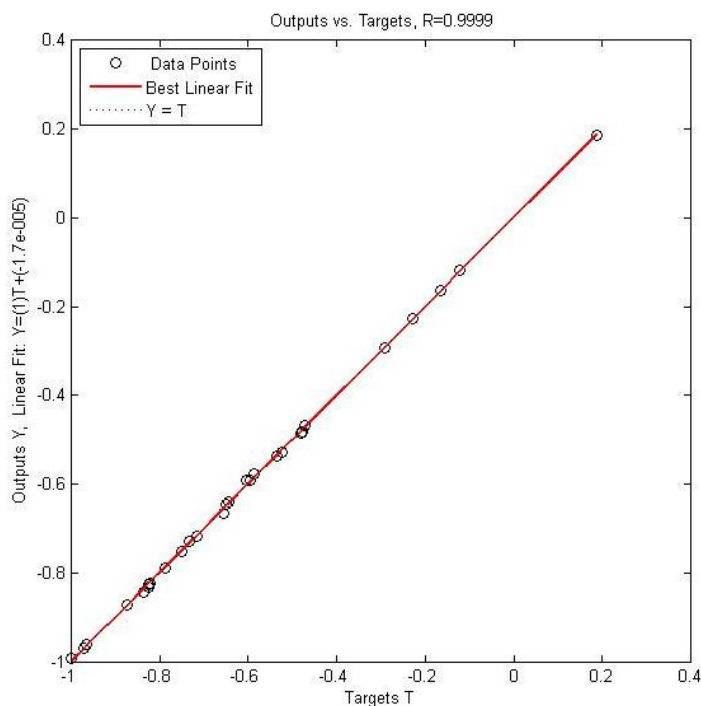


Fig. (4) : Testing TDS Regression of the Two Hidden Layer (trainscg) Network

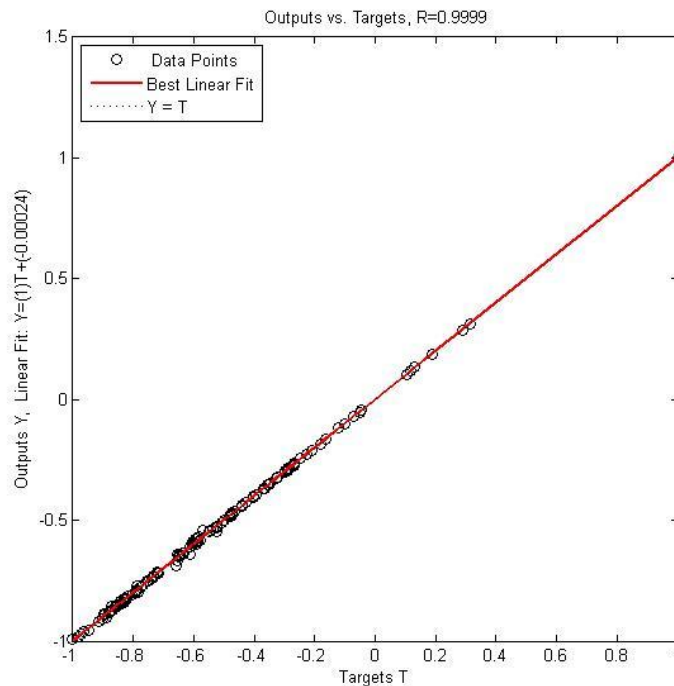


Fig. (5) : Overall TDS Regression of the Two Hidden Layer (trainscg) Network

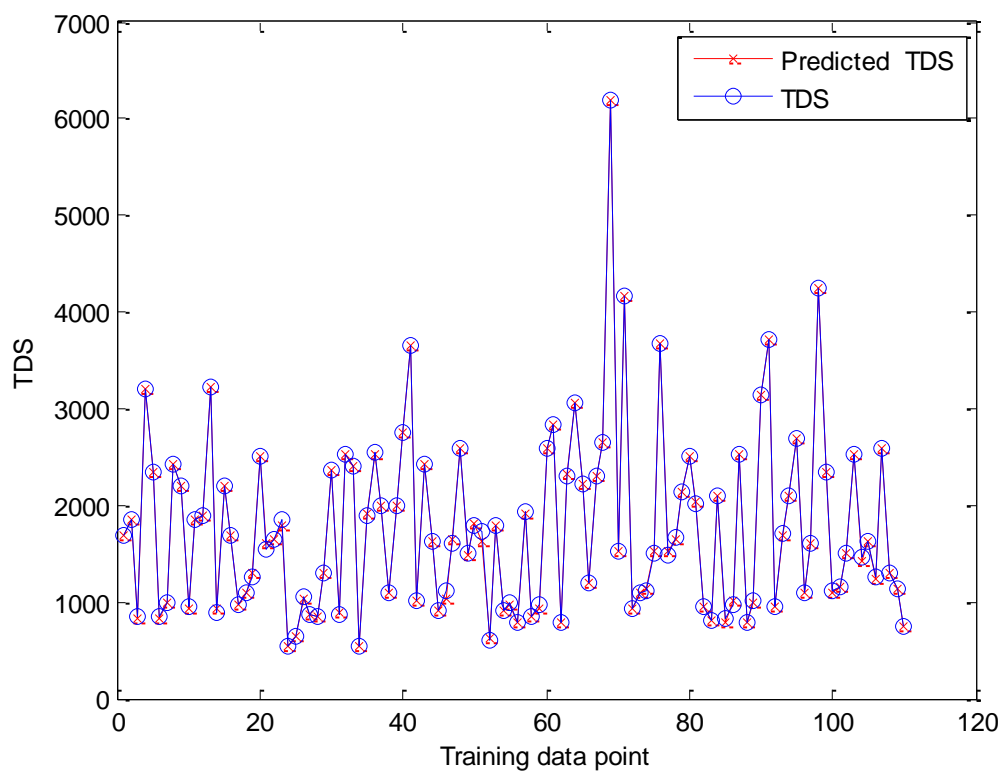


Fig. (6): Training Behavior of Predicted TDS.

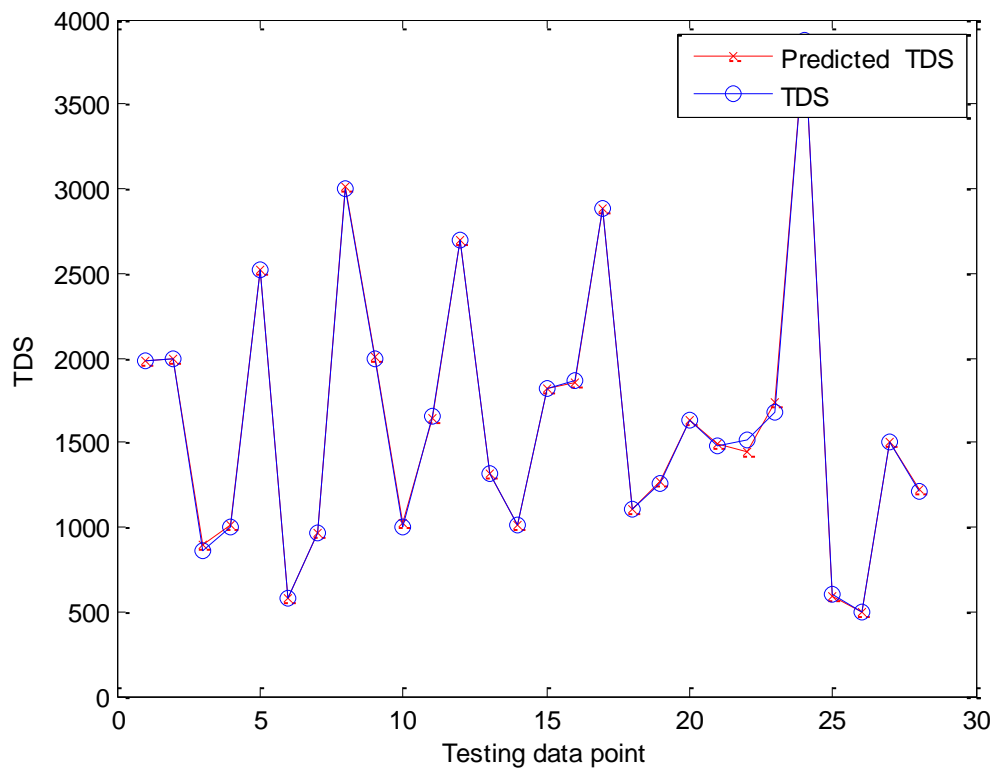


Fig (7): Testing Behavior of Predicted TDS.

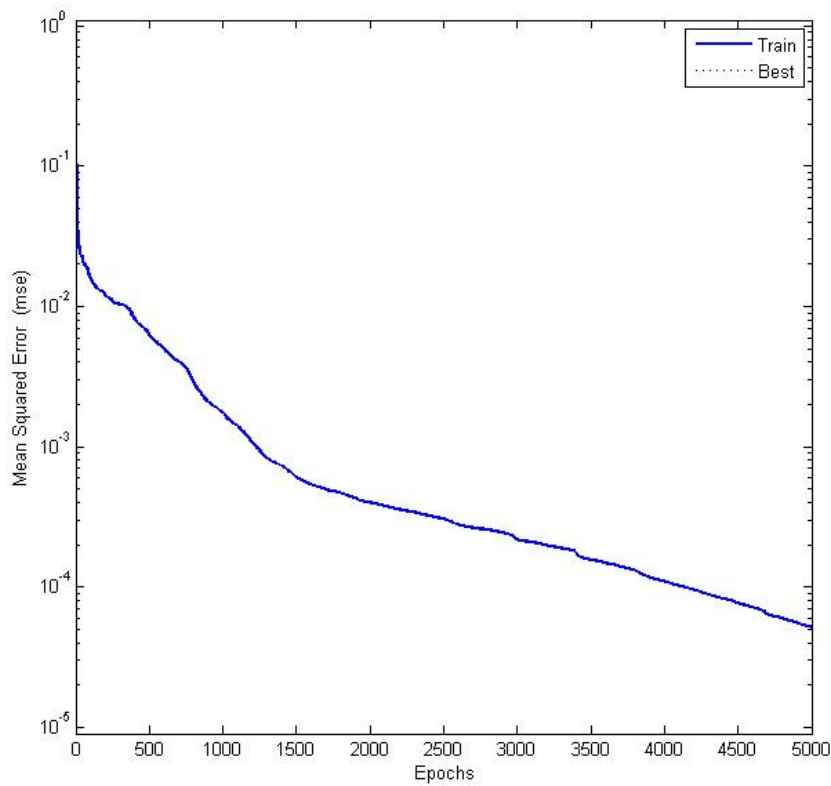


Fig. (8) : Training MSE vs. Epochs of the Best Two Hidden Layer Network (trainscg)

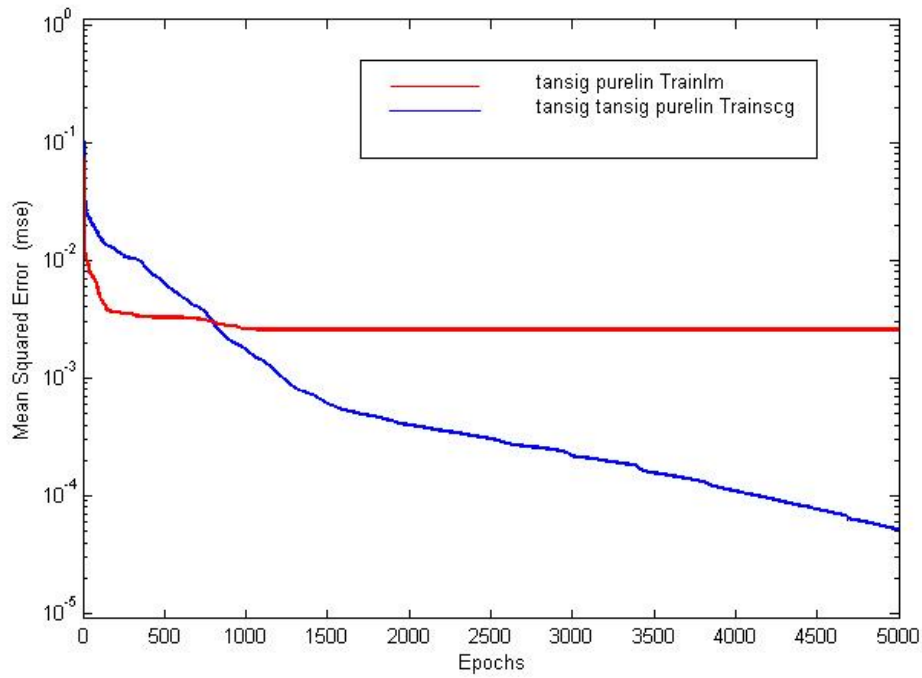


Fig. (9) : Comparison between the Best One and Two Hidden Layers Networks Performance

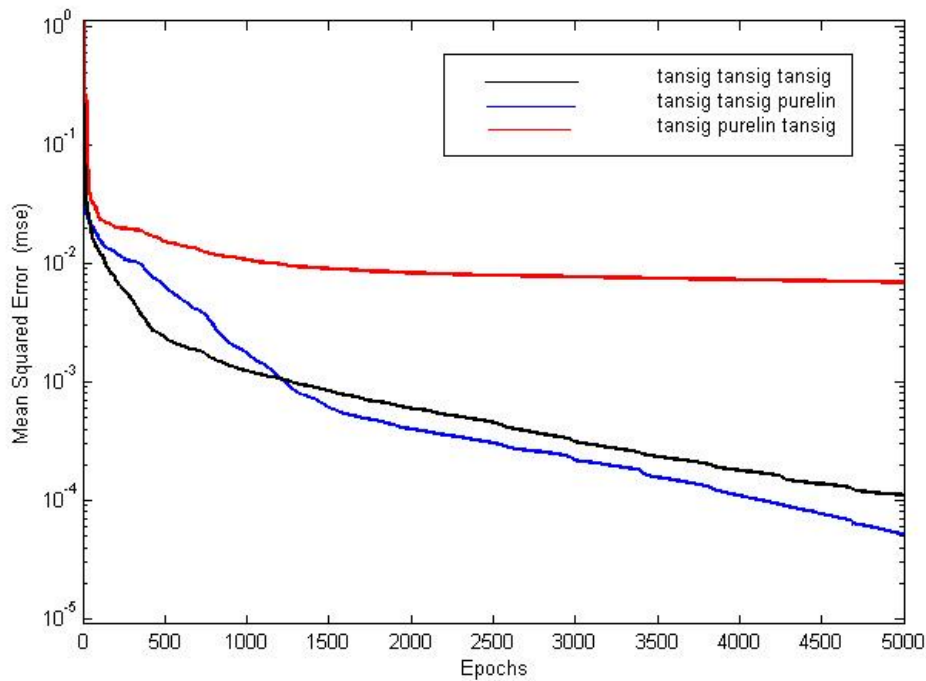


Fig. (10) : Comparison between Activation Function for the (trainscg) in Two Hidden Layer Network

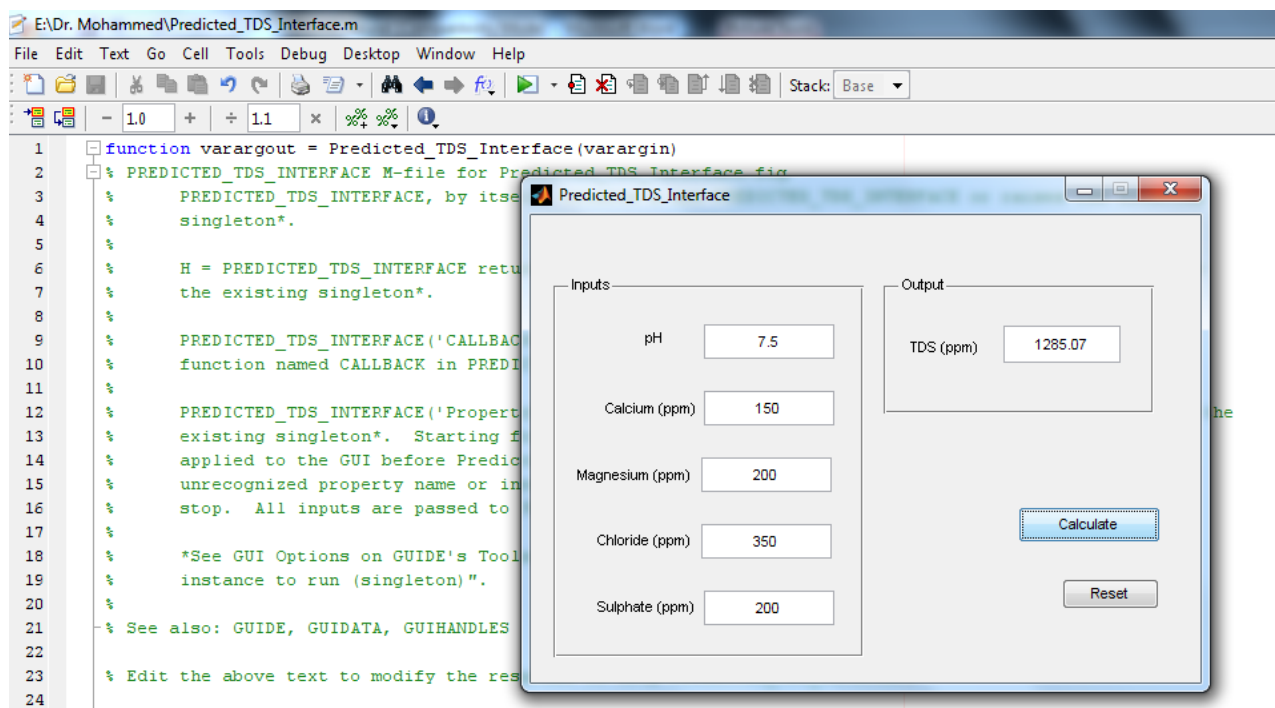


Figure (11) : Graphical User Interface (GUI)of the Neural Network Program.

4- Conclusion:

This paper, one and two hidden layer feedforward back-propagation artificial Neural network models were applied for prediction of total dissolved solids in marsh water . a (140) sample data are choose in the ANNs with five input parameters (pH, Calcium, magnesium, chloride and sulphate concentrations) in one and two hidden layers with different network conditions. Results show best performance and regression analysis reached (0.9999) for both training and testing date of this research with two hidden layer (trainscg as training function) with (5-12-10-1) neurons in their layers. Also, the results indicated that ANNs model provided a reliable and simple tool for the prediction of TDS in marsh water. It was concluded that this research can be considered as contribution to an on ongoing effort to develop artificial neural network model to solve water and waste water treatment.

Reference:

- 1- Mohammed D. (2011) "Assessment Of Toxic Materials In Sunaf Marsh (Alkhawisa Village)", J.Thi-Qar Sci vol. 3 No.1.
- 2- Kanani S., Asadollahfardi G. and Ghanbari A. (2008) " Application of Artificial Neural Network to Predict Total Dissolved Solid in Achechay River Basin", World Applied Sciences Journal 4 (5): 646-654.
- 3- Zhang, Q., and Stanley, S.J. (1997). "Forecasting raw-water quality parameters for the North Saskatchewan River by neural network modeling. Water Research", **31**(9): 2340–2350.
- 4- Eman Abd Mohammed (2010) " Water Quality Monitoring Of Al-Hawizeh Marsh", Al-Qadisiya Journal For Engineering Sciences Vol. 3 No. 3.
- 5- Riyadh Z. and Shaimaa U. (2009) "Effect Of Al Huwayza Marsh Boundary Configuration On The Velocity Patterns And Water Quality Distribution", Vol. 15 No.1
- 6- Mohammed D. (2011) " Assessment Of Toxic Materials In Sunaf Marsh (Alkhawisa Village)", J.Thi-Qar Sci vol. 3 No.1.
- 7- Mohammed D., Kaissar I. and Haider A. (2012) "Effect of Chemical and Physical Parameters of Almasab Alaam Drainage on Properties of Marsh water in South of Iraq" accepted in Al-Qadisiya Journal For Engineering Sciences
- 8- Martin T. (1996) " Neural Network Design", PWS Publishing company.
- 9- ASCE Task Committee on Application of Artificial Neural Networks in Hydrology, 2000a. Artificial Neural Networks in Hydrology: Preliminary Concepts. Part I, J. Hydrologic Engrg., ASCE, 5 (2): 115-123.
- 10- Howard Demuth (2008) " Neural Network Toolbox 5 User's Guide", The Math Works, Inc.
- 11- Hornik, K.M., M. Stinchcombe and H. White, 1989. Multilayer Feedforward Networks are Universal Approximators. Neural Networks, Vol: 2.
- 12- Jain, A.K., Mao, J.C., and Mohiuddin, K.M. (1996). "Artificial neural networks: a tutorial. Computer", **29**(3): 31–44.
- 13- Rafiq M.Y., Bugmann G. and Easterbrook D.J (2001) " Neural Network Design for Engineering Application" Journal of computers and Structures", Vol. 79 No. (17), 1451-1552.

Durability of Concrete Incorporating Corrosion Inhibitors Exposed to a Salt Solution of $Cl^- + SO_4^{2-}$

Hayder Majeed Oleiwi

Civil Engineering Department

College of Engineering

University of Thi Qar

haider_alomary@yahoo.com

Abstract:

Laboratory investigations were performed in order to assess the effectiveness of three types of inhibitors, calcium nitrite, ethanolamine and Sika ferro gard 901 (commercial inhibitor) with 1%, 2% and 3% concentration by weight of cement for each inhibitor to retarding corrosion of steel embedded in concrete. Concrete specimens were used to assess the effects of corrosion inhibitors on the compressive and tensile strength of concrete and corrosion of reinforcement.

Some of the specimens were subjected to wetting and drying cycles and reinforcement corrosion was evaluated by measuring corrosion potentials and corrosion current density. Other concrete specimens were immersed in the salt ($Cl^- + SO_4^{2-}$) solution and reinforcement corrosion was accelerated by impressing an anodic potential of +12 V from a DC power supply and measuring the time-to-cracking of the concrete specimens. The results indicated that the concrete specimens incorporated corrosion inhibitors of calcium nitrite and Sika ferro gard 901 did not adversely affect the compressive and tensile strength of concrete. Furthermore, the time-to-cracking in specimens contains those two inhibitors (calcium nitrite and Sika ferro gard 901) were higher. Two percent of calcium nitrite followed by three percent of Sika ferro gard 901 were efficient in delaying the initiation of reinforcement corrosion and reducing the rate of reinforcement corrosion current density in the concrete specimens, while all the percentages of ethanolamine corrosion inhibitor were ineffective to delay corrosion of the rebar under the conditions of the study and it's adversely affect the strength.

Keywords: concrete, strength, corrosion inhibitors, corrosion potential, current density

ديمومة الخرسانة المخلوطة بمثبطات التآكل والمعرضة إلى محلول ملحي من الكلوريدات والكبريتات
المستخلص: فحوصات مختبرية أنجزت لتقييم فعالية ثلاثة أنواع من المثبطات (نتريت الكالسيوم و ايثانول امين و سیکا فيرو كارد 901 (مثبط تجاري)) بنسب 1% و 2% و 3% من وزن السمنت لكل مثبط لتأخير التآكل في الحديد المطمور في الخرسانة. تم استخدام نماذج خرسانية لتقييم تأثير مثبطات التآكل على مقاومة الانضغاط ومقاومة الشد وتآكل حديد التسليح.

تم تعريف بعض النماذج إلى دورات من الترطيب والتجفيف لغرض تقييم التآكل في حديد التسليح من خلال قياس فرق جهد التآكل وقياس كثافة تيار التآكل (بطريقة فقدان الوزن). نماذج أخرى غمرت في المحلول الملحي الحاوي على أملاح الكلوريدات والكبريتات وتم تسريع التآكل في حديد التسليح عن طريق تسليط فرق جهد أنودي بمقدار 12 فولت وحساب وقت ظهور التشققات في النماذج الخرسانية. أشارت النتائج إلى أن النماذج الخرسانية الحاوية على مثبطات التآكل نترت الكالسيوم وسيكا فيروكارد 901 لم تؤثر سلباً على مقاومة الانضغاط ومقاومة الشد. بالإضافة إلى ذلك، فإن وقت ظهور التشققات في النماذج الحاوية على هذين المثبتين (نترت الكالسيوم و سيكا فيروكارد 901) كان أعلى. استخدام 2% من نترت الكالسيوم و 3% من سيكا فيروكارد 901 كان الأكثر فعالية في تأخير بدء التآكل وكذلك في تقليل كثافة تيار التآكل لحديد التسليح في النماذج الخرسانية، بينما كانت جميع النسب المستخدمة للمثبط ايثانول امين غير فعالة في تأخير التآكل تحت ظروف الدراسة و له تأثير ضار على المقاومة.

1. Introduction

Corrosion of steel in concrete is one of the major causes of premature deterioration of reinforced concrete structures, leading to structural failure and the useful service-life of the structures is drastically reduced because of this phenomenon^[1]. When these structures are exposed to aggressive substance containing chloride, the corrosion faults are frequently induced by the presence of chloride ions, these ions cause localized breakdown of the passive film that initially forms on the steel due to the high pH of the concrete interstitial electrolyte. Once corrosion has initiated accumulation of corrosion products occurs on the steel surface. Since these products occupy a volume several times larger than that of the original steel^[2], thus, the result is, an increase of the internal tensile stresses that generally induce cracking and spalling of the concrete cover. This situation facilitates further intrusion of aggressive agents and the consequent acceleration of the corrosion process.

There are several sources of chlorides, chlorides incorporated in the concrete when it is mixed (e.g. From salty aggregated and salty mixing water) and chlorides penetrating into concrete from the environment (e.g. From sea water, salty ground water and sea spray)^[3]. To minimize the corrosion processes a number of procedures can be assessed such as coating of concrete surface, surface treatment of the rebars, cathodic protection, chloride extraction and use of corrosion inhibitors.

ACI 116R-85 defines a corrosion inhibitors as a chemical compound, either liquid or powder, can be mixed within the fresh concrete as an admixture, usually in very small concentrations, in order to reduce the risk of steel corrosion in reinforced concrete^[4].

The corrosion inhibiting admixtures should not be as an alternative to the design specifications for durable concrete, but to increased protection against corrosion^[5]. Corrosion inhibitors can be divided into three types: anodic (e.g. Calcium nitrite, Sodium nitrite, Sodium benzoate, Sodium chromate), cathodic (e.g. sodium hydroxide, sodium carbonate, Phosphates, silicate and polyphosphates), and mixed (e.g. amine and aminoalcohol), depending on whether they interfere with the corrosion reaction preferentially at the anodic or cathodic sites or whether both are involved^[6].

Several studies have been accomplished to evaluate the effectiveness of chemical admixtures in inhibiting reinforcement corrosion^[7-9]. Early studies were concentrated on sodium nitrite, potassium chromate, sodium benzoate, and stannous chloride. Later work concentrated mainly on calcium nitrate. Craig and Wood^[7], studied sodium nitrite, potassium chromate, and sodium benzoate using the polarization technique and found that sodium nitrite was the most effective corrosion inhibitor, but it had harmful effects on concrete strength. Similar results were also reported by Treadaway and Russel^[8] who found that sodium nitrite inhibited corrosion of steel bars in the presence of chlorides, whereas sodium benzoate did not. Rosenberg et al.^[10], studied the effect of calcium nitrite as an inhibitor in reinforced concrete. They used polarization techniques for evaluation of the inhibitors and reported that the relative corrosion rates for samples soaked in a saturated sodium chloride solution for 90 days with 2% and 4% admixed calcium nitrite were about a factor of 15 times lower than those without the calcium nitrite admixture.

Tomazawa et al.^[11], also supported the effectiveness of calcium nitrite as a corrosion inhibitor in concrete. In accelerated tests with wetting and drying cycles at 80°C, calcium nitrite was found to be an effective inhibitor for long-term exposures even in marine environments.

Collins et al.^[12], evaluated several inhibitors including (1) a calcium-nitrite-based inhibitor, (2) a monofluorophosphate-based inhibitor, (3) sodium tetraborate, (4) zinc borate (5) a proprietary oxygenated hydrocarbon produced from an aliphatic hydrocarbon, (6) a proprietary blend of surfactants and amine salts (MCI2020 which migrate through concrete), and (7) a proprietary alkanolamine inhibitor (MCI 2000). The results of the study, which involved monitoring of corrosion, compressive strength and resistivity, showed that the calcium-nitrite-based inhibitor was the most promising to mitigate corrosion in a repaired structure after removal of chloride-contaminated old concrete. On the other hand, both borate compounds were found to retard the setting of Portland cement.

Prowell et al.^[13], evaluated some of the inhibitors studied by Collins et al.^[12] and conducted ponding experiments where they monitored corrosion by measuring the half-cell potential, linear polarization resistance, and chloride ion concentration for a period of 325 days. They reported that two proprietary inhibitors Alox 902 and MCI 2020 were the best performers.

Berke and Hicks^[14], published long-term data to show the levels of chloride that a given level of calcium nitrate can protect. They also indicated that once corrosion initiates, the rates are lower with the addition of calcium nitrate.

Jamil et al.^[15], conducted electrochemical impedance measurements in order to obtain information on the corrosion behavior of reinforcing steel in the presence of a penetrating amino-alcohol corrosion inhibitor. The investigation was performed in solutions contaminated with chlorides, in the presence of the inhibitor. The electrochemical results indicated that the inhibitor is able to penetrate through mortar, minimizing steel corrosion.

The significance of using corrosion inhibitors in aggressive exposures is ascribable to the fact that data are lacking in the performance of reinforced concrete that is subject to both chloride and sulfate salts.

This investigation was conducted to evaluate the effectiveness of three different types of corrosion inhibitors in reducing reinforcement corrosion in concrete subjected to chloride and sulfate salts with percentage equivalent to those present in soil and underground water in the southern parts of Iraq. The performance of the selected inhibitors in reducing reinforcement corrosion was evaluated by adopting various techniques.

2. Experimental Works

2-1: Materials and Mixes

Sulfate resistance cement (Type V) was used, the chemical composition and physical characteristics are given in tables 1 and 2, which indicate compliance with the requirements of Standard Iraqi Specification 5/1984^[16].

Table 1: Chemical composition of cement*

Chemical components	CaO	SiO ₂	Al ₂ O ₃	Fe ₂ O ₃	Lime Saturated Factor	MgO	SO ₃	L.O.I	Insoluble residues	C ₃ A
Used cement, %	62	24	4	5	0.75	4.8	1.78	2.7	0.92	2.15
Limit of Iraqi specification No.5/1984, %	-	-	-	-	0.66-1.02	≤ 5	≤ 2.5	≤ 4	≤ 4	≤ 3.5

Table 2: Physical characteristics of cement*

Physical properties	Test results	Limit of Iraqi specification No. 5/1984, %
Setting time, min.		
-Initial setting	121	≥ 45
Compressive strength, MPa		
3 days	19	≥ 15
7 days	23.5	≥ 23

*: This test was done by construction laboratory at College of Engineering- University of Thi Qar.

Natural sand of 4.75 mm maximum size complying with the Standard Iraqi Specification 45/1984^[17] has been used. The sieve analysis is given in table 3. The coarse aggregate is crushed gravel with a maximum size of 20 mm has been used and its comply with Iraqi specification 45/1984, table 4. Tap water was used for mixing and curing operations. Steel deformed bars, ϕ 12 mm, conforming to ASTM-A615/A 615-06^[18] specifications were used. The mechanical properties of steel are shown in table 5.

Table 3: Grading of sand

Sieve size, mm	10	4.75	2.36	1.18	0.6	0.3	0.15
Percentage passing	100	99	90	75	52	15	2
Limits of Iraqi Specification No. 45/1984 (Zone 2)	100	90-100	75-100	55-90	35-59	8-30	0-10

Table 4: Grading of gravel

Sieve size, mm	37.5	20	10	4.75
Passing, %	100	99	57	2
Limits of Iraqi Specification No. 45/1984 (5-20) mm	100	95-100	30-60	0-10

Table 5: Mechanical properties of steel bars*

Test results for steel bars		ASTM-A615/A 615-06 requirements
Nominal diameter, mm	12	-
Yield strength, MPa	566	≥ 420
Tensile strength, MPa	637	≥ 620
Elongation, %	10	Min. 9

*: This test was done by construction laboratory at College of Engineering- University of Thi Qar.

The mix proportion by weight of cement, fine and coarse aggregate were (1:1.72:2.8). The ingredient proportions are kept constant throughout the work. The cement content was 390 kg, w/c ratio was 0.52 for all concrete specimens.

Three types of inhibitors were used in this work (calcium nitrite (inorganic compound), ethanolamine(organic compound) and sika ferro gard 901(combination of organic and inorganic inhibitors)) with percentage of 1%, 2% and 3% by weight of cement for each inhibitor.

2-2: Preparation of The Salt Solution ($\text{Cl}^- + \text{SO}_4^{2-}$)

Pure NaCl, $\text{CaCl}_2 \cdot 2\text{H}_2\text{O}$ and $\text{MgSO}_4 \cdot 7\text{H}_2\text{O}$ with concentration of 4.5%, 0.55% and 1.79%, respectively, were used in preparing the solution to give a concentration of Cl^- equal to 30000 ppm and SO_4^{2-} equal to 7000 ppm to simulate sulfate and chloride salts in soil and underground water in the southern parts of Iraq according to the report of the National Center for Geological Survey ^[19]. Potable water was used as a solvent for these salts.

2-3: Specimens Details

100 mm x 100 mm x 100 mm concrete cubes were prepared for compression strength, concrete cylinders 150 mm diameter and 300 mm high were cast for tensile strength and reinforced concrete specimens of 100 x 100 x 100 mm with a centrally placed 12 mm diameter reinforcing steel bar of 50 mm long were cast for electrochemical measurements (corrosion assessment). Copper wire is connected to the steel rebar embedded in concrete for electrical connections. The specimens were cast with and without inhibitors ranging from 1% to 3% by weight of cement. Three specimens for each percentage of the corrosion inhibitors were tested, the specimens were covered with a nylon sheet to minimize evaporation during 24 hours after casting. Thereafter, the specimens were removed from the mould and cured in potable water for 27 days.

3. Techniques Used

3-1: Compressive Strength

After curing (24 hr. in air and 27 days in potable water) the specimens of compressive strength were tested according to BS 1881: Part 116: 1983^[20].

3-2: Tensile Strength

ASTM C496-96^[21] was adopted to test the concrete specimens for tensile strength after curing.

3-3: Half-Cell Potential (Corrosion Potential)

In normal conditions, the evolution of salt ingress is slow and has an evolution rate measured in years. In order to accelerate this process. After 28 days of curing, the specimens were exposed to sulfate and chloride solution using the wetting and drying cycles, consisting of 8 days immersed in the solution followed by 7 days drying period in an open atmosphere. The corrosion potentials were measured according to ASTM C876^[22]. Corrosion potentials were measured using a copper– copper sulfate reference electrode (CSE) and a high impedance voltmeter. The positive terminal of the voltmeter was connected to the working electrode (rebar) and the common terminal was connected to the reference electrode (CSE). The cycle in continued for 120 days. From the results, potential with time plot is drawn using the average potentials obtained. According to ASTM C 876 potential values more negative than -350 mV CSE indicate more than 90% probability of corrosion activation. Figure (1) illustrates the test method.

3-4: Accelerated Corrosion

In this technique^[23] the reinforced concrete specimens, after 28 days of curing, is placed in the salt solution of ($\text{Cl}^- + \text{SO}_4^{2-}$) and accelerate the corrosion of steel embedded in concrete by impressing a +12 V fixed anodic potential from a DC power supply until cracking of the specimens. The steel bar in the concrete specimens was connected to the positive terminal of a DC power supply to be anode. 100 x 100 mm stainless steel plate was placed in the solution tank and connected to the negative terminal of a DC power supply to be cathode.

For each specimen, the time taken for initial crack was recorded. Figure (2) illustrates the electrical connection. Battery, charger power 12V and AC conductor were used to overcome main electrical power outage.



Figure1: corrosion potential measurement



Figure 2: Electrical connection for applying a +12 V fixed anodic potential to accelerate the corrosion

3-5: Corrosion current density by weight loss method ^[24]

For the determination of corrosion rate by using of (weight loss) measurement, the initial weight of the rebar samples was taken in 4-digit electronic balance. After the curing period was over, all the specimens were completely immersed in chloride and sulfate solution for 8 days and then subjected to drying for another 7 days in open air at room temperature (wetting and drying cycles). All the concrete specimens were subjected to eight complete cycles.

After testing, the concrete specimens were broken and the reinforcing steel bars were removed. The procedure stated in ASTM G1-03^[25] was adopted for the cleaning of corroded steel bars and for the determination of mass loss. The corrosion rate was calculated using the following equation given in ASTM G1-03^[25].

$$\text{Corrosion rate (mm/year)} = \frac{(K \times W)}{(A \times T \times D)}$$

Where:

K: a constant equal to 8.76×10^4

W: mass loss in grams

A: actual corroded area of steel bar in cm^2 after removal from the specimen and visually examining

T: time of exposure in hours

D: density of steel (7.85 g/cm^3).

Using Faraday's law, the corrosion rate in (mm/year) obtained from mass loss measurement was converted to corrosion current density ($\mu\text{A}/\text{cm}^2$) by assuming uniform corrosion occurred over the steel surface by the following equation ^[24].

$$\text{Corrosion rate (mm/year)} = \frac{(0.00327 \times a \times I_{\text{corr}})}{(n \times D)}$$

Where:

I_{corr} : corrosion current density in $\mu\text{A}/\text{cm}^2$

a: atomic weight of iron (55.84 amu)

n: no. of electrons exchanged in the corrosion reaction (2 for iron)

D = density of steel ($7.85 \text{ g}/\text{cm}^3$).

4. Results and Discussion

4-1: Compressive Strength

Figure (3) shows the average compressive strength of the control concrete specimens (0% corrosion inhibitor) and those containing the corrosion inhibitors after 28 days of curing. The experimentally obtained results showing the value of compressive strength of the specimens incorporating ethanolamine corrosion inhibitors was less than the control specimens and the decrease was about 3.5-13.8%, depending on percentage of inhibitor, the maximum reduction was about 13.8% when 3% of this corrosion inhibitor was added and that is may be due to the retarding effect of the inhibitor and the air content might be slightly increased. This reduction was also confirmed during another research project ^[26].

From Figure (3) it is indicated that there is a slight increase in compressive strength when the percentage of Sika ferro Gard 901 corrosion inhibitor increased and that indicates there is no adverse effect on the compressive strength of concrete.

The strength for concrete containing 2% of calcium nitrite corrosion inhibitor was about 10% higher than for control specimens. In 3% calcium nitrite there was a reduction in the rate of increasing. K.Y. Ann et al.^[27], indicates that an increase in dosage of corrosion inhibitor may not guarantee the properties of concrete. The cause of the reduction in compressive strength is not well known.

4-2: Splitting Tensile Strength

Figure (4) shows the splitting tensile strength with a percentage of inhibitor addition and it illustrates the same behavior for compressive strength with slightly different in reduction or increasing in value of tensile strength. With the 1 % inhibitor addition, there was no adverse effect of tensile strength except ethanolamine inhibitor there was a slight reduction than the control concrete. With 2% of calcium nitrite inhibitor addition, the tensile strength was about 5% higher than the control concrete. With the 3 % inhibitor addition, the figure illustrates that, as the percentage of calcium nitrite and ethanolamine inhibitor level increase, the splitting tensile strength decreases but there is a slight increase with Sika ferro gard 901 inhibitor.

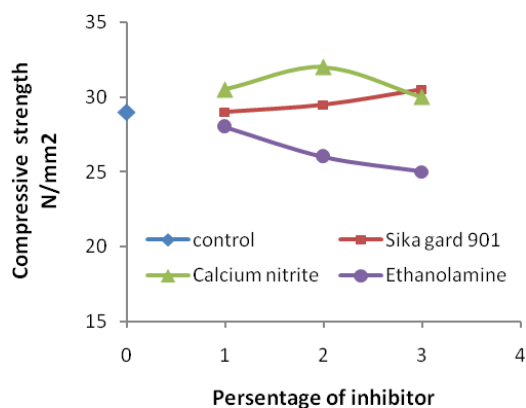


Figure 3: Compressive strength at 28 days of concrete specimens incorporating corrosion inhibitors

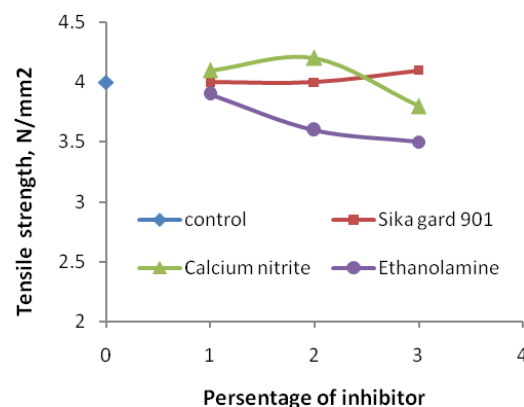


Figure 4: Splitting tensile strength at 28 days of concrete specimens incorporating corrosion inhibitors

4-3: Half-Cell Potential (Corrosion Potential)

The corrosion potentials on steel in the concrete specimens incorporating with 1% of the selected corrosion inhibitors are shown in Figure (5). From the figure it is observed that the corrosion potentials on steel in the all concrete specimens were more negative than -350 mV CSE after about 30 days of exposure indicating the corrosion activation of the rebar based on the ASTM C 876 criteria.

Figure (6) shows the corrosion potential corrosion with time for 2% inhibitor added concrete in the solution under alternate wetting and drying conditions and it illustrates that concrete specimens containing calcium nitrite were less negative -350 mV CSE indicating the passivity of reinforcing steel even after 120 days of the test period and it was -274 mV CSE. Concrete specimens incorporating Sika ferro gard 901 were showing a more negative

potential than -350 mV CSE after 60 days of exposure. Control specimens and that incorporating ethanolamine inhibitor were more negative -350 mV CSE after 30 days of exposure and they were -552 and -605 mV CSE respectively after 120 days of exposure indicating the corrosion activation.

Figure (7) shows the corrosion potential with time for 3% inhibitor added concrete in the salt solution under alternate wetting and drying conditions. In 3% inhibitor added, the control concrete specimens and incorporating with calcium nitrite and ethanolamine are showing a more negative potential than -350 mV CSE after 30 days of exposure indicating the active condition of the rebar while concrete specimens with Sika ferro gard was less negative -350 mV CSE along of the period of exposure. The corrosion potentials on steel in the control, Sika ferro gard 901, calcium nitrite and ethanolamine concrete specimens were -552, -316, -410 and -626 mV CSE respectively after 120 days of exposure. Comparing with control specimens, the potentials in the concrete specimens incorporating sika gard 901 and calcium nitrite were less negative (more positive) than the control concrete specimens.

Figures (6) and (7) can be shown the potentials in the concrete specimens incorporating 3% calcium nitrite were unexpectedly more negative than those incorporating 2% calcium nitrite under the conditions of this study, they were after 120 days of exposure -274 and -410 mV CSE for 2% and 3% calcium nitrite respectively. The same result was obtained by Al-Amoudi et al. ^[22] when they were used concrete specimens prepared with sea water and incorporating calcium nitrite with 2% and 4%.

Figures (5-7) show that the corrosion potential of ethanolamine inhibitor was decreasing and it's more negative than control when increased the percentage of inhibitor, it was after 120 days of exposure conditions -573, -605 and -626 mV CSE with 1%, 2% and 3% of ethanolamine inhibitor respectively, that is means this inhibitor ineffective to delay corrosion of the rebar under the conditions of the study.

4-4: Accelerated Corrosion

The time to cracking of control concrete specimens and those incorporating with corrosion inhibitors are shown in figure 8. From this figure, it can be observed that the time to cracking is maximum in the Specimens incorporating calcium nitrite and Sika gard 901 corrosion inhibitors addition, they were ranged (90-98) hours, indicating the low permeability of the concrete when compared to control and ethanolamine specimens. There was no clear effect to the percentage of inhibitor.

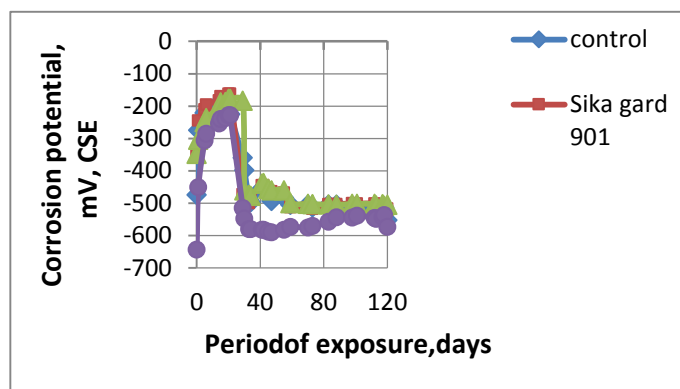


Figure 5: Corrosion potential on steel in the concrete specimens incorporating with 1% inhibitor

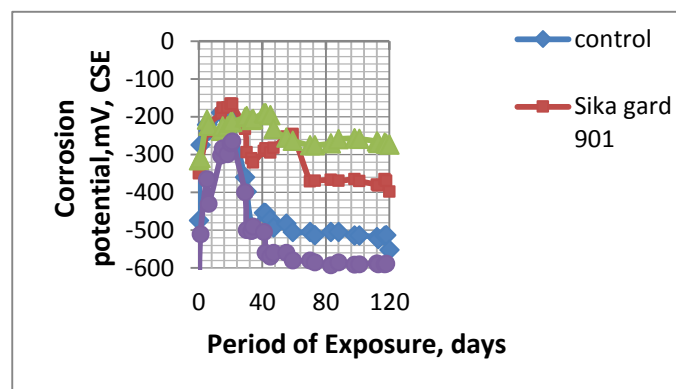


Figure 6: Corrosion potential on steel in the concrete specimens incorporating with 2% inhibitor

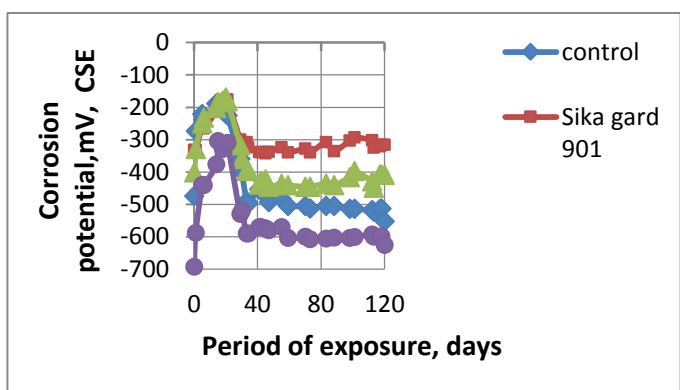


Figure 7: Corrosion potential on steel in the concrete specimens incorporating with 3% inhibitor

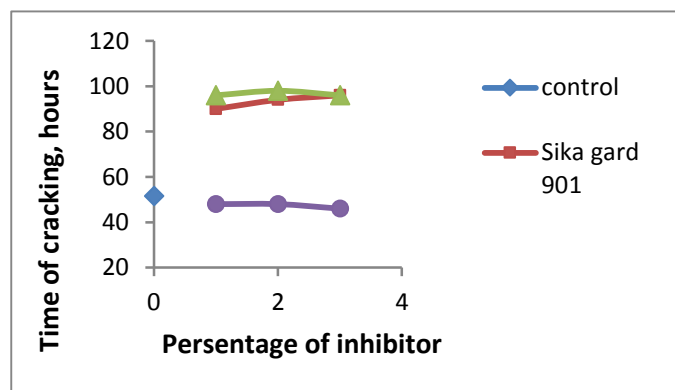


Figure 8: Time of cracking for concrete specimens incorporating inhibitors

4-5: corrosion Current Density by Weight Loss Method

The average corrosion current density calculated in $\mu\text{A}/\text{cm}^2$ for rebar embedded in concrete after 120 days of exposure in the solution with different type and percentage of added inhibitors from 1% to 3% by weight of cement are shown in figure (9).

Figure 9 shows the corrosion current density (I_{corr}) values in the concrete specimens with 1% corrosion inhibitors were in the range of $(0.714\text{--}0.886) \mu\text{A}/\text{cm}^2$ while in the concrete specimens with 2% corrosion inhibitors were in the range of $(0.602\text{--}0.963) \mu\text{A}/\text{cm}^2$. The I_{corr} values in the concrete specimens with 3% corrosion inhibitors were in the range of $(0.696\text{--}0.963) \mu\text{A}/\text{cm}^2$ and $0.911 \mu\text{A}/\text{cm}^2$ for control. The effective corrosion inhibitors were calcium nitrite and Sika ferro gard 901 in the study conditions, the minimum I_{corr} values were noted in the concrete specimens with 2% calcium nitrite inhibitor, followed by those incorporated with 3% Sika gard 901 inhibitor, The decrease in the I_{corr} was 33.9% and 23.6%, respectively, comparing with control specimens.

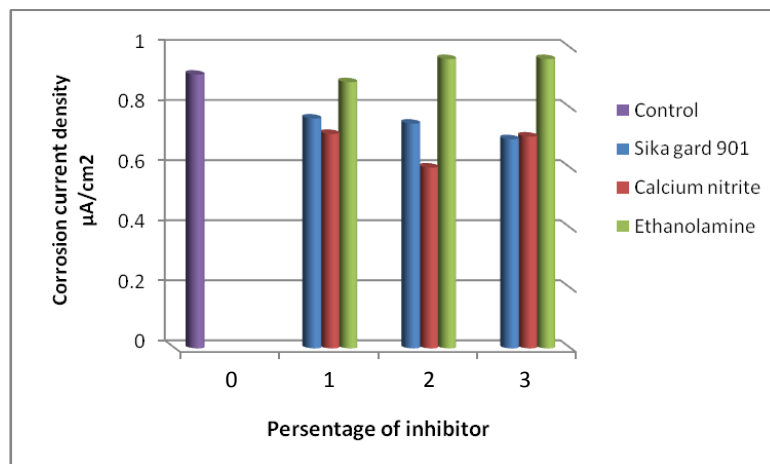


Figure 9: Corrosion current density for concrete specimens incorporating inhibitors

5- Conclusions

1. There is no adverse effect on the compressive and tensile strength of concrete specimens incorporating calcium nitrite and Sika ferro gard 901 corrosion inhibitors. The results showing maximum increasing were about 10% and 5% in the compression and tensile strength respectively, when 2% of calcium nitrite inhibitor was used to compare with the control specimens and there was a slight increase with specimens containing Sika ferro gard 901.
2. Corrosion potential studies revealed that the best performance was shown by 2% of calcium nitrite corrosion inhibitor followed by 3% of Sika ferro gard 901 corrosion inhibitor, the corrosion potentials were -274 and -316 mV CSE, respectively, and they were less negative (more positive) than -350 mV CSE indicating the passivity of reinforcing steel.
3. Ethanolamine corrosion inhibitor ineffective to delay corrosion of the rebar under the conditions of the study and there was an adverse effect on the compressive and tensile strength.
4. Calcium nitrite and Sika ferro gard 901 corrosion inhibitors increased the time to cracking of concrete specimens to about 90% higher comparing with control specimens.

5. The minimum corrosion current density values were obtained from the concrete specimens with 2% calcium nitrite inhibitor, followed by those incorporated with 3% Sika ferro gard 901 inhibitor, the percentage reduction in the values of corrosion current density was 33.4% and 23.6% than that in the control specimens, respectively.

References

1. Saricimen H., 1993,"Concrete durability problems in the Arabian Gulf region", a review. In: Proceedings of 4th International Conference on Deterioration and Repair of Reinforced Concrete in the Arabian Gulf, Manama, Bahrain, p. 943–959.
2. Tuutti K., 1982, "Corrosion of Steel in Concrete", Swedish Cement and Concrete Research Institute, Stockholm, Sweden,.
3. Poulsen E., 1994, "chloride profiles", Analysis and interpretation of observation, AEC laboratory, Denmark, P. 47-62.
4. Page C., Treadaway K., Bamforth P. , 1990, " Corrosion of reinforcement in concrete", London, Elsevier Applied Science, p. 825–850.
5. Nathan C., 1973, " Corrosion inhibitors", National Association of Corrosion Engineers, p. 279.
6. Soylev T.A., Richardson M.G., 2008," Corrosion inhibitors for steel in concrete: State-of-the-art report", Construction and Building Materials 22(4), p. 609–622
7. Craig R.J., Wood L.E., 1970,"Effectiveness of corrosion inhibitors and their influence on the physical properties of portland cement corrosion inhibitor in concrete", Transportation Research Record no 328, p. 77.
8. Treadaway K.W.J., Russell A.D., 1968, "The inhibition of the corrosion of steel in concrete", Highways Public Works 36(19), P.40.
9. Slater J.E., 1983, "Corrosion of metals in association with concrete", ASTM Special Publication No. 818, p.53.
10. Rosenberg A.M., Gaidis J.M., Kossivas T.G., Previte R.W., 1977, "A corrosion inhibitor formulated with calcium nitrite for use in reinforced concrete", ASTM STP629, p. 89–99 .
11. Tomazawa F., Masuda Y., Tanaka H., Fukushi I., Takakura M., Hori T., Higashi S., 1987, "An experimental study on effectiveness of corrosion inhibitor in reinforced concrete under high chloride content conditions", Nihon Architecture Society.

12. Collins W.D., Weyers R.E., Al-Qadi I.L., 1993, " Chemical treatment of corroding steel reinforcement after removal of chloride-contaminated concrete", Corrosion 49(1), P. 74.
13. Prowell B.D., Weyers R.E., Al-Qadi I.L., 1993, "Evaluation of corrosion inhibitors for the rehabilitation of reinforced concrete structures", Research sponsored by Strategic Highway Research Program and carried out at Virginia Polytechnic Institute and State University, Blacksburg, VA, the paper was provided by the manufacturer of MCI2000.
14. Berke N.S., Hicks M.C., 2004, " Predicting long-term durability of steel reinforced concrete with calcium nitrate corrosion inhibitor", Cement and Concrete Composites 26(3), p.191–198.
15. Jamil H.E., Shriri A., Boulif R., Montemor M.F., Ferreira M.G.S., 2005, " Corrosion behavior of reinforcing steel exposed to an aminoalcohol based corrosion inhibitor", Cement and Concrete Composites 27(6), p.671–678.
16. المواصفة القياسية العراقية رقم 5، 1984، "السمنت البورتلاندي"، الجهاز المركزي للتقييس والسيطرة النوعية.
17. المواصفة القياسية العراقية رقم 45، 1984، "ركام المصادر الطبيعية المستعمل في الخرسانة والبناء"، الجهاز المركزي للتقييس والسيطرة النوعية.
18. ASTM Standard A 615/A 615M-06a, "Standard specification for deformed and plain carbon-steel bars for concrete reinforcement", American Society for Testing and Materials.
19. Alhadithy R.Y.M., 2003, " Durability of high performance concrete incorporating high reactivity metakaolin and rice husk ash", MSc thesis, University of Technology, p.47.
20. British Standard BS 1881- part 116, 1983, " Method for determination of compressive strength of concrete cubes", British Standards Institution.
21. ASTM Standard C 496- 96, "Standard test method for splitting tensile strength of cylindrical concrete specimens", American Society for Testing and Materials.
22. ASTM Standard C 876 – 91 (Reapproved 1999), "Standard test method for half-cell potentials of uncoated reinforcing steel in concrete", American Society for Testing and Materials.
23. Al-Mehthel M., Al-Dulaijan S., Al-Idi S.H., Shameem M., Ali M.R., Maslehuddin M., 2009, "Performance of generic and proprietary corrosion inhibitors in chloride-contaminated silica fume cement concrete" Construction and Building Materials 23(5), p.1768–1774

24. Pradhan B., Bhattacharjee B., 2009, "Performance evaluation of rebar in chloride contaminated concrete by corrosion rate", *Construction and Building Materials* 23(6), p.2346-2356.
25. ASTM Standard G1-03, "Standard practice for preparing, cleaning and evaluating corrosion test specimens ", American Society for Testing and Materials.
26. Schutter G.D., Luo L., 2004, "Effect of corrosion inhibiting admixtures on concrete properties", *Construction and Building Materials* 18 (7), p. 483–489.
27. Ann K.Y., Jung H.S., Kim H.S., Kim S.S., Moon H.Y., 2006, "Effect of calcium nitrite-based corrosion inhibitor in preventing corrosion of embedded steel in concrete", *Cement and Concrete Research* 36 (3), p. 530 – 535
28. Al-Amoudi O.S.B., Maslehuddin M., Lashari A.N., Almusallam A.A., 2003, "Effectiveness of corrosion inhibitors in contaminated concrete", *Cement and Concrete Composites* 25 (4-5), p. 439–449.

Effect of silica fume on the mechanical properties of crushed brick concrete

Ghanim Mohammed Kamil

Engineering College / University of Thi-Qar /Iraq

E-mail:ghanimmohammed80@yahoo.com

Abstract:

This paper presents an experimental investigation on the effect of silica fume on the mechanical properties of concrete obtained by replacing 50% of weight of stone aggregate by crushed clay-brick. The only variable considered in this study was the dosage of silica which it is a percent of cement weight, the percent values of replacement silica fume are (0%, 2%, 4%, 6%, and 8%) of cement weight. The comparative study is focus on the effect of the silica fume on this type of concrete not the effect of replacement of crushed brick. The added silica fume has active effect on the strength of crushed brick concrete. The effect of using silica fume on compressive strength is different for the different replacement of silica fume and it is more active for the 2% replacement at 7 days age, while the replacement that yield best enhancement at 28 days is 4%. The compressive strength for 28 days age is about 27.5 MPa, 29.5 MPa, 38.5 MPa, 31.4 MPa, and 10 MPa, for (0%, 2%, 4%, 6%, and 8%) of replacement silica percent. Furthermore the best in increasing in tensile strength is at 2% while there is a small gradually increasing in gain in modulus of rupture with using silica fume until 6%, which beyond the least value it starts to drop. The high level which is observed in this study beyond 6% reduce the gain in strength of compressive at 28 days and it gets a compressive strength less than the control value at 7 days. Furthermore it gets a reduction in tensile strength and modulus of rupture in at 28 days.

Keywords: Crushed brick; Silica fume; Strength.

تأثير مسحوق السيليكا على الخصائص الميكانيكية لخرسانة الطابوق المكسر الخلاصة:

يقدم هذا البحث دراسة حول تأثير مسحوق السيليكا على الخصائص الميكانيكية للخرسانة الناتجة من استبدال 50% من وزن الركام الصخري بوزن مماثل من ركام الطابوق الطيني المكسر. المتغير الوحيد المعتبر في هذه الدراسة هو كمية مسحوق السيليكا المضاف كنسبة من السمنت، كميات الاستبدال للسيليكا هي (0%، 2%، 4%، 6%، 8%) من وزن السمنت. الدراسة مركزة حول تأثير السيليكا على هذا النوع من الخرسانة وليس على نسبة الاستبدال من ركام الطابوق المكسر. الكميات المضافة من مسحوق السيليكا تمتلك تأثيراً على مقاومة خرسانة الطابوق المكسر. التأثير مختلف باختلاف النسب لمسحوق السيليكا وهذا التأثير ذو فعالية أكثر عند 2% استبدال بعمر 7 أيام، بينما نسبة الاستبدال التي حققت أفضل تحسين للمقاومة بعمر 28 يوم كانت 4%. مقاومة الانضغاط للنماذج بعمر 28 يوم هي كالآتي (27.5، 29.5، 38.5، 31.4، 10 MPa)، (0%، 2%، 4%، 6%، و 8%) من استبدال السيليكا في المئة. Furthermore، أفضل زيادة في قوة الشد هي عند 2% بينما هناك زيادة تدريجية في كسب معامل التمزق باستخدام السيليكا حتى 6%، بعد أقل قيمة تبدأ في الانخفاض. المستوى العالي الذي لوحظ في هذا البحث بعد 6% يقلل من كسب قوة الضغط عند 28 أيام ويحصل على قوة ضغط أقل من القيمة التحكمية عند 7 أيام. Furthermore، يحصل على انخفاض في قوة الشد ومعامل التمزق عند 28 أيام.

31.4 ، 10) ميكا باسكال لنسب الاستبدال (0%، 2%، 4%، 6%، 8%) على التوالي، كذلك الزيادة الافضل في مقاومة الشد كانت عند نسبة استبدال 2%، بينما كان هناك ازيا د تدريجي في كسب المقاومة في معامل الانثناء الى حد 6% ، و بعد هذه النسبة تبدأ المقاومة بالتناقص. المستوى العالي لنسبة استبدال مسحوق السيليكا الملاحظ بعد ال 6% استبدال في هذه الدراسة قلل الكسب في المقاومة لمقاومة الانضغاط بعمر 28 يوم واعطى مقاومة انضغاط اقل مقارنة بالنموذج المرجعي بعمر 7 يوم . كذلك قلل ومقاومة الشد ومعامل الانثناء بعمر 28 يوم.

1. Introduction:

Concrete is the most widely used man-made construction material. It is obtained by mixing cement, water and aggregates (and sometimes admixture) in required proportions. Aggregates impart higher volume stability and better durability than hydrated cement paste in concrete and provide around 75 percent of the body of concrete ^[1]. The aggregates are usually derived from natural sources but in regions such as Bangladesh and parts of West Bengal, India where natural rock deposits are scarce, burnt-clay bricks are used as an alternative source of coarse aggregate. Here, construction of rigid pavement, small-to medium-span bridges and culverts and buildings up to six stories high using crushed brick (brick aggregate) concrete is quite common ^[2]. However, the use of mixed aggregate (a combination of brick aggregate and stone aggregate) may improve the strength and stiffness of concrete in comparison with those of purely brick aggregate concrete.

Silica fume is known to improve both the mechanical properties and durability of concrete. The principle physical effect of silica fume in concrete is that of filler besides the pozzolanic activity, which because of its fineness can fit into space between cement grains in the same way that sand fills the space between particles of coarse aggregates and cement grains fill the space between sand grains. As for chemical reaction of silica fume, because of high surface area and high content of amorphous silica in silica fume, this highly active pozzolan reacts more quickly than ordinary pozzolans. The use of silica fume will not significantly change the unit weight of concrete. Silica fume will produce a much less permeable and high strength concrete, but it will not produce a concrete with a higher mass per unit volume. Against these backdrops, this review is focused on the effect of silica fume on mechanical properties of concrete^[3].

Many of researchers focus their searches on the effect of using addition of silica fume on the mechanical properties of concrete and the results somewhat is consistent ,that is in general, the properties are increased with increasing silica fume to limit values and after beyond these limits they start to decrease^[4,5,6]. N. Siva Linga Rao, et. al. investigate the properties of lightweight of aggregate concrete with cinder and silica fume , they conclude that 60 percent

replacement of conventional aggregate with cinder by volume along with cement replaced by 10 percent of silica fume by weight yields the target mean strength. It worth noted that there is a slight increase in strength and other properties due to extended curing periods and the unit weight of the cinder concrete is varying from 1980Kg/m³ to 2000Kg/m³ with different percentages of cinder. It is also noted that there is a decrease in density after extended curing periods^[7].

Due to the excessive of using the natural sources of the aggregate in the infrastructure and in the building in many of the countries, there is a need to find a substitution source for the coarse aggregate, and the demolition of the building construction gets a row material for coarse aggregate.

2. Experimental program:

2.1. Cement:

Ordinary Portland cement (ASTM Type-I) was used as binding material in this study. A mixture of locally available coarse and fine sands were mixed in the ratio of 1:1 (by volume) to be used as fine aggregate. The test values of specific gravity, water absorption, and fineness modulus of fine aggregate indicate that the cement conforms to the Iraqi standard No. 5/1984 ^[8].

2.2. Fine Aggregate (Sand)

Natural sand brought from Al-Zubair region was used as a fine aggregate in this research. The sieve analysis test was conducted according to BS EN 12620+A1^[9].

2.3. Water

Ordinary tap water was used for casting and curing the specimens.

2.4.Coarse aggregate:

The course aggregates used in the study are normal coarse and crushed brick coarse aggregate with maximum size of 10 mm, the sieve analysis for the two type of coarse aggregate are done according to BS EN 12620+A1^[9].

2.5.Crushed brick aggregate:

Crushed stones available in the local market were collected to be used as natural aggregates. Well-burnt bricks of well-shaped and reddish in color were collected and then crushed in the laboratory for making brick aggregates. The nominal dimension of each brick was (241mm×114mm×70mm) and their average compressive strength was found as (23MPa).

The bricks were crushed manually and then sieved into various size fractions, and the flaky particles were separated for rejection. Both types of coarse aggregates were size-screened to a maximum of (10 mm), the sieve analysis is worked according BS EN 12620+A1^[9].

2.6. Silica Fume

The silica fume was in powder form containing 91.4% silicon dioxide (SiO₂) and having a specific surface area of about 18,000 m²/kg was used. The chemical properties of silica fume are given in Table (1). A high range water reducing admixture (superplasticizer) was used in preparing all the specimens in this investigation. Chemically it is Naphthalene formaldehyde sulphonate. It was used in its liquid state as a percentage of cement content (by weight). The dosage of superplasticizer is added to keep the slump in the range 60-80 mm.

Table (1) Chemical properties of silica fume.

SiO ₂	Fe ₂ O ₃	Al ₂ O ₃	CaO	MgO	SO ₃	Loss of ignition
91.4	1.25	1.74	1.28	1.5	0.29	3.8

3. Concrete Mix:

The concrete mix ratio for the study is (cement: sand: coarse) (1:1.5:2) by weight with 50% replacement of crushed brick as coarse aggregate, the water cement ratio is 0.4. The silica fume replacement levels used in this investigation were (2, 4, 6, and 8%) of cement weight. Superplasticizer does is somewhat different to keep the slump in range of 60-80 mm.

4. Experimental procedure:

The work is compose of casting 5 batches of concrete samples, one of them is the control reference and four of them to demonstrate the effect of silica fume on the crushed concrete, each batch includes casting 6 cubes 100 × 100 × 100 mm and cylinder of 150 × 300 mm, and prism of 100 × 100 × 500 mm.

The coarse aggregates and the fine aggregates were made saturated surface dry condition before mixing with other ingredients. At first, the amounts of the mixed aggregates were put in the batch and 0.75 of water were added and then the silica fume were added to the mix and rotate for 2 minutes and then the cement and sand were added and the dosage of the super plasticizer was added to the rest of water, and rotate for 3 minutes. The workability of fresh concrete was measured with standard slump cone test immediately after mixing. The values of slump of fresh concretes for different mixes ranged from 60 mm to 80 mm.

The casting specimens were put on the vibratortable and filled with fresh concrete in three equal layers, and the vibration was done in each layer. The top surface of fresh concrete for both the cylinder and prism specimens was finished off with a trowel. The specimens were demoded after 24 hours of casting. They were cured by immersing in a curing tank in the lab. The specimens were taken out of water at the date and time of testing the sample was removed from water and by cleaning with piece of cloth and testing it for the desired test.

The concrete specimens for different test series were tested (using 130 kN capacity universal testing machine) for compressive strength, splitting tensile strength, and modulus of elasticity at the age of 28 days. Figure 7 shows the test setup of cube and some of the failure cubes. The prisms were tested under single point loading to determine the modulus of rupture. The concrete specimens were tested following appropriate BS EN Standards.

5. Results and discussion:

The results of the tests of the samples which are tested for the work study were plotted as shown from figure 1 to figure 5 to illustrate the function of the mechanical properties.

5.1 .Testing of Specimens

All the tests were done according to the BS EN 12390^[10, 11, 12, and 13] Testing hardened concrete Part 6: Tensile splitting strength of test specimens. The cube specimens, the cylinder and the prisms were subjected to water curing. The cubes were tested at 7 days and 28 days to determine the compressive strength. The other samples were tested to determine the tensile strength and the rupture of failure at 28 days.

5.2. Compressive strength:

Figs. 1 and 4 show the variation of compressive strength with the concrete mixes having different SF contents. At 7 days age, an increase in all levels of replacement is observed while the reference mix exhibit higher strengths than the corresponding mixes containing silica fume beyond 6%. At 28 days, there is an increasing in compressive strength and gain higher the reference mixes. Concrete mixes incorporating 2 to 6 % silica fume will continue to gain higher strengths as compared to reference mixes. The variation in compressive strengths of Silica fume concretes expressed as a percentage of the corresponding strength of reference mix has been given in fig. 4. As compared to the reference mix, the replacement of silica fume at range 2% to 4% gives somewhat a steady constant gain in strength and it is the maximum

gain. After 4% there is a decreasing in gain of strength and it is a more reduction in concrete at 7 days than 28 days, may be this occurs due to the required enough curing to get the silica more effective as stated by other researches^[7]. Also may be the lower improvement in strength in could be attributed to inherently lower capillary porosity in the reference mix as a result of lower water/binder ratio. Inherent lower capillary porosity leaves less room for improvement by incorporating SF.

The results show that up to the 6% is there are gains in strength in compressive strength for both 7 days and 28 days to the reference mixes. This indicates that the pozzolanic effect of silica fume is become slower in high percent. However, beyond 7 days, silica fume mixes gain higher strengths due to the reaction mechanism of silica fume. It is observed that silica fume mixes show highest strengths at 28days, indicating that the pozzolanic reaction dominates from 7 to 28 days^[14]. It is also observed that silica fumecontent of 4% gives maximum improvement in compressive strength values. This could be attributed to the lime content. In concrete mixes having silica fume contents lower than 4%, silica fume does not consume all of CH and thus improvement in strength is not high^[5,15]. The figures of 1 and 4 show the affecting of the replacement of silica fume on the compressive strength of cubes. From the figure it can be conclude that there is a rational effect of adding silica fume, the behavior of samples at 7 days are similar of the 28 days in strength of compressive of cubes. The 2% replacement of silica fume is the more active in increasing of strength at 7 days, while the 4% is the more active at 28 days.

5.3. Tensile strength:

Fig. 3 and Fig. 6 show the variation of split tensile strength with silica fume replacement percentage. It is observed that silica fume incorporation increases the split tensile strength of concrete until 2% replacement of silica fume. A close observation of Fig. 2 exhibits that beyond 2% of replacement start the tensile with dropping with increasing in replacement ratio of silica fume and does not significantly increase the split tensile strengths and the maximum increase at 2% is 48%. Replacements considerably improve the split tensile strength with respect to control. The initial filling of the voids by silica fume significantly improves the tensile strengths, but at higher levels, the improvements decrease. On computing the percentage gains in split tensile strengths of silica fume concrete with respect to control, the best values of the average gains are at 2% and 4%, replacement levels are obtained as 48% and 20 respectively. The trend in strength gain is almost similar with that of compressive

strength at 7 days and 28 days, the optimum 28-day split tensile strength at 2% of replacement level of silica fume.

5.4. Modulus of Rupture:

Fig. 2 and Fig. 5 shows the variation of flexural tensile strength with silica fume replacement percentage. Fig. 2 does reflect a rational consistent view with the tensile and compressive strength, it shows that there is a gradually increasing in the strength of modulus of rupture with replacement of silica fume until 6%, it may be similar in general behavior with compressive strength and somewhat with tensile strength but in a less limit. The using of higher than 6% of silica fume seems to have the same pronounced effect on the split tensile strength and compressive strength, leads to dropping in strength as in Fig. 5. The gains in split tensile strengths are higher than the flexural strengths at lower replacement levels. The flexural strengths almost follow the same trend as the 28-day compressive strength does. The results of the present investigation indicate that the optimum silica fume replacement percentage for 28-day flexural tensile strength is at 6%.

6. Conclusions:

This study is worked to establish the effect of the silica fume on the mechanical properties of the concrete with crushed brick at 50% replacement. The percentage of silica fume is the main factor in this study which is mentioned to establish the enhancement in the compressive strength, tensile strength, and the rupture strength of concrete. From the diagrams which are executed based on the values, it can be concluded the following:

1. There is a somewhat similar behavior of the increasing in the compressive strength, tensile strength, and rupture failure strength.
2. The increasing is somewhat larger for the compressive in 6 %.
3. The increasing percent is linear with increasing of the silica fume for a limit and it is similar in general with the previous studies^[4, 5, 6, and 7].
4. The best percent of silica fume adding for compressive is at 4% at 28 days while is at 2% for both compressive at 7 days and tensile strength at 28 days while for modulus of rupture is at 6%.
5. There is a need to further study in method of adding of the silica fume and for more replacement levels of silica fume.

6. Using of high percent of silica fume does not significantly increase the split tensile strengths, and the 2% of replacement gives best increasing ratio, 48%.

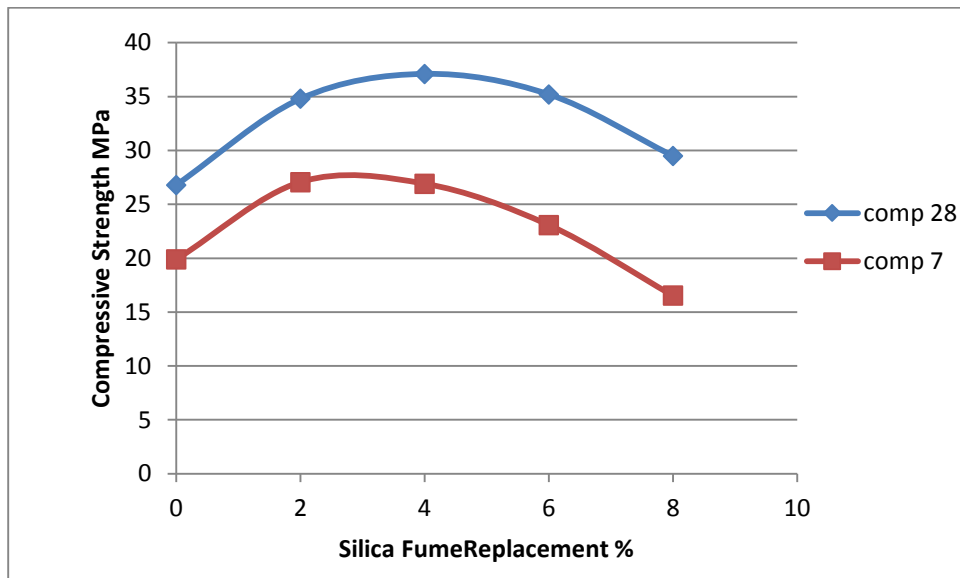


Figure1: Relationship between 28 days and 7 days compressive strength and percent of silica fume replacement

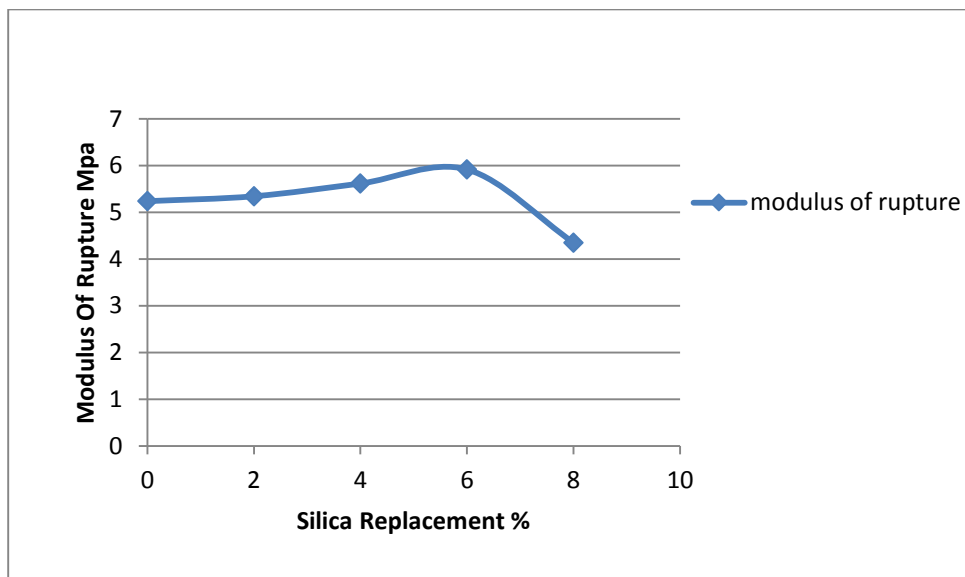


Figure 2: Relationship between 28 days modulus of rupture and percent of silica fume replacement

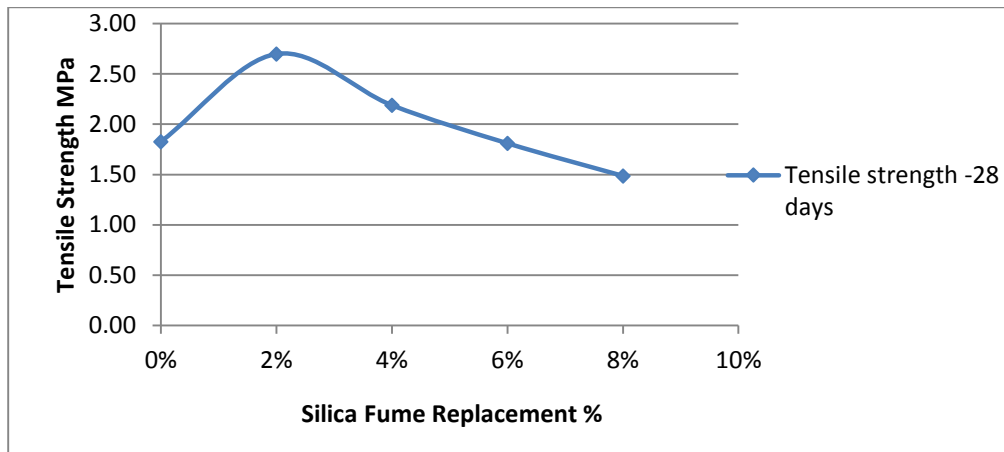


Figure 3: Relationship between 28 days tensile strength and percent of silica fume replacement

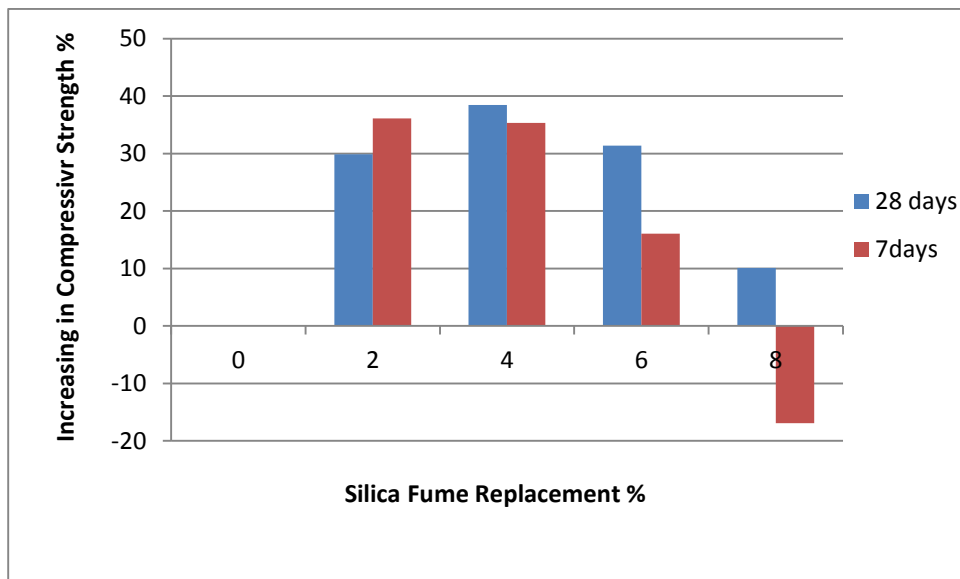


Figure 4: Bar chart shows variation in increasing of compressive strength of concrete at 7 days and 28 days with different percent of replacement of silica fume.

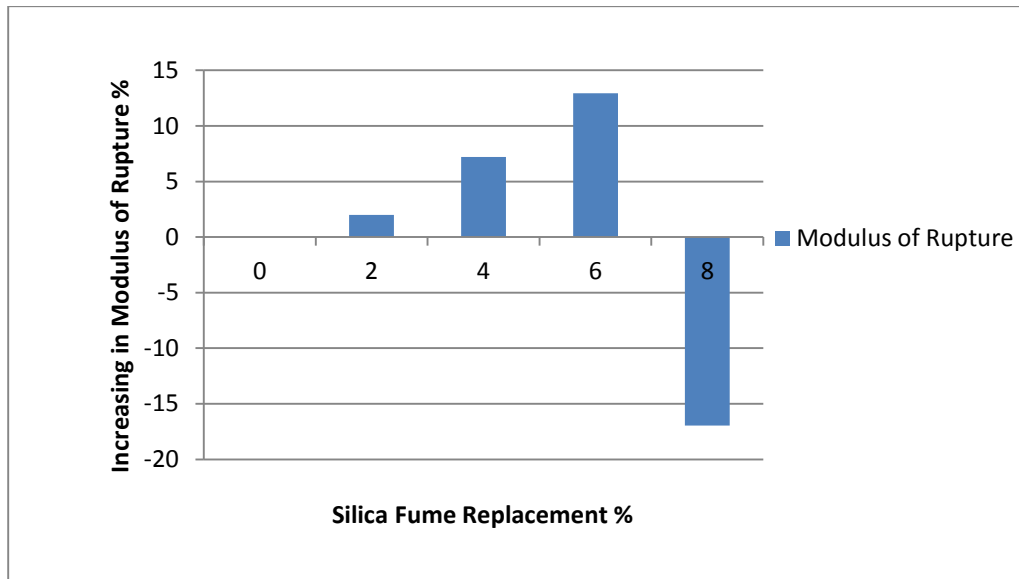


Figure 5: Bar chart shows variation in increasing of Modulus of Rupture of concrete 28 days with different percent of replacement of silica fume.

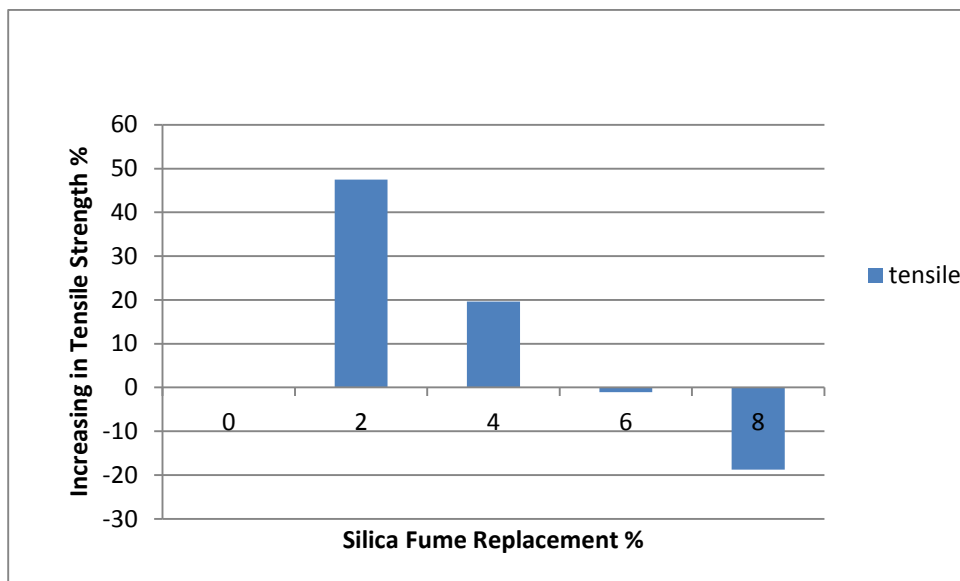


Figure 6: Bar chart shows variation in increasing of Tensile Strength of concrete 28 days with different percent of replacement of silica fume.



Figure (7) shows cubes under test and failure samples

References:

- [1] M. L. Gambhir, Concrete Technology, Tata McGraw-Hill Publishing Company Limited, New Delhi, India, 1993.
- [2] M. A. Mansur, T. H. Wee, and L. S. Cheran, "Crushed bricks as coarse aggregate for concrete", ACI Materials Journal, Vol.96, No.4, pp.478-484, 1999.
- [3] Abdulhanan A. Darwish "Development of high performance concrete using combinations of mineral admixtures", PhD thesis, 1995.
- [4] H. Katkhuda, et.al." Influence of silica fume on high strength lightweight concrete", World Academy of Science, Engineering and Technology 34 2009
- [5] N. K. Amudhavalli¹, Jeena Mathew, "Effect of silica fume on strength and durability parameters of concrete", International journal of Engineering Sciences & Emerging Technologies, August 2012, ISSN: 2231 – 6604 Volume 3, Issue 1, pp: 28-35 ©IJESET.
- [6] Juan Lizarazo-Marriga and Lucio Guillermo LÓPEZ YÉPEZ, "Effect Of Silica Fume Addition On The Chloride-Related transport properties Of High-Performance Concrete", Dyna, year 79, Nro. 171, pp. 105-110. Medellin, february, 2012. ISSN 0012-7353.
- [7] N. Siva Linga Rao, et. al. "Properties of Light Weight Aggregate Concrete with Cinder and Silica fume Admixture", International Journal of Earth Sciences and Engineering ISSN 0974-5904, Volume 04, No 06 SPL, October 2011, pp 907-912
- [8]. (I.O.S. 5 / المواصفة العراقية رقم (5) لسنة 1984) للإسمنت البورتلاندي (1984)
- [10] British standard institution BS EN 12620:2002 +A 1. Aggregates for concrete, Incorporating corrigendum. BSI, 2008.
- [9] BS EN 206-1, Concrete –Complementary British Standard to BS EN 206-1 – Part 1: Method of specifying and guidance for the specified, Second (present) edition, November 2006.
- [11] Testing hardened concrete Part 6: Tensile splitting strength of test specimens, BS EN 12390-6:2000.
- [12] Testing hardened concrete Part 5: Flexural strength of test specimens, BS EN 12390-5:2000.
- [13] Testing hardened concrete Part 4: Compressive strength specification for testing machines, BS EN 12390-4:2000.

[14] Des King , "The effect of silica fume on the properties of concrete as defined in concrete society report 74, cementitious materials" 37th conference concrete 37th Conference on Our World in Concrete & Structures 29-31 August 2012, Singapore.

[15] V.Bhikshma, K.Nitturkar and Y.Venkatesham, "Investigations on mechanical properties of high strength silica fume concrete." Asian journal of civil engineering (building and housing) vol. 10, no. 3 (2009) pp.335-346.

Analysis of Cyclostationary CR Detector for OFDM signals

Hussian K. Chaiel

University of Thi-Qar /College of Engineering

Abstract:-

The cyclostationary based spectrum sensing algorithm is especially suitable for detection of orthogonal frequency division multiplexing (OFDM) signals that exhibit strong periodic correlation due to insertion of cyclic prefix between OFDM blocks. Normally, the cyclic prefix is used to remove the Intersymbol interference (ISI) and intercarrier interference (ICI) of the OFDM signal and so it eliminates a need for complex equalizer.

In this paper, simulation results demonstrate the normalized spectrum correlation function of the primary OFDM signal used in cognitive radio systems with different values of cyclic frequency. Two techniques are assumed to be used as PAPR reduction of OFDM transmitted signal. The results show that only one of them has no apparent effect on the correlation performance of the cyclostationary detector. Finally, it is found that a reduction of 30% in the implementation complexity can be taken by suitable choice of detector cyclic frequency.

Keywords:- OFDM, Cognitive Radio, Cyclostationary Detection, Dynamic Spectrum Sensing.

الخلاصة:-

تعتبر خوارزمية تحسس نطاق الترددات بالاعتماد على تقنية (cyclostationary) الأكثر ملائمة لكشف إشارات (OFDM) والتي تؤمن خاصية ارتباط متكرر عالية بسبب إدخال بادئة دورية بين رموزها. عادة، البادئة الدورية تستعمل للتخلص من التداخل البيئي للرموز و الترددات الحاملة والذي يعني عدم الحاجة لاستخدام المصحح المعقد. في هذا البحث، نتائج محاكاة بالحاسبة لدالة ارتباط النطاق الترددي لإشارة (OFDM) للمنظومة الراديوية الإدراكية. تم افتراض تقنيتين لتقليل (PAPR) لتلك الإشارة. أثبتت النتائج أن أحد تلك التقنيات داعمة لخواص الارتباط لهذا الكاشف. أخيراً، تم الحصول من خلال البحث على تقليل مانسبته (30%) من تعقيد بناء الكاشف عملياً عن طريق الاختيار المناسب للتردد الدوري للكاشف المعتمد في هذا البحث.

I. Introduction:

The policy of spectrum licensing and its utilization lead to static and inefficient usage of this spectrum and so it has become essential to introduce new licensing policies to enable dynamic and open way of utilizing the available spectrum efficiently. Recent studies on radio

spectrum usage have given birth two concepts: Dynamic Spectrum Access (DSA) and Cognitive Radio (CR) [1]. One of the most suitable techniques to guarantee a dynamic spectral occupancy of the transmitted signal (licensed signal) is the Orthogonal Frequency Division Multiplexing (OFDM) technique . On the other hand, Cognitive radio allows unlicensed users (secondary users) to access licensed frequency bands to reduce spectrum scarcity. Even after the beginning of the transmission, the bands must be continuously checked for any primary user entering to transmit in these bands. If so the secondary users should vacate the bands as quickly as possible and go on to some other empty frequency spectrum [1,2].

A number of schemes have been developed for detecting the presence of primary user in a certain frequency band. Energy detector and matched filter type are examples of such schemes. The first functions properly for high signal to noise ratio while the second complexity is very high. These constraints led to implement a detector which performed well under low signal to noise ratio and with complexity not as high as the matched filter detector. Such type is called cyclostationary detector. This detector is merely a Fourier transform of the correlated received signal and results in peaks at frequencies which are specific to the signal. The searching for these peaks helps in determining the presence of primary user [3, 4].

The rest of the paper is organized as follows; section II describes briefly the mathematical analysis of the cyclostationary detection for OFDM signal and discusses the challenges oppose the implementation of such detector. Section III presents computer simulation tests to show the correlation performance in the presence of techniques used to reduce the peak to average power ratio (PAPR) of the OFDM signal. This section includes also the hardware complexity to implement this detector. Finally, the paper is concluded in section IV.

II. Cyclostationary Detection of OFDM Signal

A. Mathematical Analysis

The mathematical development for cyclostationary analysis is based on Gardner's work [5] and it may be derived as:-

A complex random process $x(t)$ is said to be cyclostationary in wide-sense, if its mean ($E\{x\}$) and autocorrelation (R_x) in time domain are periodic:-

$$\begin{aligned} E\{X(t+T)\} &= E\{X(t)\} \\ R_X(t+T, \tau) &= R_X(t, \tau) \end{aligned} \quad (1)$$

where $R_X(t, \tau) = E\{x(t+T)x(t)\}$

Due to periodicity of autocorrelation, it can be expanded using Fourier series as:-

$$R_x(t + T, \tau) = \sum_n R_x^{\frac{n}{T}}(\tau) e^{j2\pi\frac{n}{T}t} \quad (2)$$

where $\frac{n}{T}$ represents the cyclic frequency and can be written as α . The coefficients ($R_x^{\alpha}(\tau)$) represent a function, which may be called the Cyclic Autocorrelation Function (CAF), which may be represented by;

$$R_x^{\alpha}(\tau) = \lim_{T \rightarrow \infty} \int_{-T/2}^{T/2} R_x(t + T, \tau) e^{-j2\pi\alpha t} dt \quad (3)$$

The cyclic Wiener relation states that the Spectrum Correlation Function (SCF) is then calculated using the Fourier transform of the cyclic autocorrelation function and its maximum value is directly proportional to the probability of detection and inversely proportional to the probability of false alarm [6]:-

$$S(f, \alpha) = \int_{\tau=-\infty}^{\infty} R_x^{\alpha}(\tau) e^{-2\pi f\tau} d\tau \quad (4)$$

In this work, the primary signal ($x(t)$) is an OFDM signal, which may be represented as a composite N statistically independent QAM signal [7];

$$x(t) = \sum_k \sum_{n=0}^{N-1} \mathfrak{x}_n e^{j\left(\frac{2\pi}{T_s}nt\right)} q(t - kT) \quad (5)$$

Where \mathfrak{x}_{nk} is a complex sequence corresponds to a rectangular QAM signal point space, $q(t)$ represents a rectangular shaping pulse of duration T and T_s is a source symbol length.

The detection process based on the spectrum correlation function (Eq.4) may be implemented in three steps using the block diagram shown in (Fig.1) [6]:-

- The signal of interest is shifted by $\frac{\alpha}{2}$ and $\frac{-\alpha}{2}$.
- The shifted signals are multiplied after passing through sliding windows, where the symbol ($*$) represents the complex conjugate.
- Spectrum Correlation Function (SCF) is found by taking the Fourier transform of the multiplied signals .

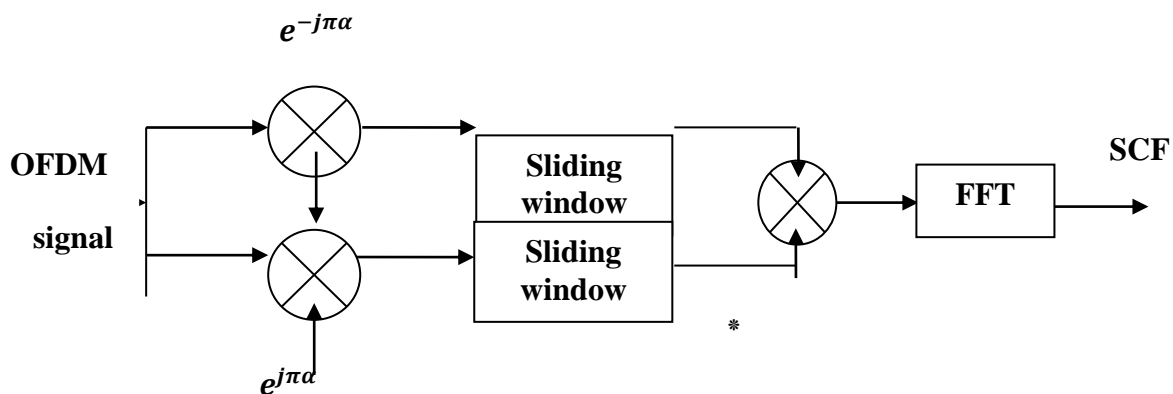


Fig.1 Block diagram of cyclostationary detector

B. Detection Challenges

However, there are two main challenges for using the cyclostationary detector in the OFDM systems. These challenges are [8-10]:-

- The first challenge is appeared due to the property of the IFFT used at the transmitter of the OFDM system, which is a high peak to average power ratio (PAPR) of the transmitted signal. This causing subcarrier intermodulation and undesired out- off band radiation. Such two drawbacks lead to inefficient amplification and a need to an expensive power amplifier. So it is important to use techniques to reduce the PAPR. These techniques may in turn reduce the correlation characteristics of the detector. [11] suggests a simple technique to reduce this ratio by mapping the QPSK symbols at the input of the IFFT of the transmitter with a certain formula. The results included in [11] show that the bit error rate performance is better than that of the conventional clipping PAPR technique. [12] proposed a tone reservation technique (operates with large number of subcarriers) reduces the ratio by a factor of nearly 5 dB. However the complexity is the main drawback of the technique proposed in [12], especially if large number of iterations are needed.
- The second challenge is merely the implementation complexity (number of arithmetic operations) of the cyclostationary detector. Many literatures analyze such issue, for example, problems of cycle leakage, aliasing and cycle phasing had been disused in [5]. In literature [13], the implementation is done mostly in angular domain to avoid complex operation (multiplication and addition/ subtraction). Finally, the signal is mapped back to Cartesian coordinates.

III. Computer Simulation tests

A. Detector performance

To examine the performance of the cyclostationary detector (Fig,1), computer simulation tests have been carried out using Matlab software. In these tests, the signal to noise ratio is equal to -20 dB and $N = 32$. A sliding window of 32-width Hamming window is used, Firstly, the maximum normalized SCF of the envelop OFDM signal is plotted with different values of cyclic frequency (α). Such plot is shown in Fig.2.

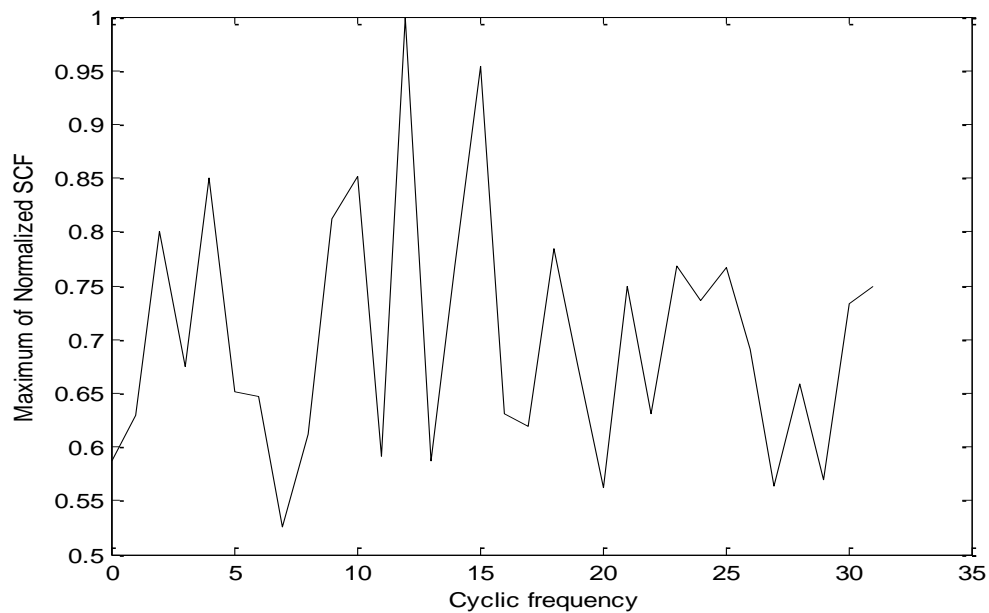


Fig.2 The maximum of SCF for different values of cyclic frequency

For $N = 32$, Fig.2 shows that the normalized spectrum correlation function has its maximum value at cyclic frequency of 12 ($\alpha = (\frac{12}{32}T)$). According to this value, Fig.3 shows the ability for such detector to know the existence of primary OFDM signal with high probability of detection and low probability of false alarm (due to clear maximum value of SCF in this figure).

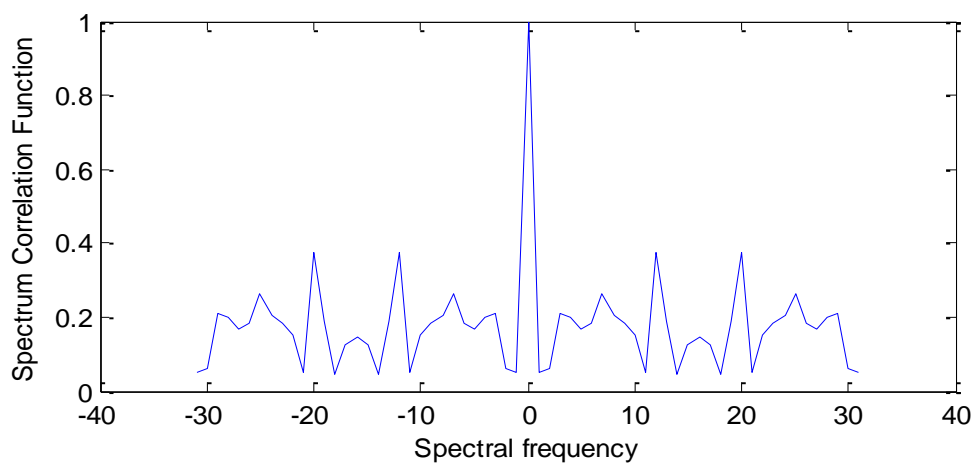
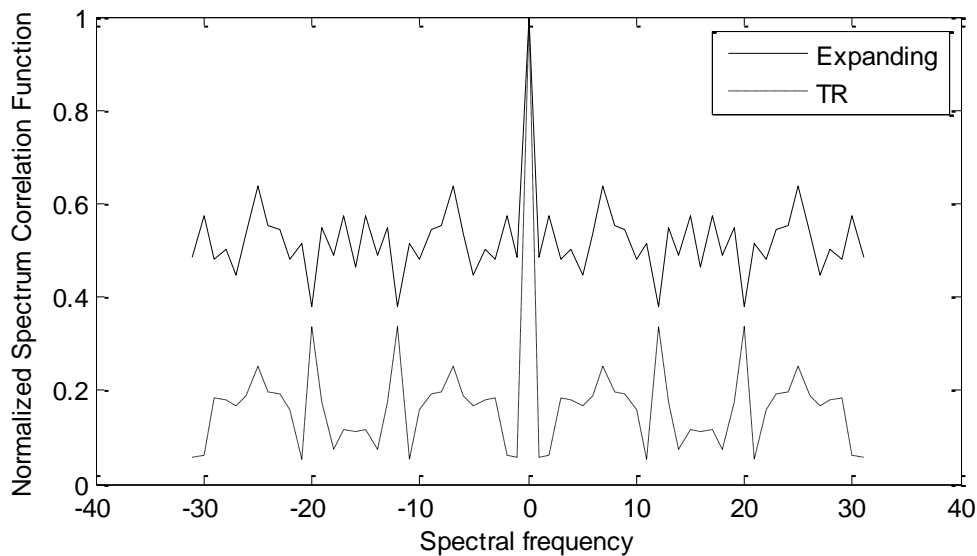


Fig.3 The normalized SCF of cyclostationary detector for OFDM signal

Extra tests shows that the correlation characteristics of the cyclostationary detector may affected when PAPR reduction techniques are used at the transmitter side of the OFDM system (first challenge in section II-B) . In these tests, symbol expanding technique [11] and tone reservation algorithm [12] are used. For an OFDM system with first technique, a reduction in the spectral correlation magnitude for the envelop of the OFDM signal is shown in Fig.4. This reduction makes the detection more difficult. In the other hand, the use of parallel search tone reservation method with memorized values enhances the cyclostationary features. It is clearly appears in Fig.4 that the difference between the maximum and the other values of the spectrum correlation function (SCF) in the tone reservation technique is higher than that of the symbol expanding technique. This means that an OFDM signal with tone reservation technique has better probability of detection and probability of false alarm than that of a same signal with symbol expanding technique.



Further tests are used to estimate the complexity of the cyclostationary detector (Fig.1). The complexity is calculated in terms of the number of addition/subtraction and multiplication operations of the detector algorithm. Table.1 shows the result of these tests with different values of OFDM symbols.

Table.1 The complexity of the cyclostationary detector for different values of OFDM symbols			
	OFDM blocks	addition/subtraction	multiplication
1	16	96	204
2	32	192	396
3	64	384	780
4	128	768	1548
5	265	1536	3084
6	512	3072	6156

C. Proposed detector

As expected, Table.1 shows that the complexity of traditional cyclostationary detector is proportional with the number of OFDM symbols. To reduce the detector complexity, this paper suggests an algorithm to implement the cyclostationary detector. This algorithm is mainly based on the reduction of the number of the multiplication and addition / subtraction operations by choosing two suitable values of cyclic frequencies (α_1 and α_2). These values are used with the exponent function in the upper and the lower arms of the detector shown in Fig.1. As a result, the real or the imaginary parts of the exponent function is equal to zero or constant, so there is no need to more mathematical operations to implement such function. This idea behind this algorithm may be explained by the following two steps:-

- Step 1: for a certain value of N , the cyclic frequency (α) is chosen such that the SCF is maximum.
- Step 2: the values of α_1 and α_2 are calculated such that the sum of these values is equal to α and the real and imaginary parts of $(e^{j2\pi\alpha_1})$ and $(e^{j2\pi\alpha_2})$ are equal to zero or constant value.

Therefore, the complexity of the proposed detector is then calculated in terms of the number of mathematical operations for different values of OFDM symbols as tabulated in Table.2:-

Table.2 The complexity of the proposed detector for different values of OFDM symbols			
	OFDM blocks	addition/subtraction	multiplication
1	16	80	134
2	32	160	262
3	64	320	518
4	128	640	1030
5	265	1280	2054
6	512	2560	4102

Finally, the estimated behavior of the traditional and the proposed detectors under multipath propagation is shown in Fig.5. Such behavior is represented by the probability of missed detection for different values of received signal to noise ratio. In this test, the received multipath signal is assumed to be a sum of the received signal with its delayed and attenuated version. The values of attenuation factor and normalized delay are assumed to have 0.75 and 15 respectively. The figure shows that the behavior of the traditional detector is better than that of the proposed detector (nearly 0.5 dB difference at probability of 10^{-4}) as a result of unbalanced values of cyclic frequencies used in the proposed detector.

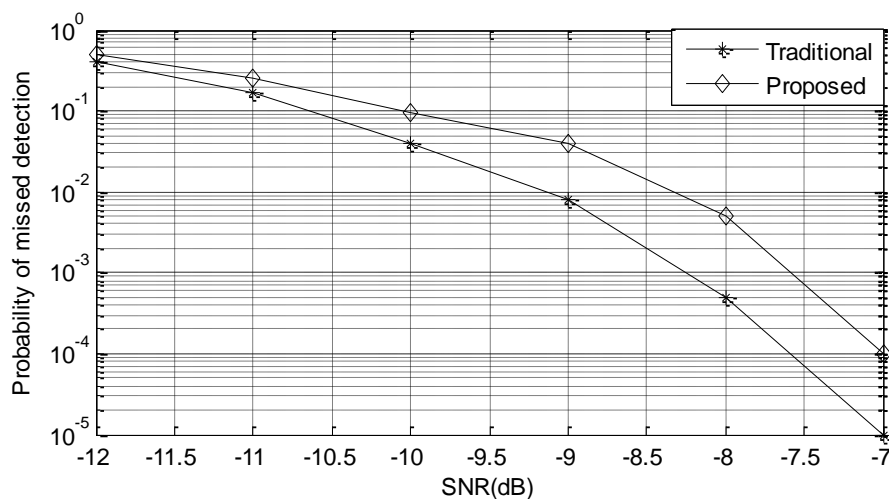


Fig.5 The behavior of the two detectors under multipath propagation conditions.

IV. Conclusion

Based on the correlation characteristics of the cyclostationary detection, this paper proves its ability to detect the OFDM primary signal. The results show the simplicity in the detection when a proposed tone reservation technique is used for reduction the PAPR of the OFDM signal. This work proposes also a method to reduce the complexity of cyclostationary detector in terms of number of arithmetic operations needed for hardware implementation. Further tests show that such hardware complexity reduction has an effect on the behavior of the proposed detector.

References

- [1] Laser Berleman and Stefan Mangold, "Cognitive Radio and Dynamic Spectrum", John Wiley and Sons, 2009.
- [2] Yulong Zou, Yu-Dong Yao and Baoyu Zhang, "Cognitive Transmission with Multiple Relays in Cognitive Networks", IEEE Transaction on Wireless Communication, vol.10, no.2, pp.648-659, February 2011.
- [3] Harry Urkowitz, "Energy Detection of Unknown Deterministic Signals", Proceeding of IEEE, vol.55, no.4, April, 1967.
- [4] S. Haykin, "Cognitive Radio: Brain Empwered Wireless Communications", IEEE Journal on Selected Areas on Communications", vol.23, no.2, pp.201-210, 2005.
- [5] William Gardner, "Measurement of Spectral Correlation", IEEE Trans. On Acoustics, Speech and Signal Processing, vol.34, no.5, pp.1111-1123, 1986.
- [6] Manish Dave, "Spectrum Sensing in Cognitive Radio: Cyclostationary Detector", M.Sc Thesis, National Institute of Technology, Rourkela, India, 2012.
- [7] Kyou Woong Kim, "Exploiting Cyclostationary for Radio Environmental Awareness in Cognitive Radios", Ph.D Thesis, Faculty of Virginia Polytechnic Institute, Virginia, USA, 2008.
- [8] Vladimir Sebeta, Roman Marsalek and Zbynek Fedra, "OFDM Detector Based on Cyclic Autocorrelation Function and its Properties", Radioengineering, vol.20, no.4, pp,926-931, December 2011.
- [9] Sina Maleki, Ashish Pandharipande and Geert Leus, "Two-Stage Spectrum Sensing for Cognitive Radio", IEEE International Conference on Acoustics, Speech and Signal Processing, pp. 2946-2949, March 2010.

- [10] Paul D. Sutton, Keith E. Nolan and Linda E. Doyle, "Cyclostationary Signature in Practical Cognitive Radio Application", IEEE Journal on Selected Areas in Communication, vol.26, no.1, pp.13-24, 2008.
- [11] Hussain K. Chaiel, "Sample Expanding Technique for PAR Reduction in OFDM Systems", Journal of Thi-Qar University, vol.5, no.3, 2009.
- [12] Hussain K. Chaiel, Hassan A. Nasir, "Proposed Algorithm of Tone Reservation PAPR Reduction in OFDM System", Basrah Journal for Engineering Sciences, vol.10, no.1, 2010.
- [13] V. Turunen, M. Kosunen, A. Huttunen, S. Kallioinen, P. Ikonen, A. Parssinen and J. Rynanen, " Implementation of cyclostationary feature detector for cognitive radio", In Proceedings of the 4th international conference on GROWNCOM '09, Hannover, Germany, pp.1-4, 2009.

Study Large Deformation Coil Spring Development For Robotics Submersible

Dr. Intessar A. Hadi

Lecturer

University of Technology

Machines & Equipment Engineering Department

Baghdad Iraq May 2012

Abstract

In this work the present a theoretical study for the free vibration of cylindrical, conical and helical springs. Circular cross sections, and non-circular cross section, namely elliptical, are considered as well for the investigating of the frequency characteristics of the springs. The equations of motion are derived mathematically for springs with different geometries. The mode shapes are numerically implemented by using COMSOL 4.2 software package for three dimensional solid elements. The mode shapes configurations are determined by applying different force loads and boundary conditions for different number of spring turns. The results show that increasing the number of turns leads to decrease the spring stiffness and vice versa. Also decreasing turn number is a good strategy to distinguish between different mode shapes. Springs stiffness is directly proportional to coil diameter. It is also shown that the configuration of cylindrical- elliptical spring is prone to the applied force where the stiffness is lower among all other spring types with the same number of turns.

دراسة التشوهات الحاصلة في النوابض الحلزونية للغاطس الآلي

الخلاصة

يقدم هذا العمل دراسة نظرية للاهتزازات الحرة لأنواع من النوابض كالحلزونية والاسطوانية والمستطيلة متساوية ومختلفة المقطع كالمخروطية. تم اشتقاق المعادلات الرياضية للنوابض ذات المقطع المتساوي رياضياً أما الدوال الشكلية للنوابض تم حسابها عن طريق برنامج متطور يسمى كومسول (4.2) لعنصر ثلاثي الأبعاد ووضع قوى مختلفة تراوحت بين 50 إلى 150 نيوتن وتثبيت طرف من النابض وظهرت النتائج أن زيادة عدد حلقات النوابض يؤدي إلى قلة جساءة النابض والعكس بالعكس. كما أنها طريقة جيدة للتفريق بين الدوال الشكلية كما أن هناك علاقة بين كل من جساءة النابض وقطر الملف ويعتبر النابض الاسطواني أفضل من النوابض الأخرى عن تسليط الاحمال بجساءة أقل ولنفس عدد الحلقات .

KEY WORDS

Helical springs; non-cylindrical; free vibration

Notations

E, \bar{G}, ν	= Young's modulus N/m^2 ,shear modulus N/m^2 , Poisson's ratio
ρ	= mass per unit volume of wire $/kg/m^3$
t	= time / s
t, n, b	= tangential, normal and binormal unit vector
χ, τ, h	= curvature ,tortuosity and step for unit angle of the helix
M_t, M_n, M_b	= torsional moment and bending moments, respectively
T_t, T_n, T_b	= axial force and shear forces , respectively
U_t, U_n, U_b	= Frenet components of displacement vector
$\Omega_t, \Omega_n, \Omega_b$	= Frenet components of rotational vector
J or I_t	= torsional moment of inertia
A	= cross sectional area
d, D	= diameters of the circular cross- section and helix ($R=D/2$)
I_n, I_b	= moment of inertias of cross –section with respect to n, b axes
C_t, C_n, C_b	= the axial stiffness and the shearing stiffness's ,respectively
D_t, D_n, D_b	= the tensional stiffness and the flexural stiffness's respectively
p, m	= external force and moment vector per unit length
S	= state vector

1. Introduction

Helical springs are commonly used in many engineering applications serving important mechanical tasks. The problem of helical springs is a classic mechanical problem that is subjected to many theoretical studies for decades. Performances of compressive springs working within dynamic environments in mechanisms have become particularly important in recent years . Helical springs are amongst the most familiar engineering components and , as vital part of the automotive engine, they have been the subject of close scientific scrutiny . Cylindrical and non –cylindrical helical springs are common in many applications for wide variety of reasons, Figure (1) demonstrate the robotic fish design [7]. The number of paper present on the non–cylindrical coil springs is, yet, insufficient [3],[4],[5].The problem is described by six differential equations .These are second order equation with variable coefficients , with six unknown displacements. Three translations , and three rotations at every point along the member. A number of investigations were conducted in the field of vibration behavior of helical springs with constant cross section [6]. However, there is no paper published on the vibration analysis of the helical springs with variable cross section.

Although, there are some studies of the problems of free vibration of cylindrical coil spring [4], there have been only a few studies on the free vibration of helical springs with irregular shapes. Yildirim[5] investigated the free vibration frequencies of cylindrical springs by the transfer matrix method. Nagaya et al. [1] have determined the free vibration frequencies of non-cylindrical helical springs both experimentally and by the method of Myklestad. For this purpose, they have used the static element transfer matrix, where they derived the closed form solution with taking into account only the axial deformation for circular cross sections. Yildirim [1] used both the Myklestad method and the complementary functions methods, and presented the free vibration of non-cylindrical helical springs taking into account the effects of axial and shear deformation together with the rotary inertia. The free vibration problem of helical spring by the transfer matrix method. Yildirim employed the transfer matrix and the complementary functions to compute the eigenvalues on non-cylindrical helical springs. The applications that use the helical and other types of springs are in continuous developments starting from the micro scale applications to huge civil engineering structures. The frequency characteristics of the helical springs can be implemented as a substitution for some continuous system applications. For instance, the robotics fish, is the interest of many researchers and companies around the globe. Due to highly need of such application, many models for robotics fish have been suggested in the last ten years. Some of these models are based on purely mechanical design, and some are based on using of smart materials. In general, the thrust mechanism stills the main challenge in the size and design of submersibles. Recently, it has been shown that the fluid-conveying pipes are a powerful technique for the thrust of submersibles. The mode of fluttering depends on the pressure inside the pipe, and it is found that higher pressure leads to fluttering with higher modes.

In this study we extend the work presented by Aren [7] who designed a robotics fish that works on the fluid inducing mechanism for the thrust force, he used relatively long hollow tail made of latex, see figure (1). The tail conveys water that is pumped from the head of the fish and flows through the latex tail and induces the tail to flutter and result in thrust force moves the fish forward. We investigate replacing of the long latex tail by a short helical spring that does the same function. the objective of the work is to replace the long latex tail by short coiled spring, than studying the eigenfrequencies of the coiled spring under the effect of internal flow along the main axis, we investigate the effect of the internal pressure on the mode shapes for different types of coiled springs. Using of suitable type of coiled spring as a substitution for the latex tail of the submersible

Stream Flow

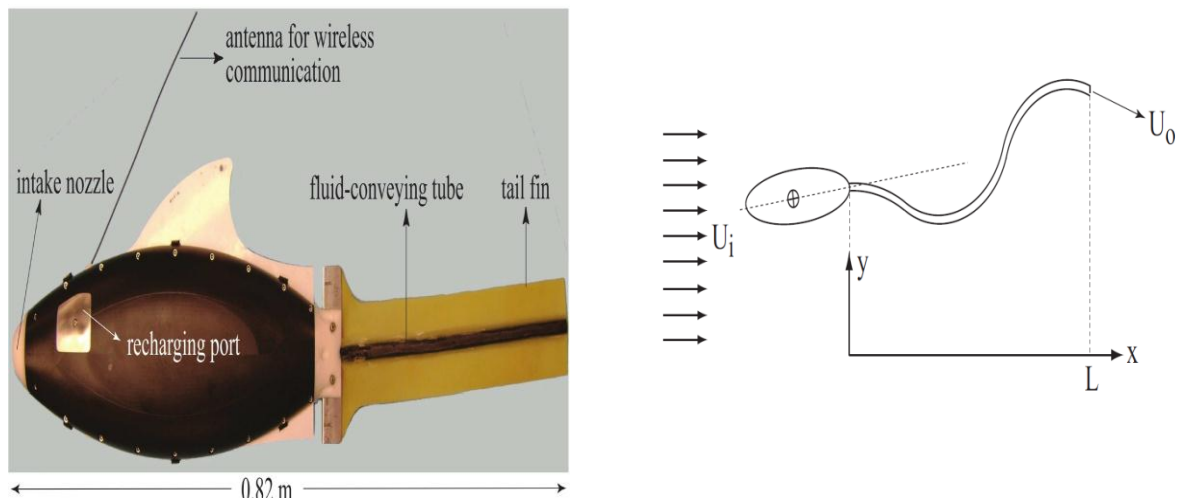


Figure (1). (a)The robotic fish design / (b)The free body diagram [7]

2. Free Vibration Formulation of cylindrical Coil Springs

The cylindrical helical coiled springs has the simplest mathematical model among the other types. The equation of motion for the 12-degree for free vibrations springs in (t, n, b)[1,2]:-

$$\frac{\partial U_t^\circ}{\partial s} = X U_t^n + \frac{T_t^\circ}{c_t} \quad (1)$$

$$\frac{\partial U_n^\circ}{\partial s} = X U_t^\circ + \tau U_b^\circ + \Omega_t^\circ + U_n^\circ / C_n \quad (2)$$

$$\frac{\partial U_b^\circ}{\partial s} = -\tau U_n^\circ - \Omega_n^\circ + \frac{T_b^\circ}{c_b} \quad (3)$$

$$\frac{\partial \Omega_t^\circ}{\partial s} = X \Omega_n^\circ + \frac{M_t^\circ}{D_t} \quad (4)$$

$$\frac{\partial \Omega_n^\circ}{\partial s} = -X \Omega_t^\circ + \tau \Omega_n^\circ + \frac{M_n^\circ}{D_n} \quad (5)$$

$$\frac{\partial \Omega_b^\circ}{\partial s} = -\tau \Omega_n^\circ + \frac{M_b^\circ}{D_b} \quad (6)$$

$$\frac{\partial T_t^\circ}{\partial s} = X T_n^\circ - P_t^\circ + \rho A (\partial^2 U_t^\circ / \partial t^2) \quad (7)$$

$$\frac{\partial T_n^\circ}{\partial s} = -X T_t^\circ + \tau T_b^\circ - P_n^\circ + \rho A (\partial^2 U_n^\circ / \partial t^2) \quad (8)$$

$$\frac{\partial T_b^\circ}{\partial s} = -\tau T_n^\circ - P_b^\circ + \rho A (\partial^2 U_b^\circ / \partial t^2) \quad (9)$$

$$\frac{\partial M_t^\circ}{\partial s} = X M_n^\circ - m_t^\circ + \rho J (\partial^2 \Omega_t^\circ / \partial t^2) \quad (10)$$

$$\frac{\partial M_n^\circ}{\partial s} = T_b^\circ - X M_t^\circ + \tau M_t^\circ - m_n^\circ + \rho I_n (\partial^2 \Omega_n^\circ / \partial t^2) \quad (11)$$

$$\frac{\partial M_b^\circ}{\partial s} = T_n^\circ - \tau M_n^\circ - m_b^\circ + \rho I_b (\partial^2 \Omega_b^\circ / \partial t^2) \quad (12)$$

3. Modeling tools

COMSOL Multiphysics 4.2 simulation environment was used to make this analysis , COMSOL 4.2 is a complete problem-solving tool. MATLAB interface allowed somewhat straight forward modeling of a complex three dimensional helical geometry without resorting to CAD modeling .The analysis was also rather fast ,with meshing and analyzing taking less than 10 seconds .A three dimensional helix was created and meshed in COMSOL . eigenfrequency analysis was conducted to identify the first five vibrational modes along with their frequencies.

4. Case study analysis

A three dimensional helix was created in COMSOL4.2.to get deformation shape for different types of coiled springs. Figure (2) demonstrate different types of coiled springs , figures (3), (4) and (5) illustrate deformed and undeformations shapes for cylindrical, conical and elliptical springs for five mode shape .Table 1 records the results of COMSOL 4.2 when implemented for cylindrical, conical and elliptical springs .

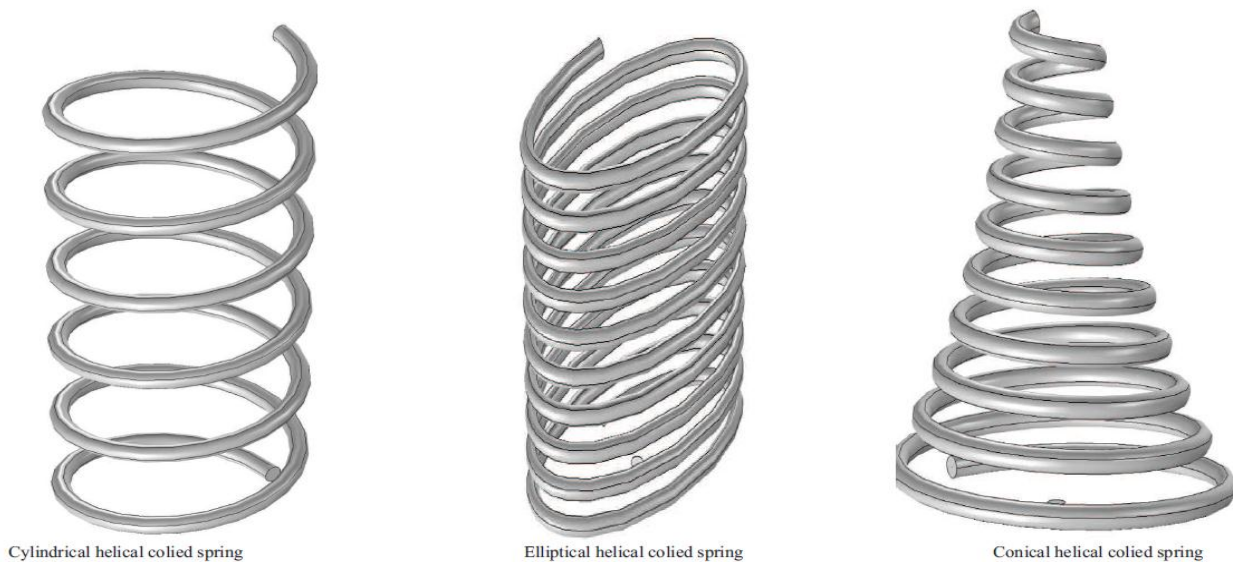


Figure (2).Different types of coiled springs

4.1. Cylindrical Spring analysis

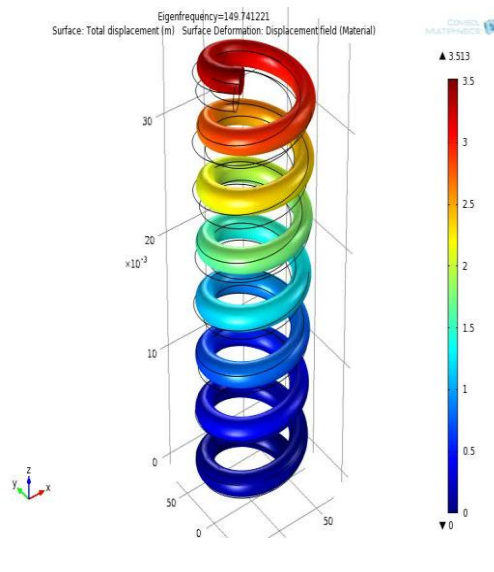
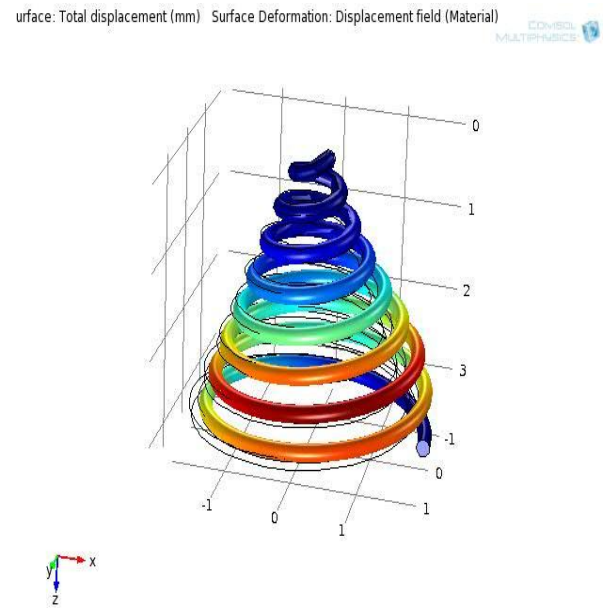


Figure (3). Cylindrical spring deformed & undeformed.

4.2. Conical Spring analysis



Figure(4). Conical spring deformed & undeformed.

4.3. Elliptical Spring analysis

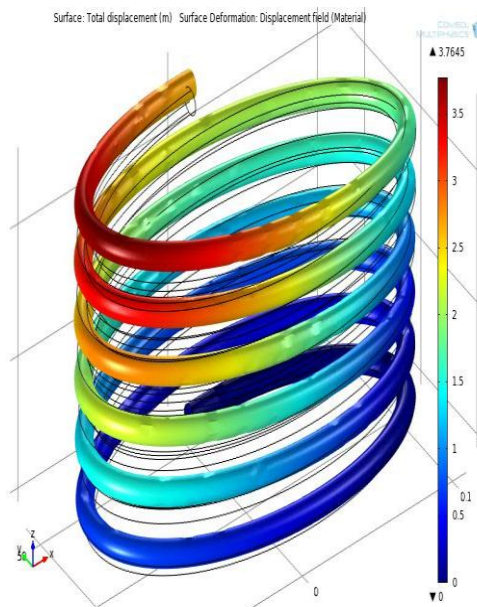


Figure (5).Cylindrical spring deformed & unreformed.

Table. (1). Application for spring steel AISI 4340 ($n=6$, $E=2.0610^{11}$ N/m² $\nu=0.3$, $d=0.005$ m, $a=0.001$, $\alpha=0.00468$, $\rho=7900$ Kg/m³).

Type	Mode1	Mode2	Mode3	Mode4	Mode5
Cylindrical/ PS	19.005	19.019	29.115	32.89	64.72
Yildirim[1]	36.52	36.544	150.627	165.616	201.82
Elliptical/ PS	23.646	25.587	31.500	32.888	53.765
Yildirim[1]	25.402	28.356	31.444	42.171	45.783
Conical/ PS	3.246	3.726	4.672	5.170	5.056
Yildirim[1]	3.200	3.121	4.556	5.443	5.508

PS=Present study

5. Results and Discussions

In this work, the equation of motion in helical spring was, derived from Timoshenko beam theory and Frenet formulae, after applying suitable boundary conditions by fixed one end. The software has been applied to the large deformation analysis of helical springs under axial loading. The Eigen frequency analysis was run across various values of the number of turns n , the wire diameter, and the helix diameter D . This paper presents theoretical analysis of vibration problem of coil springs of arbitrary shape by using COMSOL 4.2. The results can be summarized five mode shape for cylindrical and elliptical springs as shown in figures (10,11) and table (2). For cylindrical spring. Figures (12,13) and table (3) for elliptical spring.

5.1. Cylindrical Spring

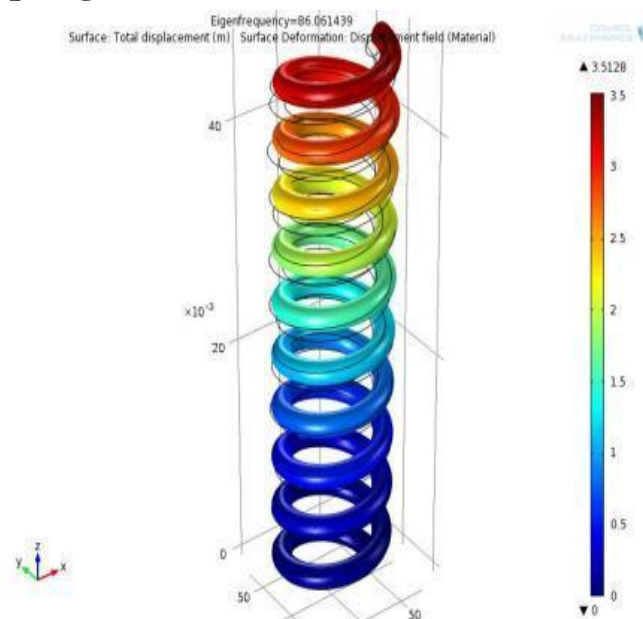
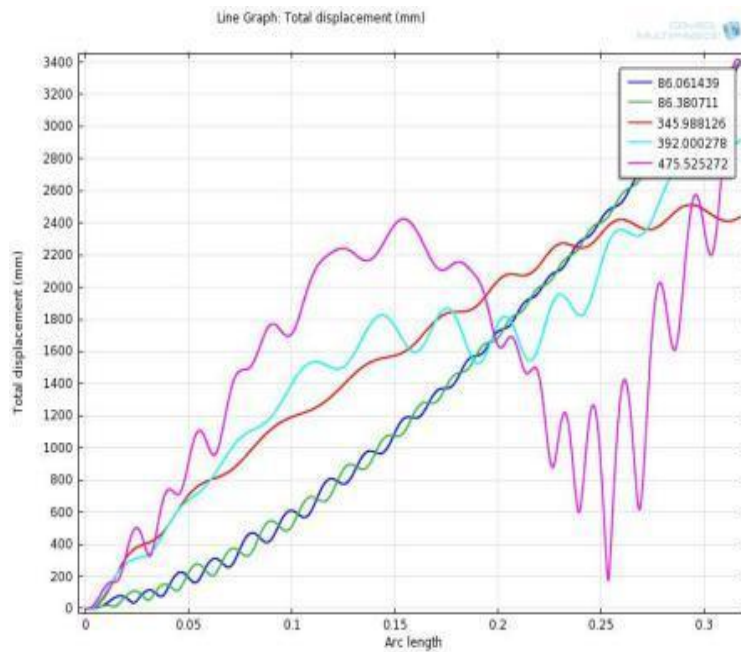


Figure (6). Deformed & unreformed of cylindrical spring

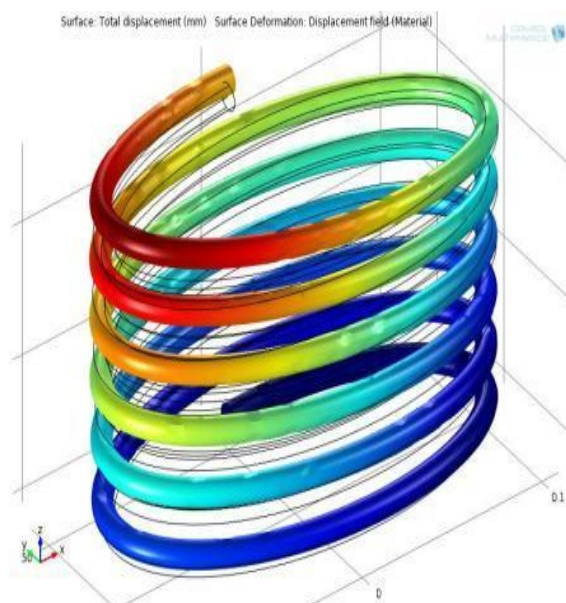


Figure(7). Fifth mode shape of spring fixed one end

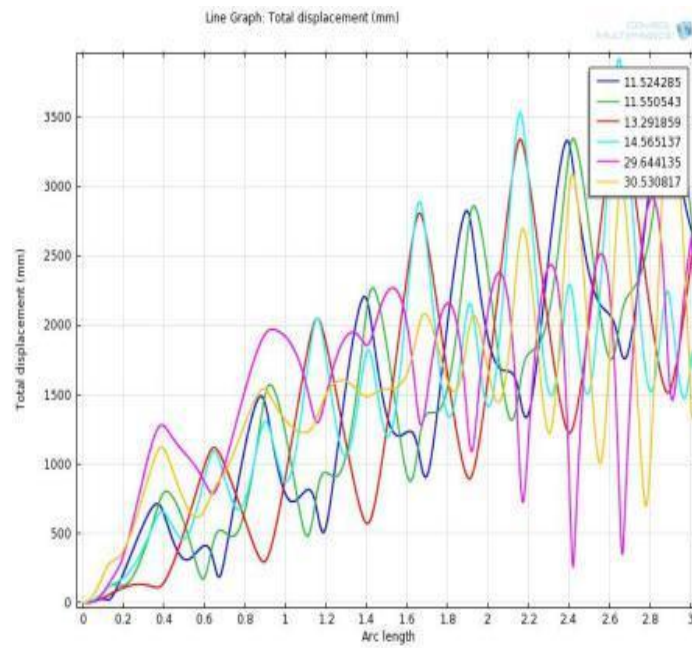
Table (2). Example for a cylindrical spring free vibrations, second with body load =50-150 N, Eigenfrequency for(5) mode shape number of turns =6.

Load	Mode 1	Mode 2	Mode 3	Mode 4	Mode 5
$X=y=z=0$	459.304	509.359	526.678	532.339	906.888
$Y=0$	107.84	108.153	238.845	268.833	474.070

5.2. Elliptical Spring



Figure(8). Deformed & undeformed of elliptical spring fixed one end



Figure(9). Fifth Vibration mode shape of elliptical springs fixed one end

Table (3). Example of an elliptical spring with out load , second with body load, Eigenfrequency for (5) mode shape number of turns =6 .

Load	Mode 1	Mode 2	Mode 3	Mode 4	Mode 5
Y=0	11.524	13.294	14.565	29.644	30.538
X=y=z=0	25.402	28.356	31.444	42.171	45.783

6- Conclusions

The following notes can be extracted from the research results :-

1. Increasing spring turns number (n) will decreases spring stiffness and all resonant.
2. Decreasing spring turn number (n) is a good way to achieve separation between five mode and others.
3. Increasing diameter of the spring wire (d) will increas spring stiffness and increasing all resonant frequencies.
4. Springs having the same material and geometrical properties for elliptical type is more rigid than others types.
5. Some natural Frequencies are very close to each other for the elliptical type as illustrated in figures (14 ,15 ,16) below , which explore the effect of vibrational mode frequencies on spring number of turns(n) for constant pitch angle.
6. Figure (13) shows comparison of vibrational mode frequencies for Conical spring between this study and Yildirim

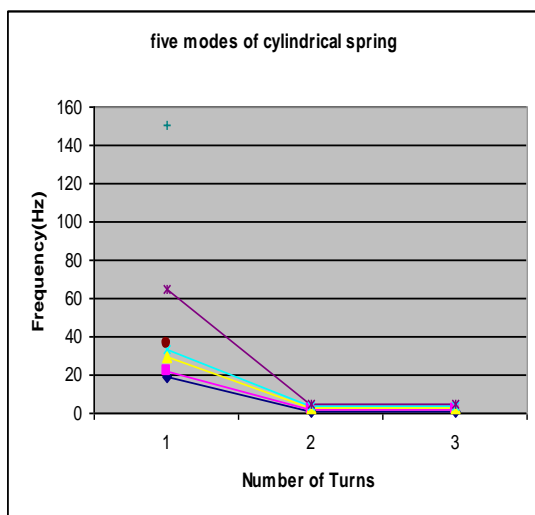
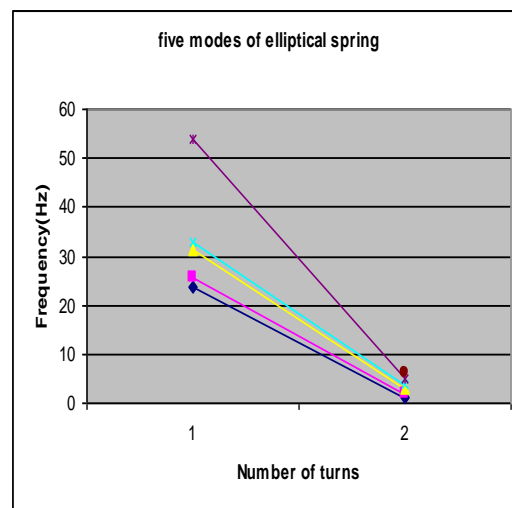
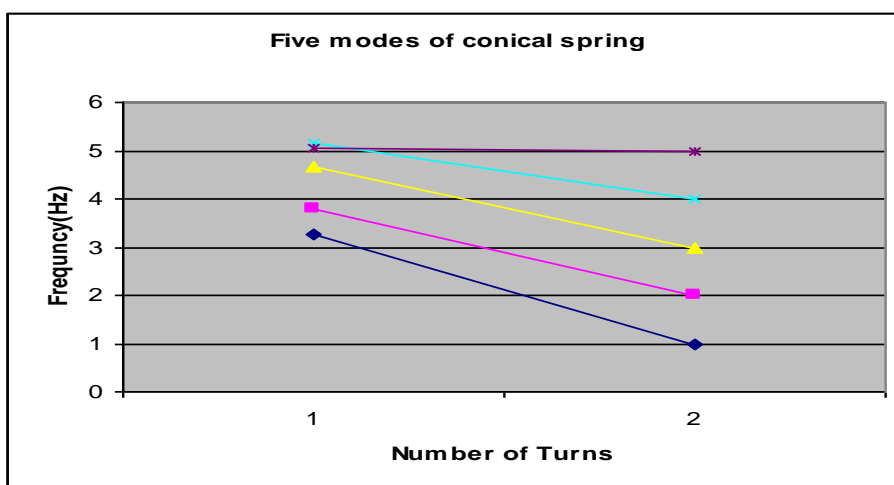


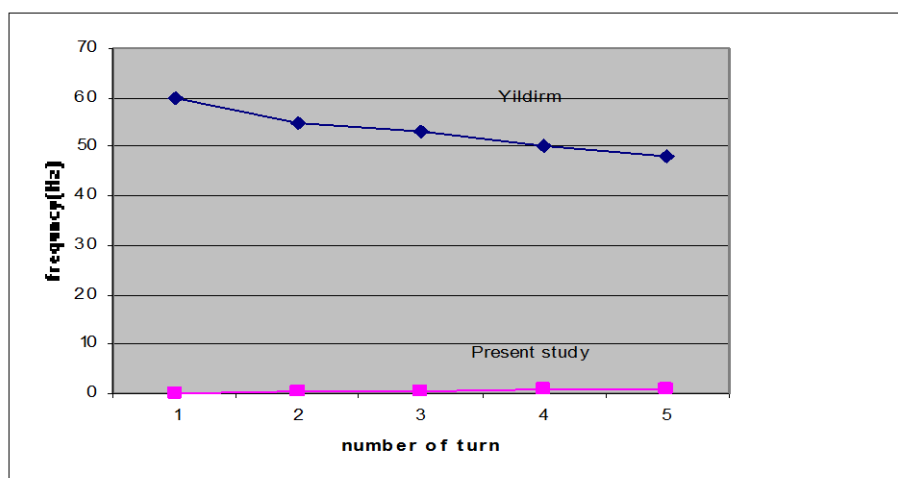
Figure.(10).Vibration mode frequencies on number of turns =6 of cylindrical spring



Figure(11).Vibration mode frequencies on number of turns=6 of elliptical spring



Figure(12).Vibrational mode frequencies on number of turns=6



Figure(13) comparison of vibrational Mode frequencies for Conical springs between this study and Yildirim.

References

1. Yildirim “ Investigation of parameters affecting free vibration Frequency of helical springs” Turkey Vol.39,99-114(1996).
2. Wisam Busool”Free vibration of helicoidal Beas of Arbitrary Shape and Variable Cross section” JULY2002 ,Vol.124/397.
3. Pratheev Sreetharan"Eigenfrequency Analysis of helical spring Electrode" Dec.16 ,2008.
4. A.M. Yu,Y.Hao"Free Vibration analysis of cylindrical springs noncircular cross- sections"J.of sound and vibration 330(2011).
5. V.Yildirim "Free vibration analysis of non-cylindrical coil springs by combined use of the transfer matrix and the complementary function methods"Vol.13,487- 94(1997).
6. Kosuk,Nagaya and Takeda ,Sadahiko, “Free vibration of coil Springs of Arbitaray Shape “Int.J.Numer Method Eng..32.pp1081-1099(1986)
7. Aren "Modeling and simulation of fluttering bioinspired submersible "Ph.D thesis 2011 MSU.
8. V.Yildirim, N. Ince. Natural frequencies of helical springs of arbitrary shape,Journal of Sound and vibraton 204 (1997) 311-29.
9. COMSOL "Introduction to COMSOL multiphysics "2011”.

Study The Effect Of Different Common Beam Sections Having A Constant Cross Sectional Area On The Critical Buckling Load

Dr. Abdul-Wahab Hassan Khuder

Assistant Professor

Technical College-Baghdad

akhuder@yahoo.com

Sabah Khammass Hussein

Lecturer

Technical College-Baghdad

Sabah.Kh1974@yahoo.com

Ammar Azeez Mahdi

Assistant Lecturer

Technical College-Baghdad

Ammaraz83@yahoo.com

SUMMARY:

A simply supported beam is used to calculate the critical buckling load. A common beam sections with constant cross sectional area are used to analyze the results using ANSYS11 program which gives a good results as comparing with the theoretical equation. The critical buckling load depends on the shape and dimensions of beam section which has constant cross sectional area. It observed that the critical buckling load is higher with a wide range of width for thinner hollow rectangular-section than the thicker section and lower for (I, T & L-sections). Changing the width or thickness for U & Z-sections gave a small effect on the critical buckling load. Increasing the thickness of hollow circle beam section gives a decreasing in the critical buckling load. The last beam section gives a higher critical buckling load as comparing with solid circle section of the same cross sectional area. The same phenomenon is found for hollow rectangular-section as comparing with the solid section.

Keywords: A simply supported beam, Critical buckling load.

المستخلص:

تم استخدام عتبة ذات ارتكاز البسيط من الطرفين لحساب حمل الأنبيج الحرج. تم استخدام المقاطع الشائعة من العتبات بثبوت المساحة لتحليل النتائج باستخدام برنامج (ANSYS11) والذي أعطى نتائج جيدة مقارنة مع المعادلة النظرية. حمل الأنبيج الحرج يعتمد على شكل وأبعاد مقطع العتبة الذي يمتلك مساحة ثابتة.

لوحظ من النتائج أن حمل الأنبياع الحرج يكون عالي بمدى واسع للمقطع المستطيل المجوف النحيف مقارنة مع المقطع السميك وتكون قليلة في المقاطع ذات الأشكال (I,T&L). تغيير عرض أو سمك المقطع ذات الأشكال (U&Z) أعطى تأثير قليل على حمل الأنبياع الحرج. زيادة سمك مقطع العتبة الدائري المجوف يعطي نقصان في حمل الأنبياع الحرج وأعطى حمل أنبياع حرج عالي مقارنة مع المقطع الدائري الصلب لنفس مساحة المقطع. نفس الظاهرة الأخيرة لوحظت في المقطع المستطيل المجوف مقارنة مع الصلب.

1. Introduction:

Euler was the first who studied for engineering applications important problem of buckling arising in a simple, monolithic beam loaded axially by a concentrated load. It has been shown from two solutions of the problem due to Timoshenko theory; the elastic foundation increases the critical buckling load of the beam. Starting from the previous classical results, a mechanism to enhance the buckling strength of a cantilevered beam is investigated. In the place of a single, one-element, monolithic cross-section, the use of a bundle of more than one, similar or not, single cross-sections, placed with parallel axes, and staying in free contact along their adjacent boundaries, is proposed [1].

The buckling behavior of an I-beam under combined axial and horizontal loading is examined. It is shown that the actual application location of the axial loading governs the buckling behavior of the long I-beam. Theoretical formulation is developed to determine the critical buckling load for such combined loading configuration from the elastic static theory. Both, the beam deflection theoretical model and the critical load capacity are derived for this combined loading condition. The Finite Element Analysis (FEA) is utilized to apply the axial load on the beam at various configuration locations and it is shown that this application location determines the buckling behavior and the critical load of the buckling of the I-beam [2]. Tapered I-beams can carry a maximum bending moment at a single location while in the rest of the member the moment carrying capacity is considerably lower. Numerous researchers have focused on the investigation of the elastic behavior of tapered I-beams and many theoretical findings have been incorporated into the current specifications. The elastic critical moment is used for determining the design strength against lateral-torsional buckling (LTB) of I-beams with uniform cross-section and a number of coefficients is employed accounting for the boundary conditions, the cross-sectional geometry and the type of transverse loading, while no detailed information is given regarding non-uniform members. Modification factors of the elastic critical moment with reference to the mean cross-section are given for various taper ratios. The approach presented here in can be very easily applied for the design of tapered beams against lateral-torsional buckling [3].

The lateral-torsional buckling of composite strip and I-beams is considered. The geometrically exact governing equations are simplified by consistently regarding certain configuration parameters as small. The assumption that these parameters are indeed small is equivalent to the assumption that the square of the maximum prebuckling cross-sectional rotation due to bending is small compared to unity. The analysis takes into account various refinements of previously published results, elastic coupling, and the offset of the load from the centroid, and, of course, prebuckling deflections. The analysis is thereby reduced to a single fourth-order differential equation and boundary conditions, all of which are derivable from a corresponding energy expression. Using this comparison function, a formula for the buckling load as a function of the small parameters of the problem is found and validated. With certain exceptions regarding the load offset parameter; the formula provides results which agree quite well with the numerical solution of the exact equations as long as all the small parameters remain small. However, the load offset parameter always appears in the governing equations as multiplied by a ratio of stiffness, which can become large, especially for composite I-beams [4].

In steel construction the flange of a steel I-beam is usually coped to allow clearance at the connection. Local web buckling at the coped region may occur when the cope length is long and/or the cope depth is large, provided that lateral-torsional buckling of the beam is prevented. In order to verify such recommendation, an experimental and numerical investigation of coped I-beams with stiffeners at the coped region was conducted and reported. The local web buckling could not be prevented efficiently if only horizontal stiffeners were provided at the coped region. Both the test and the numerical results showed that the horizontal stiffeners at the cope displaced laterally due to gross web distortion. It was found that for cope depth to beam depth ratio $(d/D) \geq 0.3$, both horizontal and vertical stiffeners are required in order to prevent local web buckling at the cope region [5].

A method of identifying the buckling load of a beam-column is presented based on a technique named Multi-segment Integration technique. This method has been applied to a number of problems to ascertain its soundness and accuracy. The boundary conditions mean that, i) it is hinged at both ends; ii) it is fixed at both ends; and iii) it is fixed at one end and hinged at the other end. The results obtained by Finite Difference method are compared in order to determine the efficiency of this method [6].

In the present work, the lateral buckling response of a simply supported beam, subjected to a mid span concentrated load is thoroughly discussed. Assuming that the loss of stability occurs through divergence, we consider the equilibrium in a slightly bent configuration in which vertical and lateral deflections as well as angles of twist are developed. This state of equilibrium by a system of three differential equations with non-constant coefficients. Clearly, a closed form solution of the above system cannot be, in general, obtained. Therefore, one has to resort to approximate analytical solutions. Hence, an analytic approximate technique for solving the above system of differential equations is successfully employed [7]. The determination of the critical (elastic) level of loading is not only of theoretical, but also of practical importance, since in many current design codes, the design resistance of a beam against lateral buckling, even in the case of inelastic buckling, is based on the corresponding value of elastic buckling. The problems related to lateral buckling, results are obtained applying approximate procedures as well as finite element methods [8]. Approximate shape functions are also used, for establishing the post buckling behavior in cases of lateral (bending without axial force) [9], or lateral torsion buckling, [10, 11]. The effect of stacking sequences, fiber orientation angles, boundary condition and delamination numbers on the critical buckling loads of the laminated composite beams have been investigated analytically and numerically. Firstly, an analytical model is presented to take into consideration the reduction in stiffness of the beam due to the presence of the delamination in the beam. Then, two-dimensional finite element models for the composite beams having single/double middle delamination have been established by using contact element at ANSYS commercial program. A good agreement between theoretical and finite element results has been found. It is seen that the buckling loads vary with changing stacking sequences, orientation angles and boundary conditions. The results show that a reduction in the critical buckling loads occurs when delamination length increases. In the numerical analysis, the appropriate buckling load values of the laminated beams are obtained by using normal penalty stiffness that is chosen as elasticity modulus for contact elements in the delamination region [12]. This work deals with the lateral buckling of beams on which a concentrated load was applied through a bar subjected to a compressive force of constant direction. For the same cases of loading the problem of lateral buckling of beams under directed loading with the aid of finite element computer programs. Non-conservative problems are of paramount importance in modern structural design. The present paper deals with the lateral buckling and to calculate the critical buckling load. ANSYS11 program are using to analyze the results which gives a good results as comparing with the theoretical equation.

2. Theory of Columns Buckling (Euler Columns):

A assume a bar of length (L) loaded by a force (P) acting along the longitudinal beam axis on pinned end. As shown in Figure (1), the bar is bent in the positive y-direction, this required negative moment, and hence:

$$M = -Py \quad (1)$$

Where:

M : moment (N.m).

P : the applied load (N).

y : moment arm (m).

If the bar should happen to bend in the negative y-direction a positive moment would results. The resulted moment can be written in the following equation:

$$EI \frac{d^2 y}{dx^2} = M \quad (2)$$

Where:

E : modules of elasticity (N/m²).

I : second moment of inertia (m⁴).

Sub Eq. (1) in Eq. (2):

$$\frac{d^2 y}{dx^2} = \frac{-Py}{EI} \quad (3)$$

or

$$\frac{d^2 y}{dx^2} + \frac{P}{EI} y = 0 \quad (4)$$

The solution of the above second order differential equation is as follows:

$$y = A \sin\left(\sqrt{\frac{P}{EI}}\right)x + B \cos\left(\sqrt{\frac{P}{EI}}\right)x \quad (5)$$

Where (A) and (B) are constants of integration and can be found from the boundary conditions.

In this work, the deflection is zero at both ends ($x=0, L$). The first boundary conditions give ($B=0$) and the other give:

$$A \sin\left(\sqrt{\frac{P}{EI}}\right)L = 0 \quad (6)$$

If $A=0$; no buckling occurs, therefore:

$$\sin\left(\sqrt{\frac{P}{EI}}\right)L = 0 \quad (7)$$

Equation (7) is satisfied by: $\sqrt{\frac{P}{EI}}L = n\pi$

Where:

n: is an integer.

Solving for $n=1$ gives the critical load, P_{cr} :

$$P_{cr} = \frac{\pi^2 EI}{L^2} \quad (8)$$

Which called the “Euler column formula”

The critical applied stress, σ_{cr} (N/m²), is:

$$\sigma_{cr} = \frac{P_{cr}}{A} = \frac{\pi^2 EI}{AL^2} \quad (9)$$

The relation of radius of gyration, (k) for any cross sectional area is given by:

$$k = \sqrt{\frac{I}{A}} \quad (10)$$

Sub Eq. (10) in Eq. (9):

$$\sigma = \frac{P_{cr}}{A} = \frac{\pi^2 E}{(L/k)^2} = \frac{\pi^2 E}{S^2} \quad (11)$$

The term (S) is known as the slenderness ratio. And the solution of Eq. (11) is called as a critical unit load. The buckling is occurred when the critical buckling stress is occurred below the yielding point of material where the “Euler column formula” is applicable. This occurred for long columns. The fail is occurs by compression for short columns. According to its length, the columns are classified as:

- (1) Short if $S < 30$.
- (2) Long if $S > 120$.
- (3) Intermediate $120 > S > 30$.

2-1. Principles Axis of Inertia:

Consider the cross sectional area of beam lies in the (y - z) plane, Figure (1). In Euler column formula, the moment of inertia is taken as the minimum moment of inertia either about the (y) or (z)-axis for the beam section which has a moment of inertia ($I_{yz}=0$). This is satisfied for the following beam section (used in this work):

- 1- Solid rectangular or square section.
- 2- Hollow rectangular or square section.
- 3- Ring or Hollow circular section.
- 4- Channel section.
- 5- T-section.
- 6- I-section.

The other type of beam section used in this work (L & Z-section) give a none zero value of ($I_{yz} \neq 0$); where:

$$I_{yz} = A\bar{y}\bar{z} \quad (12)$$

There are two values of “ θ ” which locate the position of principle axes of inertia (Y, Z) for a given cross sectional area:

$$\tan 2\theta = -\frac{2I_{yz}}{I_y - I_z} \quad (13)$$

The values of principle moment of inertia are given by:

$$I_Y = \frac{I_y + I_z}{2} + \sqrt{\left(\frac{I_z - I_y}{2}\right)^2 + I_{yz}^2} \quad (14)$$

$$I_Z = \frac{I_y + I_z}{2} - \sqrt{\left(\frac{I_z - I_y}{2}\right)^2 + I_{yz}^2} \quad (15)$$

Where:

I_y, I_z : second moment of inertia about the (y & z-axis).

I_Y, I_Z : principle moment of inertia about the principle axis (Y & Z-axis).

3. Finite Element Methods Using ANSYS11 Program:

3-1. Material of Beam:

A carbon steel of type (Structural) is used for beam material. The yield stress is (250 Mpa), ultimate stress (400Mpa), Poisson's ratio (0.29) and have a young modulus of elasticity (E=200Gpa).

3-2. Dimensions of Beam:

A constant cross sectional area is used for various beam section (common beam section). To ensure that the buckling is achieved and be applicable with Euler column formula, a suitable cross sectional area as compared with beam length must be choose to ensure that the buckling of beam within the yield region (satisfy Euler column formula). Hence the following beam dimensions are used for a different common beam cross section:

$A = 100 \text{ mm}^2$ (beam cross sectional area).

$L = 2000 \text{ mm}$ (beam length).

Where, the values of (S) in Eq. (11) is more than (120) for each of beam dimension used (long beam). The following beam cross sectional are used in this work:

- | | |
|--------------------------------|-------------|
| 1- Hollow rectangular-section. | - Table (1) |
| 2- Channel-section. | - Table (2) |
| 3- L-section. | - Table (3) |
| 4- T-section. | -Table (3) |

- 5- I-section. - Table (4)
- 6- Z-section. -Table (4)
- 7- Hollow circle-section. - Table (5)
- 8- Solid circle-section. - Table (6)
- 9- Solid circle and square-section. - Table (6)

In each type of thin cross section, a finite number of thickness (t), width (W_1) and height (W_2) are used such that the cross sectional area still constant ($A=100 \text{ mm}^2$).

Hence, a three sets of dimensions used with thickness value ($t = 1, 2, 3 \text{ mm}$) as shown in tables (1-4). For each thickness value, a wide range of sectional width is used. For example, in the first beam section, (Table-1), the width values are ($W_1=5, 10, 15 \dots 50 \text{ mm}$) for the first set of thickness ($t_1=1 \text{ mm}$). The other dimension (W_2) is calculated such that the total cross section area equal to ($A=100 \text{ mm}^2$). Where:

$$A=2W_1t+2(W_2-2t)*t=100 \text{ mm}^2$$

For the hollow circular section (Table-5), the values of thickness are ($t=1, 2, 3, 4$ and 5 mm). Hence the other dimensions are calculated such that the total cross section area is constant ($A=100 \text{ mm}^2$). Table (6) gives the values of solid circle and square dimensions with the same above area. The moment of inertia (I_y, I_z, I_{yz}), and other properties are calculated by ANSYS11 program for each beam section.

3-3. Finite Element Method:

Each of the previous cases are modeled using finite element method with element type (structural beam, 3D finite strain, 3 nodes 189) in ANSYS11 program. The boundary conditions of beam are simply supported as in Figure (1). Hence, a half-length of beam is used to analyze the problem. One end is considered as a fixed end (fixed all degree of freedom). The other end is simply which represent the end of the applied load as shown in Figure (2).

A ten element is used (11 node). Each element section is meshed with a fine mesh. The solution of problem has been done initially with static solution and then with buckling solution with ANSYS11 program. The resulted data is recorded as a critical buckling load for each case.

4. Results & Discussions:

The resulted data from the theoretical equation (Euler column formula) which include the critical buckling load is calculated for each case of beam section with the same beam length,

cross sectional area and material properties as mentioned. Those values of critical buckling load are plotted and compared with those recorded from the ANSYS11 program [Figures (3 - 9)]. Hence a good agreement has been found between the theoretical and FEM values of this force for each case of the beam section (error = 0.1- 0.3%) and the results for each beam section can be explained as follow:

4-1. Hollow Circular-Section:

Increasing the thickness of circular section resulted in decreasing the critical buckling load (P_{cr}). A sharp decreasing for (P_{cr}) is found as the uniform increasing in thickness. Hence, the force (P_{cr}) is (6256N) at ($t=1\text{mm}$) which reduce to (404N) at ($t=5\text{mm}$), or in another representation, the force decrease at a percentage of (94%) through the increasing in thickness at a percentage of (80%). This is due to the decreasing in the moment of inertia. It can be say that a thinner ring beam section gives a good buckling property than the thicker ring beam section, Figure (3).

4-2. Hollow Rectangular-Section:

Variation of (P_{cr}) with width range (W_1), Table (1), is plotted for three values of thickness in Figure (4). As it has been shown, the critical buckling force is increase uniformly until reach the maximum value and then decrease for each thickness value. A thinner section gives a higher critical buckling load as comparing with the thicker section for each value of section width (W_1). Increasing the width (W_1) result in increasing the minimum moment of inertia which results in increasing (P_{cr}) according to Eq.(8). Hence the maximum value of ($P_{cr}=4840\text{N}$) is recorded at the minimum thickness ($t=1\text{mm}$) and ($W_1=25\text{mm}$). Therefore, this type of beam section gives a good buckling property with a thinner section.

4-3. I-Section:

As in Figure (5), the critical buckling load increase with increasing the width (W_1) for each value of thickness used in table (4), a continuous increasing is observed without decreasing. That means the maximum critical buckling load is observed at the final value of width (W_1) used for each thickness. Where ($P_{cr} \max = 4685\text{N}$, at ($t=1\text{mm}, W_1=40\text{mm}$), ($P_{cr} \max = 1319\text{N}$, at ($t=2\text{mm}, W_1=20\text{mm}$) and ($P_{cr} \max = 836.5\text{N}$, at ($t=3\text{mm}, W_1=15\text{mm}$). That means, a good buckling property can be found in the thinner wide I-beam section. The narrow

thin section gives a lower (P_{cr}). Where (P_{cr}) is higher for ($t=2\&3\text{mm}$) for width range ($W_1 < 20\text{mm}$).

4-4. L-Section:

Nearly, in Figure (6), the same (P_{cr}) is observed for ($t=2\&3\text{mm}$) at a width ($W_1 < 15\text{mm}$) which higher than that for thickness ($t=1\text{mm}$). The values of (P_{cr}) are decrease with increasing width ($W_1 > 20\text{mm}$) for ($t=3\text{mm}$) and at ($W_1 > 30\text{mm}$) for ($t=2\text{mm}$). While, the force (P_{cr}) is continuous in increasing with increasing width at ($t=1\text{mm}$) which gives a higher values for width ($W_1 > 30\text{mm}$) than those for the other thickness (2 & 3mm) and reach a maximum value at the final width ($P_{cr}=2900\text{N}$).

4-5. T-Section:

The critical buckling load is increased gradually with width (W_1) for to values of thickness ($t=2\&3\text{ mm}$) and then decreased at ($W_1=20\text{ mm}$) for thickness ($t=3\text{mm}$) and at ($W_1=30\text{ mm}$) for thickness ($t=2\text{mm}$). The critical buckling load is increased without decreasing for the first thickness of beam section as in Figure (7). Which gives a good buckling property as comparing with those for thickness ($t=2\&3\text{ mm}$) for width ($W_1 > 34\text{mm}$). A wide range of width gives a good buckling property for beam section of thickness ($t=2\text{mm}$) as comparing with that of thickness ($t=3\text{mm}$).

4-6. U-Section:

Nearly, the same critical buckling force has been shown for each set of beam section with each value of the width. This load increase gradually with width until reach the maximum value at ($W_1=35\text{mm}$), ($P_{cr})_{max}= 6522\text{N}$, for the first set of beam section ($t=1\text{ mm}$) and then decrease, Figure (8).

4-7. Z-Section:

In general, the critical buckling is increase gradually and then decrees for each set of beam thickness set during increasing the beam width. Nearly, the same value of (P_{cr}) is found for a wide range of beam thickness set. The maximum value of (P_{cr}) is found at ($W_1=30\text{mm}$), ($P_{cr})_{max}= 2365\text{N}$, Figure (9).

4-8. Solid-Section:

To compare the results of the above thin beam sections with those of solid sections (the same cross sectional area), the value of critical buckling force is observed ($P_{cr} = 411N$) for solid square section and ($P_{cr} = 393N$) for solid circle section, Table (6). Hence, a solid square section gives a good material buckling property than those of circle beam section. But a thin beam sections are a better buckling property than those of solid beam section for wide range of thickness and width. A sample of deformed and un-deformed L-beam of Figure (2b) is shown in Figure (10). The 4-mode buckling shapes for this section are shown in Figure (11).

5. Conclusions:

From the previous results, it can be concluding:

- 1- A hollow thin circle and rectangular beam section gives higher critical buckling load as comparing with those of thick section.
- 2- Increasing the width of rectangular section results in increasing (P_{cr}) until reach a maximum value and then decrease for each thickness value.
- 3- A lower critical buckling load is observed for thinner I-beam section as comparing with those of thick section for each value of beam section.
- 4- The critical buckling load increase with increasing the width of I-beam section without decreasing at any value of width or thickness of beam.
- 5- The L & T- section, the critical buckling load is continuous increasing with increasing width for the beam section thickness ($t=1$ mm). And reach a maximum value and then decreased with increasing width for the other beam thickness ($t=2$ & 3 mm).
- 6- The critical buckling load is lower for L-beam section at a thickness ($t=1$ mm) as comparing with the other two thickness at the range of ($W_1 < 30$ mm) and higher at the range of ($W_1 > 30$ mm).
- 7- The critical buckling load is lower for T-beam section at a thickness ($t=1$ mm) as comparing with the other two thickness at the range of ($W_1 < 34$ mm) and higher at the range of ($W_1 > 34$ mm).
- 8- Nearly, the same critical buckling load has been observed for U & Z-beam section during a wide range of width and thickness.
- 9- A solid circle or rectangular beam gives a lower buckling load than thinner section.
- 10- Changing the shape of beam section with the same area result in changing in the critical buckling load.

- 11- The maximum critical buckling load has been found in the thinner U-beam section with ($t=1\text{mm}$ & $W_1=35\text{mm}$), ($P_{cr})_{max} = 6522\text{N}$).
- 12- The suggested FE model in the ANSYS11 program gives good results of (P_{cr}) as comparing with (Euler column formula).

6. REFERENCES:

- [1] A. Michalopoulos et al., "On The Buckling of Fiber-Bundle Type Beams", Jordan Journal of Civil Engineering, Vol.1, No.1, 2007.
- [2] Amir Javidinejad, Zodiac Aerospace, " Buckling of Beams and Columns Combined Axial and Horizontal Loading With Various Axial Loading Application Locations", Journal of Theoretical and Applied Mechanics, Vol. 42, No.4, 2012, pp.19-30.
- [3] Ioannis G. Raftoyiannis and Theodore Adamakos, "Critical Lateral-Torsional Buckling Moments of Steel Web-Tapered I-beams", The Open Construction and Building Technology Journal, Vol. 4, No.2, 2010, pp.105-112.
- [4] Dewey H. Hodges, David A. Peters, " Lateral-torsional buckling of cantilevered elastically coupled composite strip and I-beams", International Journal of Solids and Structures 38 (2001), pp.1585-1603.
- [5] Michael C.H. Yam et al. "The Local Web Buckling Strength of Stiffened Coped Steel I-Beams", Steel Structures 7 (2007), pp.129-138.
- [6] Goutam Saha and Sajeda Banu, "Buckling Load of A beam-Column for Different End Conditions Using Multi-Segment Integration Technique ", ARPN Journal of Engineering and Applied Sciences, Vol.2, NO. 1, February 2007.
- [7] Trahair N.S., *Flexural-Torsional Buckling of Structures*, FN Sport, London, 1993.
- [8] Wang C.M., Wang L. & Ang K., *Beam-Buckling Analysis Via Automated Rayleigh - Ritz Method*, Journal of Structures Engineering , 1994, pp. 200-211.
- [9] Ioannidis G., Marenholtz O. & Kounadis A.N., *Lateral Post-Buckling Analysis of Beams*, Archive of Applied Mechanics, 1993, pp. 151-158.
- [10] Kounadis A.N. and Ioannidis G.I., *Lateral Post-Buckling Analysis of Beam Columns*, Journal of Engineering Mechanics, 1994, pp.695-706.
- [11] Ioannidis G.I., Kounadis A.N., *Lateral Elastic Post Buckling Analysis of Elastically Rotationally Restrained I-beam Columns*, Proc. 1st European Conference on Steel Structures, Athens. 1995, pp. 41-46.

- [12] Gokmen Atlihan, *Buckling Analysis of Delaminated Composite Beams*, Indian Journal of Engineering and Materials Sciences, Vol.20, August 2013, pp.276-282.

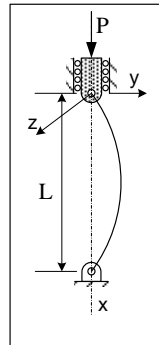
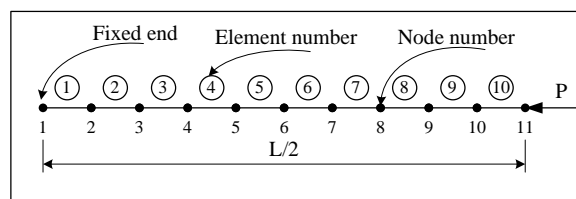
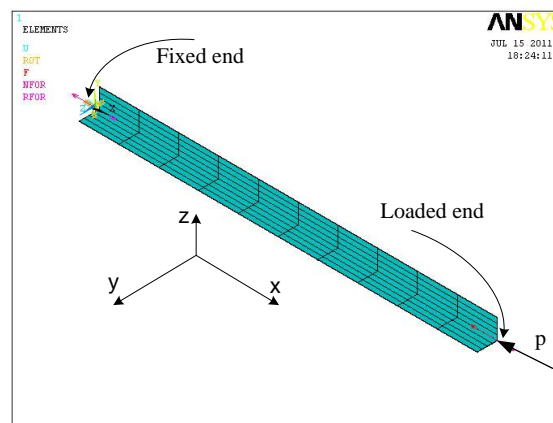


Figure (1) Buckling of pin-pin ends beam.



(a) Schematic Graph for all beam sections.



(b) ANSYS model for L-section ($W_1=50$, $W_2=51$ & $t=1\text{mm}$).

Figure (2) Finite element model of half beam length with boundary conditions and the applied load.

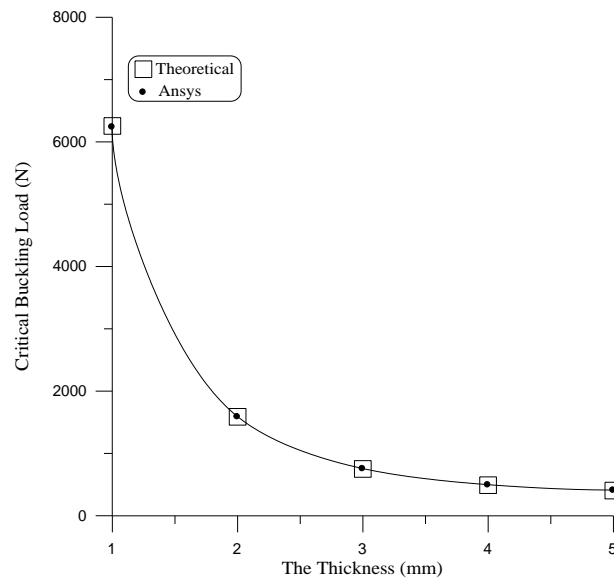


Figure (3) Variation of critical buckling load with thickness for Hollow circle-section.

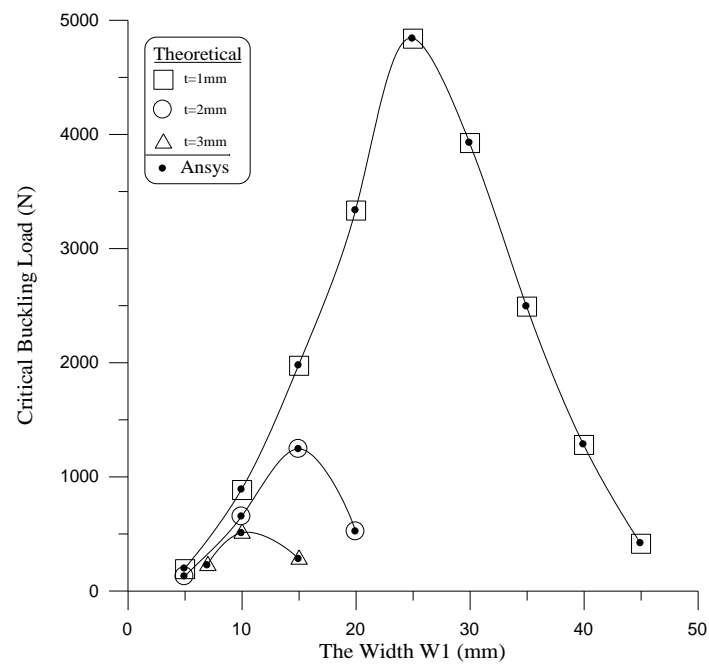


Figure (4) Variation of critical buckling load with width for Hollow rectangular-section.

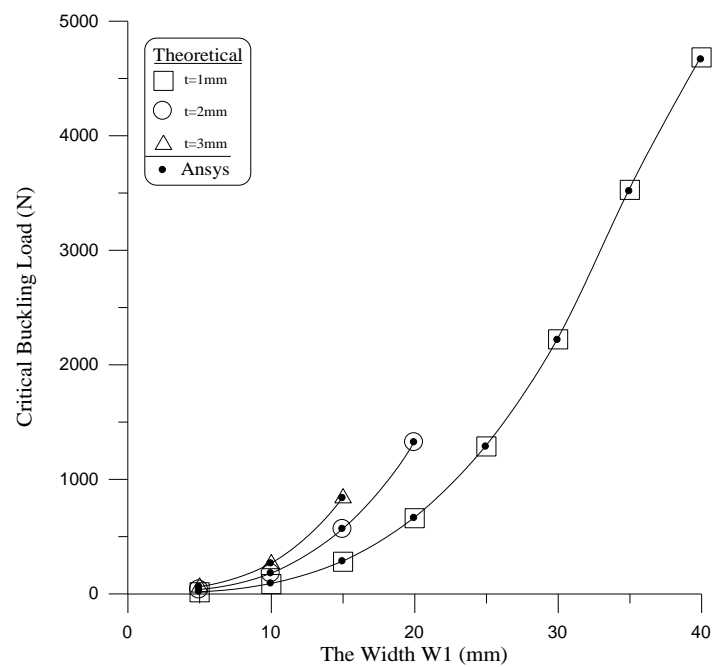


Figure (5) Variation of critical buckling load with width for I-section.

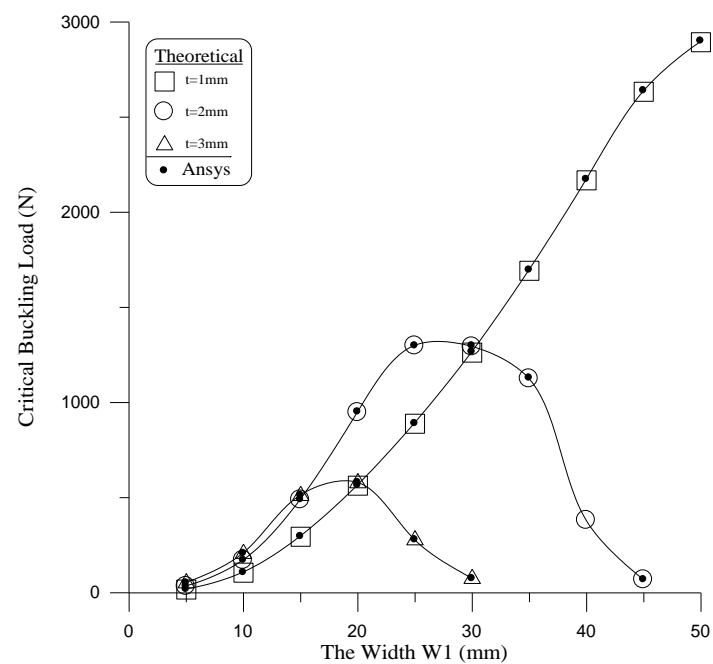


Figure (6) Variation of critical buckling load with width for L-section.

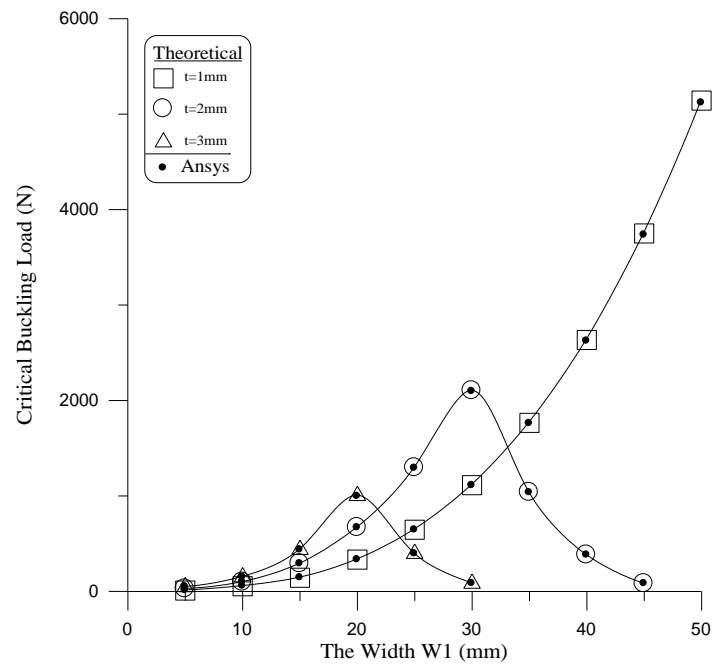


Figure (7) Variation of critical buckling load with width for T-section.

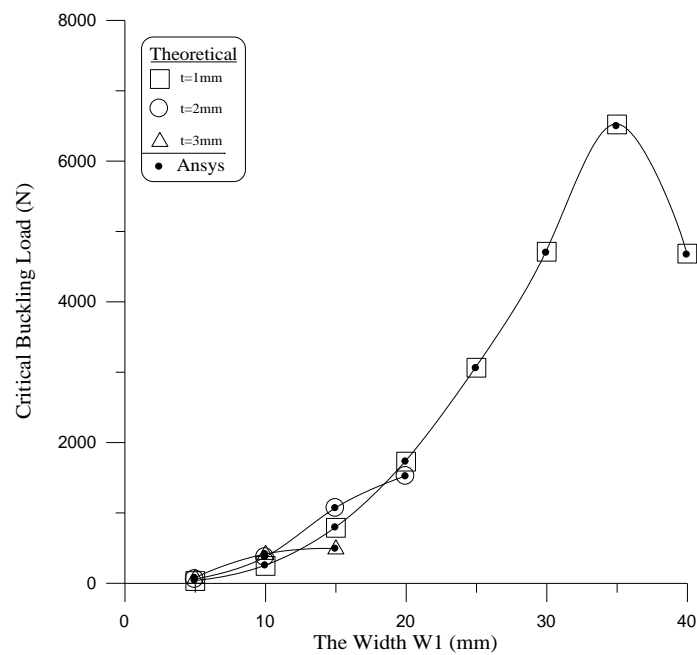


Figure (8) Variation of critical buckling load with width for U-section.

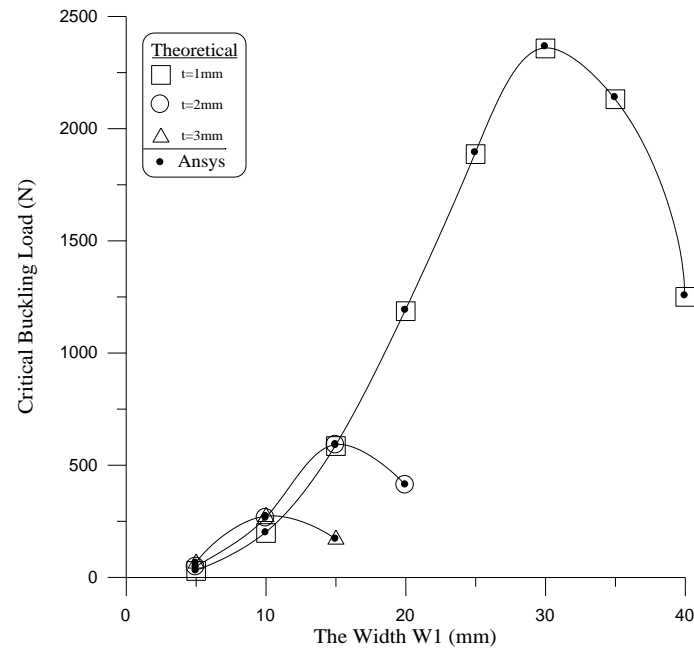
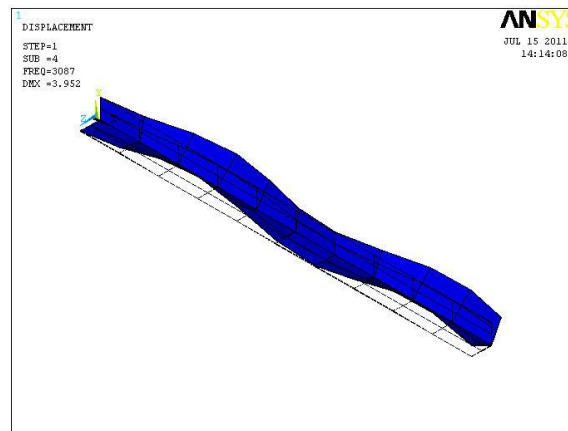
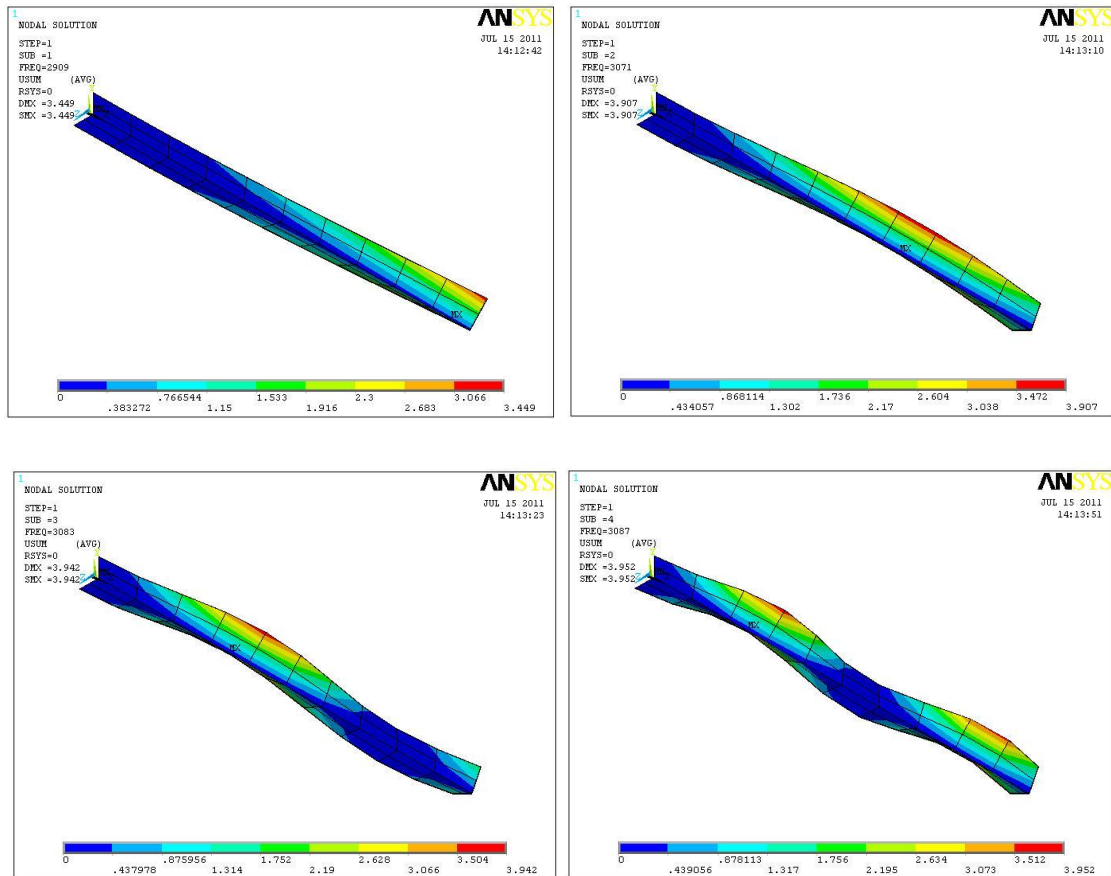


Figure (9) Variation of critical buckling load with width for Z-section.



Figure(10) The deformed and un-deformed L-beam for mode shape - 4.



Figure(11) The deformed L-beam with four mode shapes.

Table (1) Dimensions of Hollow rectangular-section.

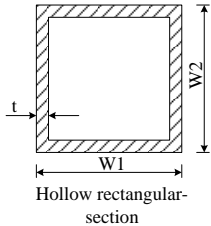
t=1mm		t=2mm		t=3mm	
W1(mm)	W2(mm)	W1(mm)	W2(mm)	W1(mm)	W2(mm)
5	47	5	24	7	15.6666
10	42	10	19	10	12.6666
15	37	15	14	15	7.66666
20	32	20	9	 <p>Hollow rectangular-section</p>	
25	27	25	4		
30	22				
35	17				
40	12				
45	7				
50	2				

Table (2) Dimensions of channel-section.

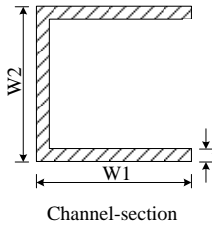
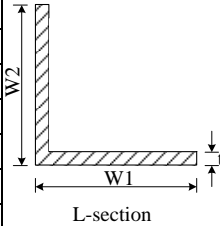
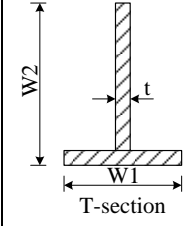
t=1mm		t=2mm		t=3mm			
W1(mm)	W2(mm)	W1(mm)	W2(mm)	W1(mm)	W2(mm)		
5	92	5	44	5	29.3333		
10	82	10	34	10	19.3333		
15	72	15	24	15	9.3333		
20	62	20	14				
25	52						
30	42						
35	32						
40	22						

Table (3) Dimensions of L and T-section.

t=1mm		t=2mm		t=3mm	
W1(mm)	W2(mm)	W1(mm)	W2(mm)	W1(mm)	W2(mm)
5	96	5	47	5	31.3333
10	91	10	42	10	26.3333
15	86	15	37	15	21.3333
20	81	20	32	20	16.3333
25	76	25	27	25	11.3333
30	71	30	22	30	6.3333
35	66	35	17		
40	61	40	12		
45	56	45	7		
50	51				



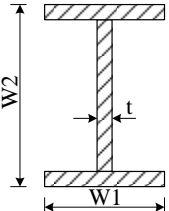
L-section



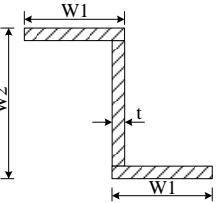
T-section

Table (4) Dimensions of I and Z-section.

t=1mm		t=2mm		t=3mm	
W1(mm)	W2(mm)	W1(mm)	W2(mm)	W1(mm)	W2(mm)
5	92	5	44	5	29.3333
10	82	10	34	10	19.3333
15	72	15	24	15	9.3333
20	62	20	14		
25	52				
30	42				
35	32				
40	22				



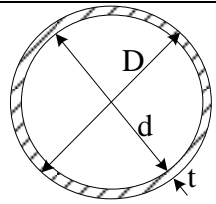
I-section



Z-section

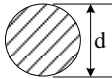
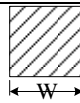
Table (5) Dimensions of Hollow Circle-Section.

t (mm)	d(mm)	D(mm)
1	30.831	32.831
2	13.915	17.915
3	7.61	13.61
4	3.9577	11.957
5	1.36	11.366



Hollow shaft-section

Table (6) Dimensions of Solid Circle and Squire-Section.

d=11.2837 mm	 <p>Solid circle-section</p>
W=10mm	 <p>Solid square-section</p>

Effect of Coolant Jet Holes Direction on Film Cooling Performance

Dr. Assim H. Yousif, Dr.Amer M. Al-Dabaghand Dr.Muwafag Sh. Alwan

University of Technology, Baghdad, Iraq

Abstract

The film cooling effectiveness and local heat transfer coefficient for coolant jet holes direction (orientation angle), have been investigated. Experimental investigations were done on a flat plate by using a single test transient IR thermograph technique. Evaluation of the cooling performance is obtained by estimated both film cooling effectiveness and heat flux ratios. Three models of coolant jet holes are investigated, each model consists of two rows of holes arranged in a staggered way with different orientation angles. Model (1) downstream row with acute angle and the upstream row with obtuse angle; model (2) both rows with obtuse angles, while model (3) both rows with acute angles. The holes diameter is 4mm, the longitudinal distance between the upstream and downstream rows (X/D) is $4D$, and the span distance between two neighboring holes (S/D) is $3D$. Three blowing ratios of ($BR = 0.5, 1.0$, and 1.5) were used in the investigation program. In order to predict the flow behavior numerically for the cases under investigation CFD code is introduced. The numerical investigation shows two large vortices large counter rotating vortex pair and horseshoe vortices, both vortices have major effects on cooling performance. The experimental results showed that the film cooling effectiveness increases as blowing ratio increases for models (1 and 2), while decreases for model (3), and model (1) provide better performance than the others at high blowing ratios.

تأثير اتجاه فتحات البثق البارد على الأداء الحراري لغشاء التبريد

تم دراسة تأثير اتجاه فتحات البثق البارد (زاوية الاتجاه والميل) على فعالية غشاء التبريد و معامل انتقال الحرارة الموقعي. حيث تم إجراء التجارب عملية باستخدام تقنية الصورة الحرارية للأشعة تحت الحمراء (IR) على صفيحة مستوية بألية الفحص الأنثالي الواحد. أن الحصول على تقييم أداء التبريد تم باستخدام فعالية غشاء التبريد وتقنية نسبة الفيض الحراري. وقد تم اختبار ثلاث عينات، كل عينة من هذه العينات تحتوي على صفين من الثقوب المرتبة بشكل متعرج وزوايا اتجاه مختلفة. العينة الأولى الصف الامامي بزواوية نفث حادة والصف الخلفي بزواوية نفث منفرجة، والعينة الثانية كان صفي النفث بزواويتين منفرجتين والعينة الثالثة كان صفي النفث بزواويتين حادتين. تم تثبيت قطر الثقوب بمقدار ($D=4\text{ mm}$)، المسافة الطولية بين الصفين ($X/D=4$)، والمسافة البينية (العرضية) بين فتحات الصف الواحد بمقدار ($S/D=3$). أجريت التجارب باستعمال ثلاث نسب من النفخ هي ($BR=0.5, 1.0$, and 1.5). لتنبؤ عن سلوك الجريان تم استخدام الحلول العددية. أعطت الاختبارات العددية المستخدمة تنبؤ جيد لسلوك النفث البارد المحقون مع الجريان الرئيسي الحار. أن الاختبارات النظرية التي تم استخدامها في مجال الجريان وعند منطقة التداخل بين التيارين البارد والحار أظهرت وجود

نوعين من الدوامات الكبيره، زوج من الدوامات المتعاكسة و دوامات حدوة الحصان. وقد أظهرت النتائج النظرية أن هذه الدوامات تلعب دورا " رئيسيا" في التأثير على أداء التبريد. أظهرت النتائج العملية أن فعالية الغشاء تزداد بزيادة نسبة النفخ لنموذجين الاول والثاني بينما تقل للنموذج الثالث. كما أظهرت النتائج ان النموذج الاول يعطي أداء أفضل عند مقارنتهم النموذجين الآخرين عند نسب النفخ العالية.

Introduction

Turbine blades require better cooling technique to cope with the increase of the operating temperature with each new engine model. Film cooling is one of the most efficient cooling methods used to protect the gas turbine blades from the hot gases. Jet holes arrangement offers reliable technique help to improve the coolant effectiveness of the film cooling.

Film cooling primarily depends on the coolant-to-mainstream pressure ratio or can be related to the blowing ratio, temperature ratio (T_c/T_m), the film cooling hole location, configuration, and distribution on a turbine elements film cooling. In atypical gas turbine blade, the range of the blowing ratios is of about 0.5 to 2.0, while the (T_c/T_m) values vary between 0.5 and 0.85 [1].

Injecting behavior of two rows of film cooling holes with opposite lateral orientation angles have been investigated by [2] in which hole rows arrangements were one inline and three staggered. Detailed adiabatic film cooling effectiveness distributions were measured using thermochromic Liquid Crystal to investigate how well the injecting covers the film cooled surface. They found that staggered opposite lateral arrangement shows best cooling performance.

Detailed of heat transfer coefficient and film effectiveness measurements were obtained simultaneously using a single test transient IR thermography technique for a row of cylindrical film cooling hole and shaped holes by [3]. A number of anti-vortex film cooling designs that incorporate side holes. They found that the presence of anti-vortex holes mitigates the effect the anti-vortices pairs. Experimental and numerical investigations were done by [4 and 5] to measure and to predict the film cooling performance for a row of cylindrical holes. They used adiabatic film effectiveness and heat transfer coefficients were determined on a flat plate by using a single test transient thermograph technique at four blowing ratios of 0.5, 1.0, 1.5 and 2.0. Four test designs crescent and converging slot, trench and cratered hole exits, are tested. Results showed that both the crescent and slot exits reduce the jet momentum at exit and also provide significantly higher film effectiveness with some increases in heat transfer coefficients.

Numerical prediction of [6] shows that the flow field structure of injected holes present vortices such as counter pair kidney vortex and horseshoe vortex have major effects on cooling performance, in which the strength of the kidney vortex decreases and the horseshoe vortex is lifting up, leading to an improvement in the coolant performance. Therefore numerical model is suitable to design holes arrangement futures of film cooling system by introducing oriented holes row over single jet holes row.

Experimental Facilities

Low speed open duct test rig is used at the present investigation to supply uniform hot air to the test section as shown in figure 1. The settling chamber of the test rig contains a series of electrical heaters and row of screen to ensure adequate hot air of uniform temperature throughout the test rig. The hot air routed through a convergent- divergent contraction having a rectangular cross-section before flowing through the test section. In order to allow the air to reach the desired temperature, the air is initially routed out away from the test section by using a by-pass gate passage. The temperature of the air is continuously monitored at the exit of the gate and when the desired temperature is reached, the gate is gradually fully opened and the hot air is passes into a test section through a rectangular duct. The operating velocity in the test section is controlled to run from 20 to 40m/s. The test section has 50mm width and 100mm height. The bottom plate of the test section is made of (234x123) mm Plexiglas of 10mm thickness and used as the test model.

A centrifugal air blower was used to supply the coolant air to the plenum. The plenum was located below the test model. The coolant air enters a plenum then ejected through holes into the test section. The coolant air pressure is measured at the inlet of the test section. Digital thermometers were used to measure the mainstream and coolant air temperature. Pre-testing showed that all holes exists constant desired flow rate and temperature.

Two rows of staggered holes with opposite orientation angles are included in the present study. The orientation angles (γ) is defined as the hole orientation toward the cross-flow in the mainstream and the inclination angle (θ) is defined as the angle between the centerline of the hole and the surface of the test wall as shown in figure 2. Three models at different holes direction are shown in table (1). Each model consists of two rows of holes arranged in a staggered arrangement. For model 1, the inclination angle of the upstream and downstream rows are fixed at ($\theta=30^\circ$), and the orientation angle of ($\gamma=0^\circ$) and ($\gamma=180^\circ$) for the downstream and upstream row holes respectively. For model 2, the jet injected angles of upstream and downstream holes are fixed at ($\theta=30^\circ$) and ($\gamma=0^\circ$). While for model 3, the jet

injected angles of upstream and downstream holes are fixed at ($\theta=30^\circ$) and ($\gamma=180^\circ$). Each of holes (upstream and downstream row) contains eight holes. The holes diameter is 4mm, the longitudinal distance between the upstream and downstream rows (X/D) is $4D$, and the span distance between two neighboring holes (S/D) is $3D$. Data collected only for three middle holes for each row to reduce the effects of the side wall as shown in figure (3).

Surface temperature measurement

The surface temperature of test model was measured using an infrared thermographs technique. IR thermograph infrared camera type Fluke Ti32 is used at the present investigation. This camera is able to precisely record temperature variations. The IR system is greatly affected by both background temperature and local emissivity. The test surface is sprayed with mat black color to increase the emissivity like a perfect black body. The temperature measurement taken is not accurately recorded unless the IR system is calibrated.

The system was calibrated by measuring the temperature of the test surface using thermocouple type K and the reading of IR camera. The test surface is heated by mainstream hot air. The measured of temperatures obtained by both ways are recorded and stored during the heating process until achieving a steady state condition. Due to the emissivity of the test surface the temperature obtained by IR camera is differ from the temperature obtained by the thermocouple, therefore IR camera reading is adjusted until both temperatures reading are matched.

Film cooling effectiveness and heat transfer coefficient estimation

Consider the transient flow over a flat plate as shown in figure 4. In this case the test plate is initially at a uniform temperature T_i , and the convective boundary condition is suddenly applied on the plate at time $t > 0$. Now, heat assumed to be conducted only in the x-direction and perform an energy balance on the plate, therefore the one-dimensional transient conduction equation is

$$\frac{\partial^2 T}{\partial x^2} = \frac{1}{\alpha} \frac{\partial T}{\partial t} \quad (1)$$

The main approximation often applied to analyze transient conduction shown in Figure 4 is the semi-infinite approximation. The semi-infinite solid assumptions are valid for present investigation for two reasons. The test duration is small, usually less than 60 seconds. Secondly, the hot air flowing over the test surface made from Plexiglas of, low thermal

conductivity, low thermal diffusivity, and low lateral conduction. Therefore the solution of equation (1) as given by [7] is as follows:

$$\frac{T_w - T_i}{T_m - T_i} = 1 - \exp\left(\frac{h^2 \alpha t}{k^2}\right) \operatorname{erfc}\left(\frac{h\sqrt{\alpha t}}{k}\right) \quad (2)$$

Where T_w measured by using IR camera, all the other variables in the equation (2) are either known variable or measured variable except the heat transfer coefficient (h).

In film cooling case, the film should be treated as a mixture of air mainstream and the coolant air, as shown in figure 5, the mainstream temperature (T_m) in equation(2) has to be replaced by the film temperature (T_f), therefore equation (2) become as:

$$\frac{T_w - T_i}{T_f - T_i} = 1 - \exp\left(\frac{h^2 \alpha t}{k^2}\right) \operatorname{erfc}\left(\frac{h\sqrt{\alpha t}}{k}\right) \quad (3)$$

A non-dimensional temperature term is known as the film cooling effectiveness (η), and is defined as:

$$\eta = \frac{T_f - T_m}{T_c - T_m} \quad (4)$$

Equation (3) has two unknowns (h and T_f), to solve this equation, two sets of data points required to obtain the unknowns like:

$$\frac{T_{w1} - T_i}{T_f - T_i} = 1 - \exp\left(\frac{h^2 \alpha t_1}{k^2}\right) \operatorname{erfc}\left(\frac{h\sqrt{\alpha t_1}}{k}\right) \quad (5)$$

$$\frac{T_{w2} - T_i}{T_f - T_i} = 1 - \exp\left(\frac{h^2 \alpha t_2}{k^2}\right) \operatorname{erfc}\left(\frac{h\sqrt{\alpha t_2}}{k}\right) \quad (6)$$

In this case, a transient infrared thermograph technique will be used to obtain both h and η from a single test as described by [8]. Thus, two images with surface temperature distributions are captured at two different times during the transient test.

A net heat flux ratio is used to measure the combined effect of film effectiveness and heat transfer coefficient [9]:

$$\frac{q}{q_o} = \frac{h}{h_o} \left(1 - \frac{\eta}{\phi}\right) \quad (7)$$

The value for the overall cooling effectiveness (ϕ) ranges between 0.5 and 0.7. A typical value is $\phi = 0.6$ according to [10], and this is generally assumed in the present experimental analysis.

The IR images for models surface at each investigated test was captured and stored by thermal camera. These images are transferred to PC. Smart View Software program supplied with Camera can be used to limit the selected area to avoid the effect of the test section walls. The IR images converted to corresponding temperature digital values and then saved as data in Excel sheet.

MATLAB programs Software are prepared using a semi-infinite solid assumption to introduce the film cooling effectiveness and heat transfer coefficient contours. Equations, (4), (5), (6), and (7) may be solved using MATLAB Software, Smart View Software, and Excel Software. The data were collected from the selected area denoted by (A_o); this area included only six staggered jet holes as shown in Figure (3).

The measurement uncertainty was determined by using the methodology given by Ref. [11]. Error estimates for each variable are as follows: wall temperature ($\Delta T_w = \pm 2^\circ\text{C}$), initial temperature (ΔT_i) is $\pm 2^\circ\text{C}$, mainstream temperature (ΔT_m) is $\pm 0.2^\circ\text{C}$, and coolant temperature (ΔT_c) is $\pm 0.2^\circ\text{C}$. the camera frame rate is 60 Hz resulting in a time error (Δt) of $\pm 0.125 \text{ sec}$ and the test surface property (α and k) uncertainty are taken from tabulated values, as a custom, $\pm 3\%$ relative uncertainty is assumed for both variables. The resulting average uncertainty for heat transfer coefficient and film effectiveness is $\pm 8.2\%$ and $\pm 11.0\%$, respectively.

Numerical procedure

In the present study, air is taken as the working fluid and the flow characteristics are assumed to be steady flow, Newtonian fluid, incompressible fluid (Mach number=0.11), turbulent flow, three dimensional. The numerical computation area was matched to the experimental domain instead of computing only two holes with symmetry boundary conditions. FLUENT version (12.1), GAMBIT software and Auto CAD 2011 will be used to create, grid for the system geometry and then simulate the film cooling for the three geometry model and three blowing ratio. The solution of the Reynolds Averaged Navier-Stokes and energy equations is obtained by using the commercial CFD software FLUENT is applied. Fluent is based on an unstructured solver using a finite volume approach for the solution of the RANS equations. The system geometry shown in figure 6 consists of the box with dimensions (128x12x50) mm for the hot mainstream, box with dimensions (35x12x20) mm for coolant jet and the different model geometry of two rows of holes as shown in table 1. The system geometry is drawn by using (Auto CAD 2011 code). The diameter of cooling hole is 4mm. The coolant conditions were maintained the same in all cases and the mainstream flow rate was altered to change the blowing ratios. The Mainstream temperature was set at 322 K and the coolant temperature was set at 302 K. At the exit plane, pressure level was specified along with zero streamwise gradients for all other dependent variables.

The current study used the standard ($k - \varepsilon$) model for the simulating the turbulent flows in film cooling. The standard ($k - \varepsilon$) model is economical with reasonable accuracy for

a wide range of turbulent flows and it is widely used in heat transfer simulation[12]. There are some general guidelines to create a good mesh. These guidelines are shortly called rules of QRST standing for (Quality, Resolution, Smoothness, and Total cell count) [13]. The importance of quality parameter is the face alignment; it is the parameter that calculates skewness of cells. Elements with high skewness should be avoided. The way of checking whether the solution is grid independent or not is to create a grid with more cells to compare the solutions of the two models. Grid refinement tests for average static temperature on hot surface indicated that a grid size of approximately (2.5 million cell) provide sufficient accuracy and resolution to be adopted as the standard for film cooling system. The nodes near the test plate surface were adjusted so that average y^+ value was about 20 near the test plate surface which is within the range of Ref.[14]. The most significant factor to be monitored for the present model is the average static temperature on hot surface. When the average static temperature on hot surface value monitor converged it is unnecessary to go further on with the iterations and wait even if the residuals do not fall below the defined convergence criteria.

Results and Discussion

Figure 7 shows the contours of film cooling effectiveness for three models. The film cooling effectiveness increases with increasing the blowing ratios for model 1 and model 2, while for model 3 the effectiveness values decreases with increasing the blowing ratio. Near the hole exit and downstream, model 2 exhibit more uniformity of η values as the blowing ratios increased more than the other models for all blowing ratios. For model 3 the η contours exhibit high values of η at a hole downstream area at a low BR (BR=0.5) and η decreases with an increase in BR. This behavior only exists at model 3. Model 1 provides better performance when compared with other models at high blowing ratios (BR=1 and 1.5), because different jet holes arrangement gave different flow behavior. The behavior of flow in three dimensional domains is a complicated flow regime. To simplify the case and to make the flow recognizable and readable, the flow will be presented in two dimensions in a plane perpendicular and parallel to the cross flow at different plane location. When the coolant jet flow with the direction of hot mainstream ($\gamma=0^\circ$), multiple vortex structures are produce where two large vortex structures have been detected, counter rotating vortex pair (CVP), and horseshoe vortices. CVP plays an important role in the contribution of jet lifting off, this can be seen clearly in the case of low momentum jet (BR=0.5) and the case of high momentum jet (BR=1.5), in which the horseshoe vortex is strongly influenced by high jet momentum [6]. While when coolant jet flow opposite to the direction of hot mainstream ($\gamma=180^\circ$), the main

stream creates a local variation of pressure at the hole exit. The pressure of the injected air on the upstream side of the hole is elevated, thus locally reducing the jet velocity; and pushing up the hot stream depending on the blowing ratio. On the downstream side of the hole, the pressure falls and locally increases the exit velocity. As the cooled air penetrate into the hot stream, its momentum decreases up to the momentum of the main stream then bend back toward the surface causing lee vortex.

The pressure variation at the hole exit create a reverse flow where part of the cooled air exits in the direction tangent and normal to rims hole reducing the jetting effect at hole rims, which was responsible for creating kidney vortex as in the forward injection. This reverse flow creates pair of vortex similar to the kidney vortex downstream but in a plane parallel to the main stream $(CVP)_p$, this vortex is sweeping near the surface and pushing away the horseshoe vortex where moderate and wider protection area are obtained at low and high BR around the hole area. For model 1, two types of vortices are created, one $(CVP)_p$, while the second is (CVP) as shown in figure 8. For model 2 two pairs of vortices $(CVP)_p$ are appeared in a plane parallel to hot mainstream flow 1mm above the surface as shown in figure 9. In model 3 four vortices exist in the vertical plane in the hole downstream as shown in figure 10.

As a matter of fact, the enhancement of the blade surface protection is done by keeping the local heat transfer coefficient (h) as low as possible. The local heat transfer coefficients are calculated from the data of two IR images taken in successive times. Figures 11 represents the effect of blowing ratio on local heat transfer coefficients for models (1, 2 and 3), (h) increases with increasing BR models (1 and 2), while it decreases with increasing BR for model 3. At low blowing ratios ($BR=0.5$), model 3 provides high heat transfer coefficient values than models 1 and 2. As the blowing ratio increases to 1 and 1.5, model 1 gave higher heat transfer coefficient than models 2 and 3.

Figure (12a, b and c) shows (η_{sa}) variation with (X/D) for the same three models. (η_{sa}) is calculated as the average values taken from the local reading of 46 pixels in spanwise direction in twenty streamlines location downstream from the hole exist. The streamwise distance between each two successive spanwise location is (D) . Model 2 shows different behavior than that of the other models as shown in figure (12 .a, b, and c), in which (η_{sa}) decreases gradually with increase in (X/D) for all BR, while in models 1 and 3, (η_{sa}) decreases and then increases. From these figures, it can be seen that any model from these models has an advantage and disadvantage. So are can notice that model 2 gave better values of film cooling effectiveness than that of the other models near the hole exit for all BR. In the downstream

region at (BR=0.5), model 3 gave higher value of (η_{sa}) than that of the other models, but for cases (BR=1 and 1.5), model 1 gave better performance for approximately ($X/D \geq 7$).

The overall average film cooling effectiveness for the entire selected area A_o (η_{av}) was calculated from the values of local film cooling effectiveness (η) for the entire pixels values included by the area (A_o). Figure 13 shows the effect of the blowing ratio on the averaged film cooling effectiveness (η_{av}) for the same cases. This Figure shows that model (1) gave higher value of (η_{av}) than other models, especially at high blowing ratio. It appears that the averaged film cooling effectiveness increases slightly with increasing BR, in models 1 and 2, while it decreases with increasing (BR) in model 3.

The average of the local heat transfer coefficient ratios (h / h_o), in which (h and h_o) represent the heat transfer coefficient on the plate surface with and without film cooling respectively are presented in Figure 14. This figure shows that model 1 gives high (h/h_o) with respect to the other two models at high blowing ratio.

In the practical application, turbine designers are concerned with the reduction of heat load to the film protected surface. The heat load can be presented by combining film cooling effectiveness (η) and the heat transfer coefficient ratio (h/h_o), according to equation (7), therefore the ratio (q/q_o) can be calculated. (q/q_o) represent the reduction in heat flux at the tested surface with the presence of coolant air. If the values of these ratios are less than 1, then the film coolant is beneficial according to Ref. [5], while if the values are greater than 1, therefore effect of the film coolant is poor. Figure 15 represents the effect of blowing ratio on the overall heat flux ratios (q/q_o). It appears that the BR effect dominates the holes direction effects.

Conclusions

The present work has reached to the following conclusions:

Numerical prediction of the flow field structure for holes arrangement shows that the vortices (counter pair kidney vortex and horseshoe vortex) both have major effects on cooling performance.

The reverse flow from backward injection hole creates pair of vortex similar to the kidney vortex created from forward injection hole, but in a plane parallel to the main stream.

Near the exit holes area, model 2 (opposite direction rows hole) shows uniform heat protection from the hot gas streams.

For low blowing ratio, the film cooling effectiveness is constructed at the holes exit region, while at high blowing ratio, the coolant jets developed downstream give better film

cooling effectiveness. On the other hand, model 3 arrangement (staggered rows, both inclination angles in the stream line direction) show an odd behavior.

Nomenclatures

A_o selected area.

BR blowing ratio

CFD Computational Fluid Dynamic

CVPCounter rotating vortex pair

(CVP)_pCounter rotating vortex pair in parallel plan to main stream

D film hole diameter

Exp.Experimental

h heat transfer coefficient with coolant injection.

h_o heat transfer coefficient without coolant injection.

K thermal conductivity of test surface.

q heat flux with coolant injection.

q_o heat flux without coolant injection.

T time when the IR image was captured.

T_c coolant air temperature

T_f film temperature

T_i initial temperature

T_m mainstream temperature

T_w wall temperature

U_c coolant air velocity

U_m mainstream air velocity

η film effectiveness

η_{sa} spanwise average film cooling effectiveness

η_o average film cooling effectiveness

\emptyset overall cooling effectiveness

α thermal diffusivity

γ orientation angle

Θ inclination angle

References

- [1] Han, J.C. and Ekkad, S.V., “Recent Development in Turbine Blade Film Cooling”, International Journal of Rotating Machinery, Malaysia, Vol. 7, No. 1, 2001, pp. 21-40.
- [2] Ahn, J., Jung, I.S., and Lee, J.S., “Film cooling from two rows of holes with opposite behavior and adiabatic film cooling effectiveness”, International Journal of Heat and Fluid Flow, Vol. 24, 2003, pp. 91-99.
- [3] Dhungel, A., Phillips, A., Ekkad, S.V., and Heidmann, J.D., 2007, “Experimental Investigation of a Novel Anti-Vortex Film Cooling Hole Design”, ASME IGTI Turbo Expo, Montreal, Paper GT 2007-27419.
- [4] Lu, Y., Dhungel, A., Ekkad, S.V., and Bunker, R.S., 2007, “Effect of Trench Width and Depth on Film Cooling from Cylindrical Holes Embedded in Trenches”, ASME Paper GT 2007-27388.
- [5] Lu, Y., Dhungel, A., Ekkad, S.V., and Bunker, R.S., 2007, “Film Cooling Measurements for Cratered Cylindrical Inclined Holes”, ASME Paper GT 2007-27386.
- [6] Alwan, M.Sh., 2012, “Experimental and Numerical Investigation of Film Cooling Thermal Performance for Staggered Rows of Circular Jet” PhD thesis, Mechanical Engineering Department, University of Technology.
- [7] Holman, J.P. and Bhattacharyya, S., “Heat Transfer”, Ninth Edition, New Delhi, McGraw-Hill, 2008.
- [8] Ekkad, S.V., Ou, S., and Rivir, R.V., “A Transient Infrared Thermography Method for Simultaneous Film Cooling Effectiveness and Heat Transfer Coefficient Measurements from a single test”, GT 2004-54236, Proceedings of ASME Turbo Expo 2004, Vienna, Austria.
- [9] Ekkad, S.V., and Zapata, D., “Heat transfer coefficients Over a Flat Surface with Air and CO₂ Injection Through Compound Angle Holes Using a Transient Liquid Crystal Image Method”, ASME Journal of Turbomachinery Vol. 119, No. 3, 1997, pp. 580-586.
- [10] Albert, J.E., Cunha, F. and Bogard, D.G., 2004, “Adiabatic and Overall Effectiveness for a Film Cooling Blade”, ASME Paper GT2004-53998.
- [11] Kline, S.J. and McClintock, F.A., 1953, “Describing uncertainties in single sample experimental”, Mechanical Engineering, Vol. 75, pp. 3-8.
- [12] Versteeg, H.K. and Malalasekera, W., 1996, “An introduction to computational fluid dynamics the finite volume method”, Longman Group, London.

- [13] Öztürk E., 2004, “CFD analysis of heat sinks for CPU cooling with FLUENT”, MSc thesis, graduate school of natural and applied sciences, Middle East Technical University.
- [14] Jones, D.A. and Clarke, D.B., 2005, “Simulation of a wind-body junction experiment using the fluent code”, DSTD-TR-1731, Australia.

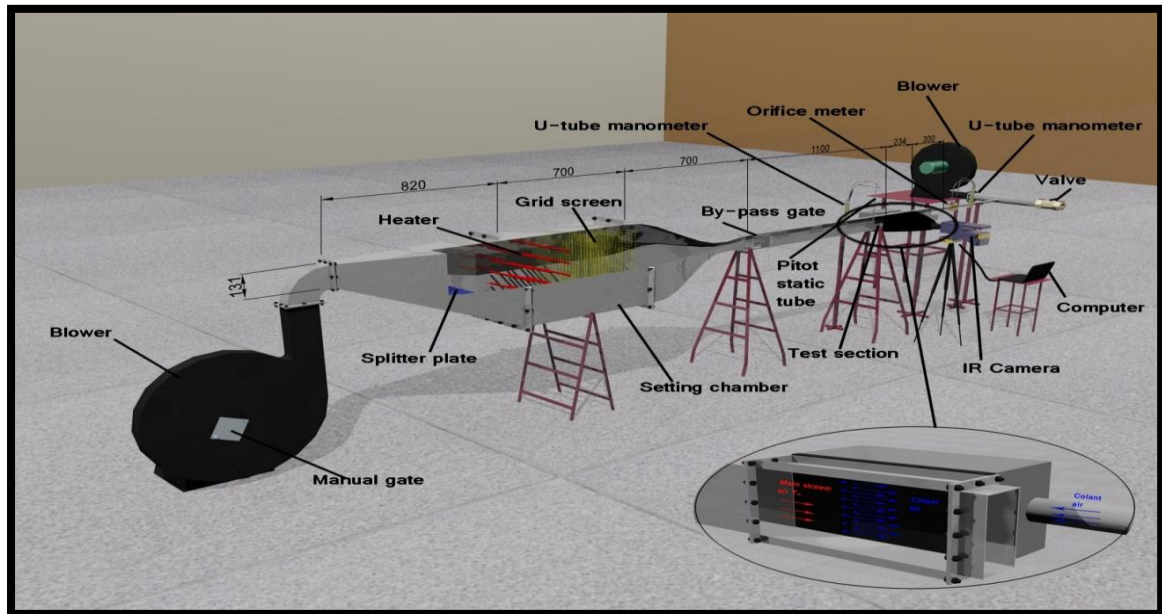


Figure 1 Schematic of the test rig

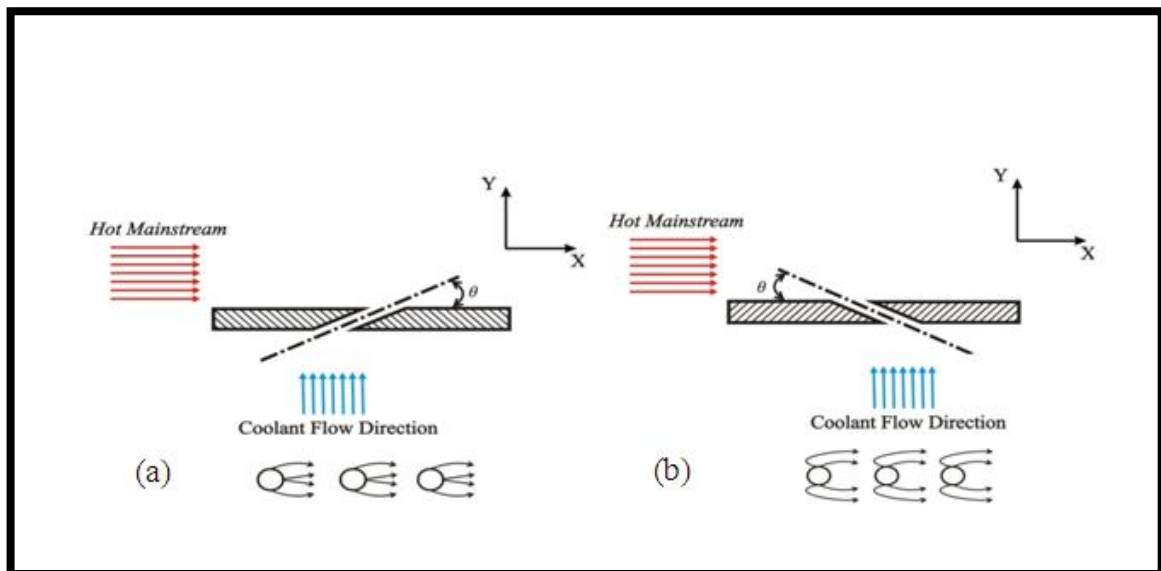
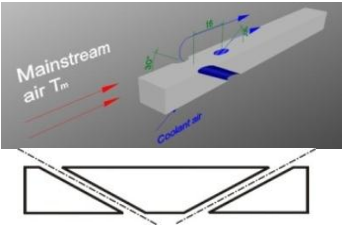
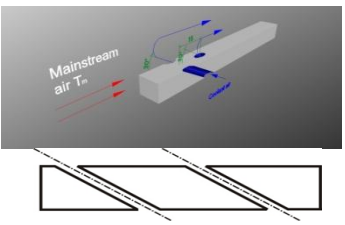
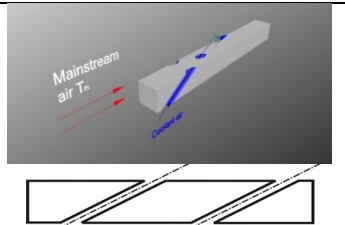
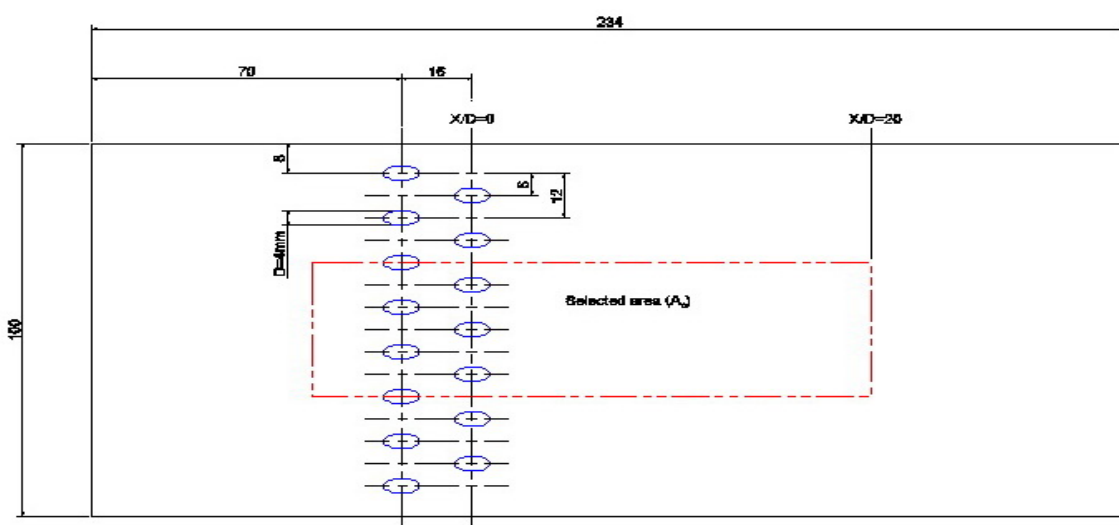


Figure (2) Illustrate diagram of the inclination and orientation angle:(a) $\theta = 30^\circ$ and $\gamma = 0^\circ$, (b) $\theta = 30^\circ$ and $\gamma = 180^\circ$

Table (1) illustrated geometry for the three models.

Model Number	Upstream Row		Downstream Row		Shape
	θ	γ	θ	γ	
Model1 Stagger	30° Acute jet angle	180°	30° Acute jet angle	0°	
Model2 Stagger	30° Acute jet angle	180°	150° Obtuse jet angle	180°	
Model3 Stagger	150° Obtuse jet angle	0°	30° Acute jet angle	0°	


Figure 3 the middle selected area of the test section (A_0)

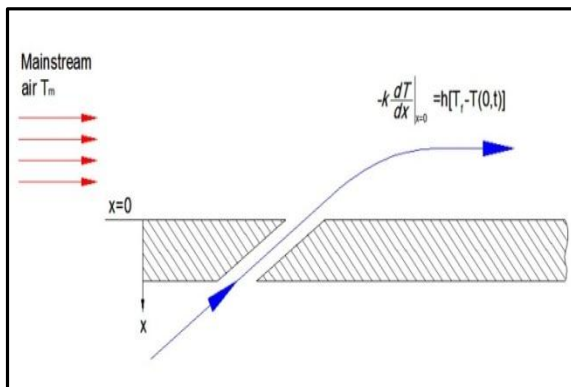


Figure 4 Flow over a flat plate

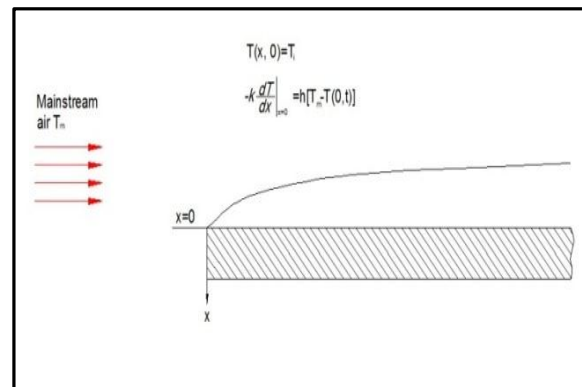


Figure 5 Film cooling over a flat plate

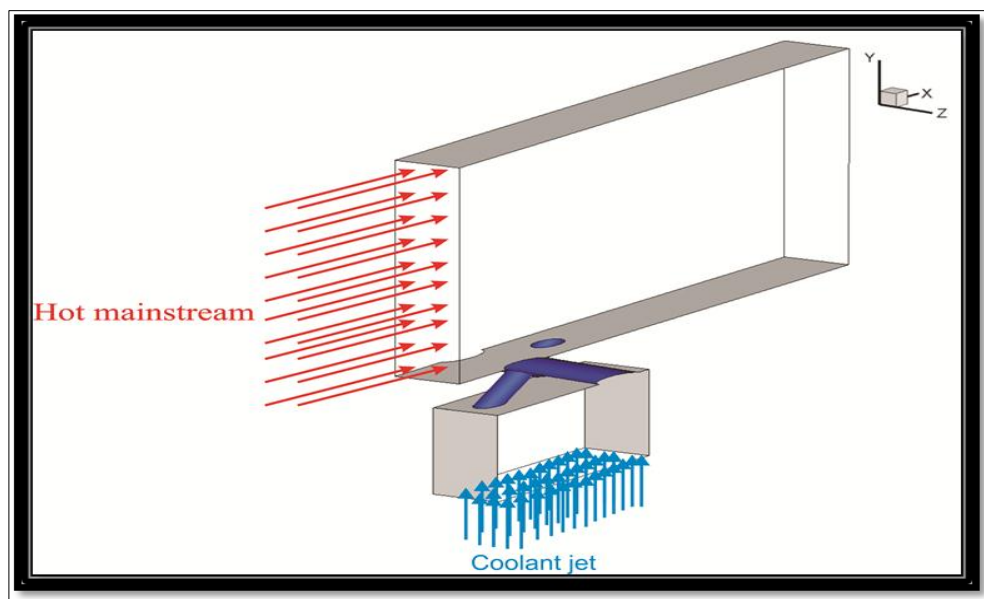


Figure 6 Schematic of geometry shape

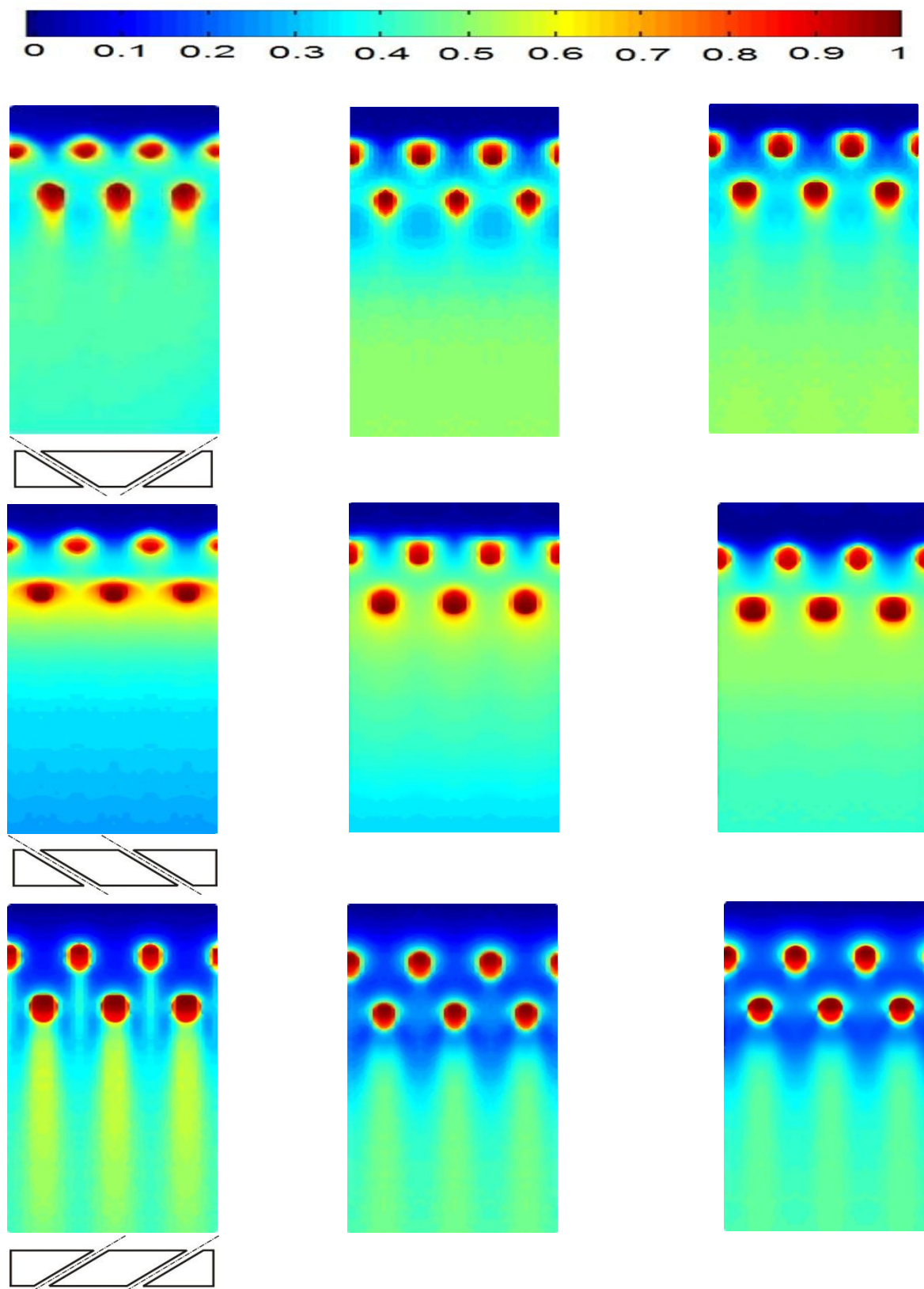


Figure 7 Contours of film cooling effectiveness for models (1, 2 and 3) at different blowing. (Exp.)

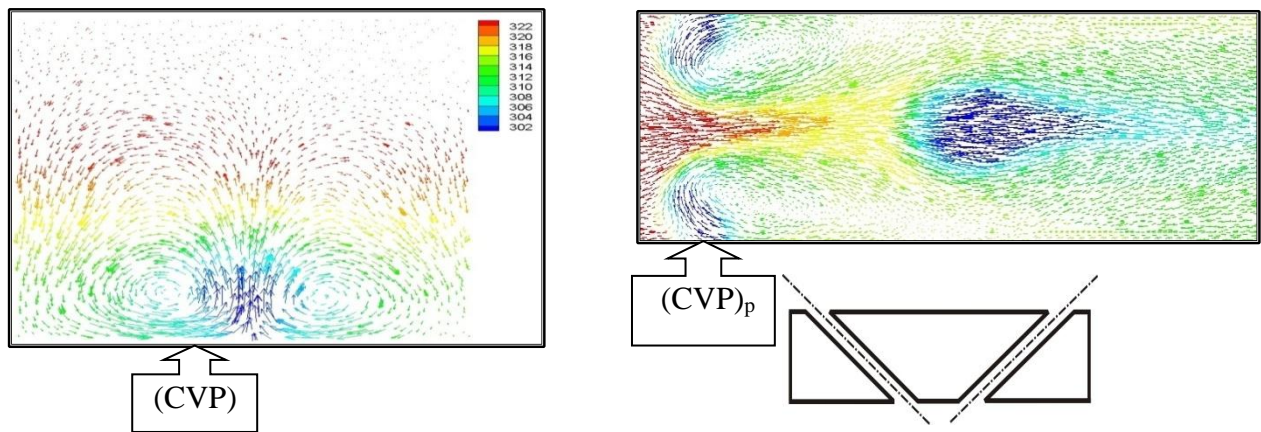
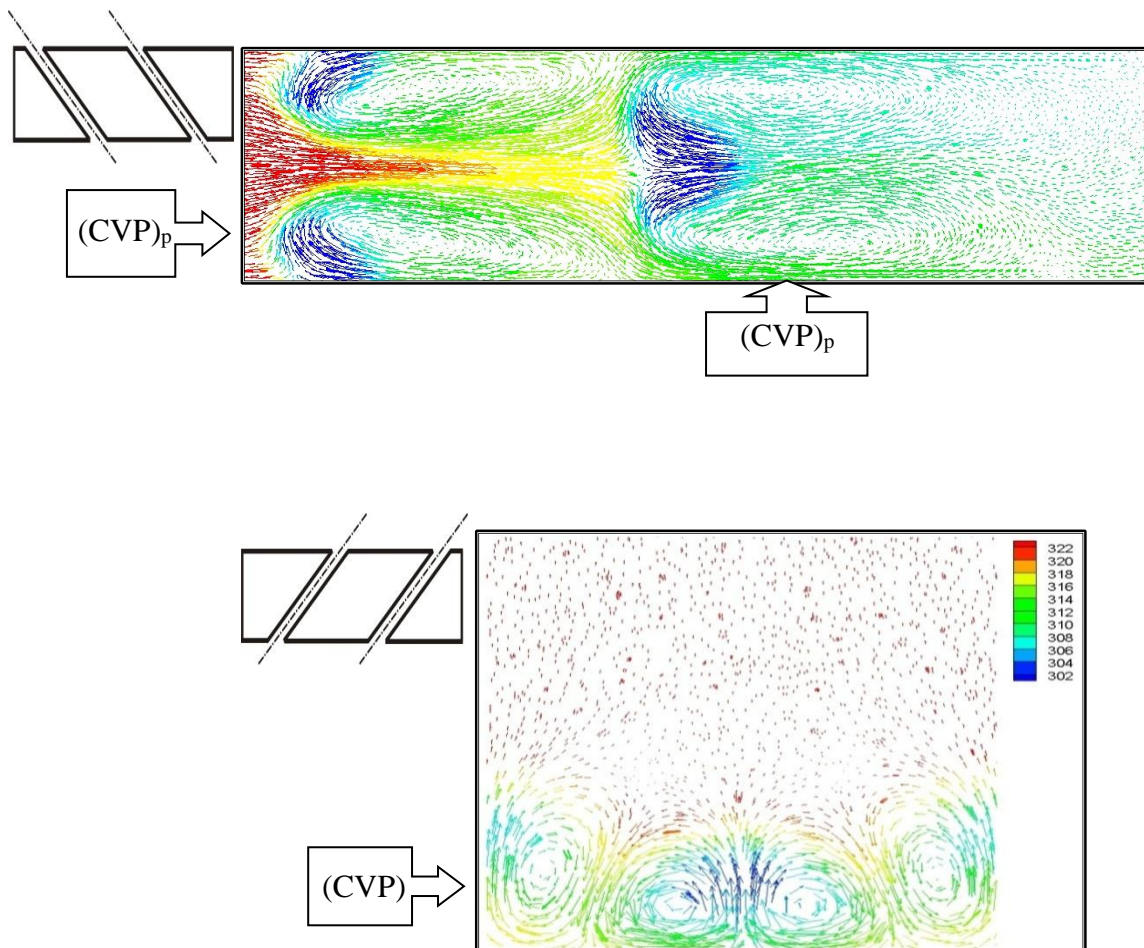


Figure 8 (a) Flow vectors colored by temperature at plane $(X/D=4)$ for model 1 at $BR=1.5$ (CFD)
 (b) Flow vectors colored by temperature at plane parallel to test surface $(Y=1mm)$ for model 1 at $BR=1.5$ (CFD)



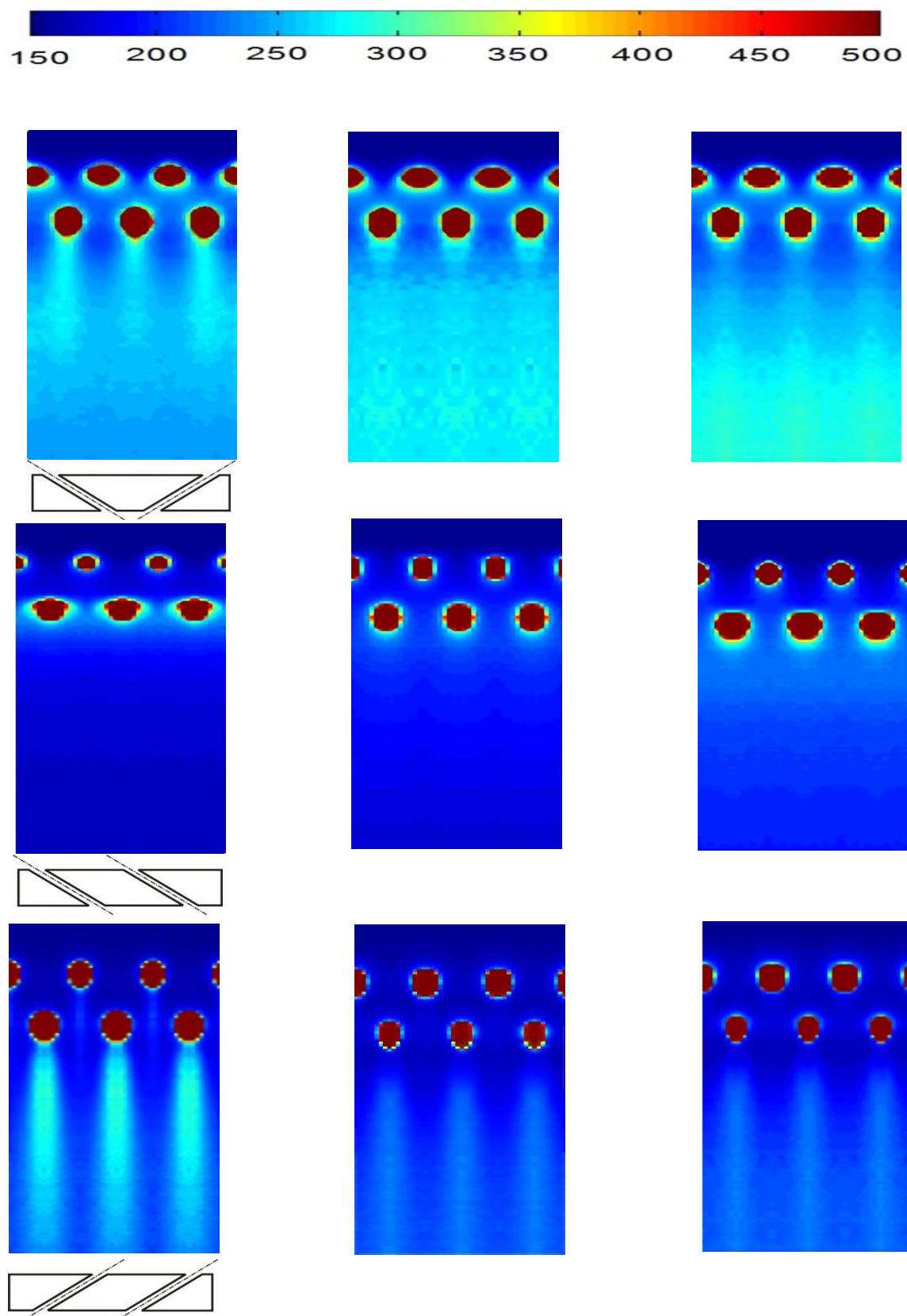


Figure 11 Contours of heat transfer coefficients ($\text{W/m}^2\cdot\text{K}$) for models (1, 2 and 3) at different blowing ratio. (Exp.)

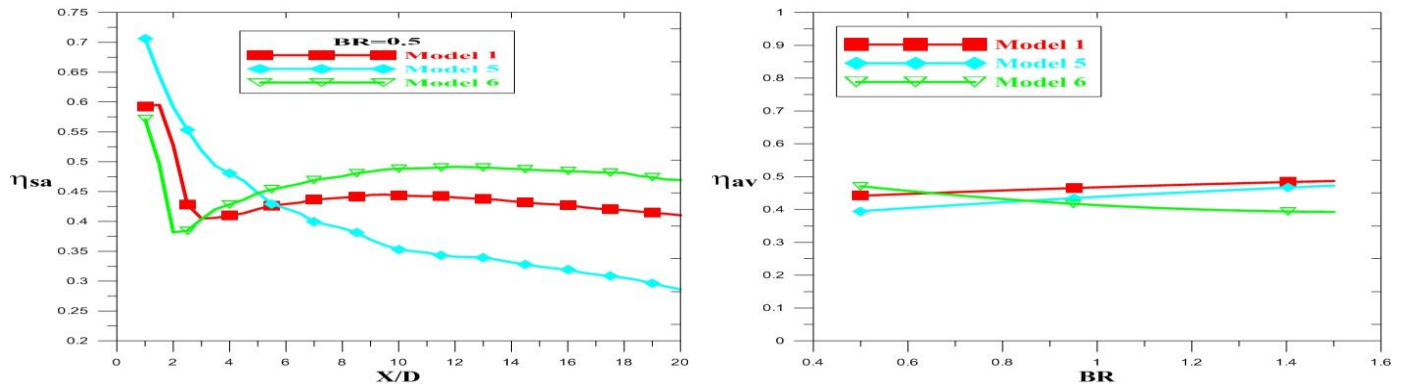


Figure 13 Effect of blowing ratios on averaged film cooling effectiveness for models (1, 2 and 3). (Exp.)

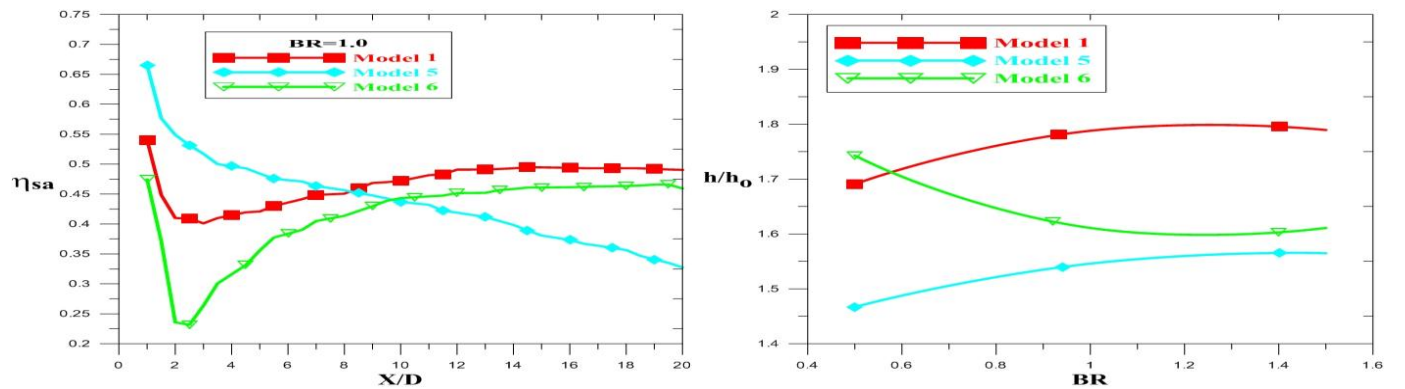


Figure 14 Effect of blowing ratios on averaged heat transfer coefficient ratios for models (1, 2 and 3). (Exp.)

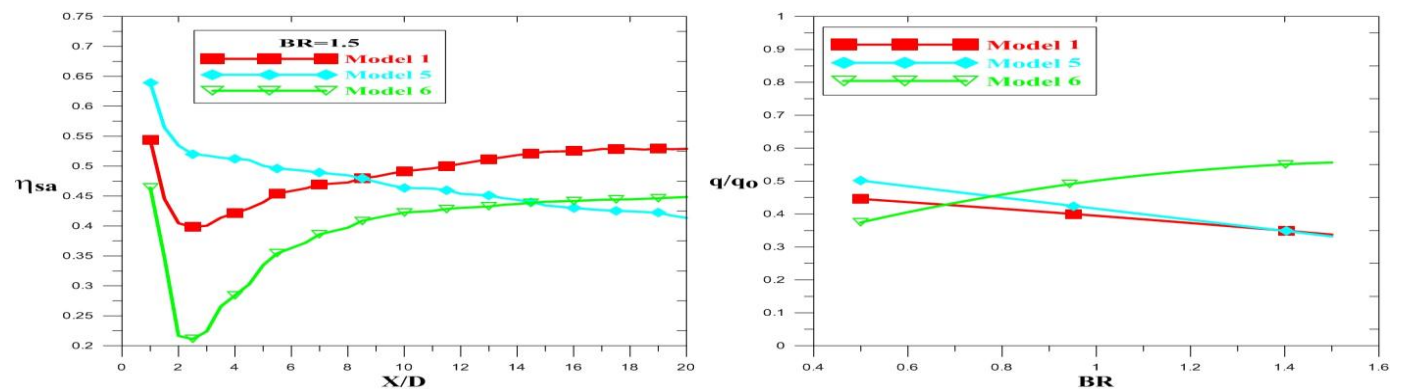


Figure 12 Effect of hole arrangement on span wise averaged film cooling effectiveness for models (1, 2 and 3) at:(a) $BR=0.5$, (b) $BR=1.0$, (c) $BR=1.5$. (Exp.)

Figure 15 Effect of blowing ratios on overall averaged heat flux ratios for models (1, 2 and 3). (Exp.)